Interactions of Cellulose Nanocrystals in Colloidal and Composite Systems

by

Cailean Q. Pritchard

Dissertation submitted to the faculty of Virginia Polytechnic Institute and State University in partial fulfillment of the requirements for the degree of

DOCTOR OF PHILOSOPHY

in

Chemical Engineering

Michael J. Bortner, Chair

William A. Ducker

Richey M. Davis

Maren Roman

September 16, 2021

Blacksburg, VA

Keywords: cellulose nanocrystal, cellulose nanofibril, nanocomposite, thermoplastic polyurethane, diffusion-softening, orientation

Interactions of Cellulose Nanocrystals in Colloidal and Composite Systems

by

Cailean Q. Pritchard

Technical Abstract

Cellulose nanomaterials (CNMs) have been widely studied for their potential as sustainable fillers in polymer nanocomposites, optical responsiveness in suspensions and thin films, and their orientation-dependent liquid crystalline behavior in suspensions. Cellulose nanocrystals (CNCs) have seen a particular prominence due to their versatility across a breadth of applications. The unique structure of CNCs, represented as nanoscale rods with a slight twist, provides for their self-assembly into liquid crystalline phases when their concentration is increased and can be used to generate iridescent materials with tunable wavelengths. Further, CNCs are often used as fillers in nanocomposites, due to their high single crystal Young's modulus, achieving vast enhancements in stiffness when incorporated above a critical concentration where a percolating network is formed. The breadth of applications for CNCs strongly depend not only on their crystalline structure, but crucially on the interactions between particles. These interactions are well-known, yet a complete understanding to enable the full exploitation of the properties attainable in CNC-based materials is lacking. The principal emphasis of this dissertation lies in further improving our comprehension of the interactions between CNCs across a variety of applications such that their full potential can be achieved. A review of the current research of CNC-based materials is provided to guide the discussion herein.

Interparticle interactions are studied in aqueous suspensions of CNCs in evaporating sessile droplets. This system provides a complex interrelationship between mass, heat, and momentum

transport which collectively provide a change in the local CNC concentration as a function of time. CNC interactions can be controlled throughout the evaporation process as a result of these local concentration variations. We implement a novel approach using time-resolved polarized light microscopy to characterize the evolution of these particle interactions via the orientation of CNCs as a function of CNC concentration and droplet volume. Ultimately, boundary interactions at the leading edge of the contact line during evaporation was found to drive a cascade of local CNC interactions resulting in alignment post-deposition. Computational analysis evaluated the influence of evaporation-induced shear flow during evaporation. Orientation was found to be independent of the bulk fluid flow, corroborating the importance of interparticle interactions on the ensuing alignment of CNCs. Characterization of an evaporating droplet of initially liquid crystalline suspension of CNCs verified the simulations which predicted that orientation was not coupled with entrainment. Finally, the multiple modes of orientation showed that local control over CNC properties can be realized through governance of the interactions between CNCs.

The interactions of CNCs in polymer nanocomposites were also studied for the development of smart materials which can adapt their properties in response to external stimuli. A well-known example of this phenomena is found when CNCs are introduced as fillers in thermoplastic polyurethanes (TPUs) above a critical concentration required to achieve percolation. The interactions between CNCs in the percolating network provide a strong enhancement to the modulus of these materials. However, these materials soften upon exposure to water following the disruption of inter-CNC hydrogen bonding by the diffusing water molecules, as prevailing theories suggest. CNCs simultaneously enhance water transport into hydrophobic matrices. Thus, a complete understanding of the interrelationship between the mass transport and mechanical performance can facilitate the development of humidity sensing or

shape memory materials which operate as a result of the interactions between CNCs inside of a polymer matrix. Despite an increase in the equilibrium water uptake with increasing CNC concentration, a decrease in the apparent diffusivity of water within the nanocomposites was observed as a result of swelling of the bulk polymer. Additionally, we developed a modification to the commonly used percolation model to predict the time-dependent evolution of storage modulus during water-induced softening. We found that the solvent mass transport can be directly coupled to the mechanical integrity of the percolating network of CNCs by evaluating the hydrogen bonding state of the network as a function of time.

Finally, a novel nanocomposite filler comprised of CNCs and 2,2,6,6-tetramethylpiperidine 1-oxyl (TEMPO) oxidized cellulose nanofibrils (TOCNFs) was prepared through solution casting to improve the mechanical performance of the individual reinforcements alone. The physical interaction length is increased by incorporating CNMs of different length scales resulting in increased tensile strength and elongation. Further, the morphology, evaluated with polarized light microscopy, atomic force microscopy, and simulated with dissipative particle dynamics, revealed the combined fillers exhibit a cooperative enhancement between CNMs. Characterization of the crystallinity through x-ray diffraction confirmed the interactions occur primarily between the crystalline domains of each material. Accordingly, the combination of CNMs resulted in nanocomposite fillers which can be implemented such that the weak interfaces with polymer matrices can be bridged with fillers providing reinforcement over a broader length scale.

Interactions of Cellulose Nanocrystals in Colloidal and Composite Systems

by

Cailean Q. Pritchard

General Audience Abstract

Cellulose nanocrystals (CNCs) are sustainable and biorenewable nanoparticles derived from cellulose. These materials have been widely studied and are commonly used among a plethora of applications such as in reinforcing fillers in polymer nanocomposites, optically responsive materials that can be used in packaging or anti-counterfeiting technologies, as well as in suspension modifiers for skin care products. These techniques tune the interactions between individual CNCs to modify the behavior of the bulk material. The specific interactions are well-known, yet a complete understanding of the influence of these interactions resulting in the utility of CNC-based materials in various applications is lacking. The principal emphasis of this dissertation lies in further improving our comprehension of the interactions between CNCs across a variety of applications such that their full potential can be achieved.

Interactions between CNCs were investigated in three systems comprising of a range of typical use cases for CNC-based materials. The behavior of CNCs was examined in evaporating droplets of aqueous suspensions. These materials exhibited a change in orientation in the final deposit which is dependent on variations in local CNC concentration during drying. These concentration changes describe the relative strength of interactions between CNCs which ultimately influences the final alignment of these materials. Further, these interactions provide a pathway to deposit a controlled orientation of CNCs on a substrate which can be utilized for optically responsive materials or serve as templates for other orientation-dependent materials.

CNCs were also incorporated into a thermoplastic polyurethane (TPU) matrix to provide increased stiffness. In these composites, water preferentially interacts with CNCs preventing the nanoparticles from interacting with one another. As water is absorbed, these materials soften as a result of the reduced interactions between CNCs. We investigated the influence of dynamically changing CNC interactions on the mechanical performance of these materials during water absorption and developed an analytical model to describe the observed softening behavior.

Finally, CNCs were combined with 2,2,6,6- tetramethylpiperidine 1-oxyl oxidized cellulose nanofibers (TOCNFs) and cast into thin films. The mechanical properties of these differently sized, yet chemically similar, nanoparticles were compared as a function of CNC composition. A cooperative enhancement of the ultimate tensile strength and elongation was observed at low CNC loadings where CNCs and TOCNFs were found to self-organize during casting in a mutually beneficial manner.

Acknowledgements

I would like to thank my research advisor, Dr. Michael Bortner, for his guidance throughout my PhD. In particular, his mentorship in scientific communication has been invaluable and will follow me throughout my career. Further, he supported my growth as a student, a researcher, and a leader which will allow me to excel in my future endeavors.

I would also like to thank my research committee, Dr. Maren Roman, Dr. William Ducker, and Dr. Richey Davis for their continued advice and counsel while investigating my research projects. Their diversity in research experience brought an enlightened perspective to our discussions which has broadened my research focus and provided alternative solutions to many complex phenomena.

I would also like to extend a heartfelt thank you to my fiancée, Christina Chuong, for her continued and everlasting support and love through the challenges I have endured during my PhD. Christina, your unconditional support has inspired me to continue my pursuit of excellence and knowledge. No level of acknowledgement can truly describe your commitment, your care, and I cannot imagine where I would be today without you.

I cannot conclude without thanking my wonderful family for their enduring encouragement and support. My parents, Kathryn and Craig Pritchard, and my brothers, Iain, Graham, Neil, and Stewart Pritchard, have always been there for me in difficult situations. I have found solace in their positivity and altruism. Their intellectual diversity led to many productive and scientific discussions, with all of my family, that guided me through my degree.

Additionally, I would like to thank all of my coworkers in the Bortner group for their friendship, guidance, and support in my research. I would specifically like to thank Jake Fallon,

Eric Gilmer, Kathleen Chan, and Arit Das for fostering my research and personal development, providing attentive listening, being with me throughout my PhD, and offering their advice.

Finally, the happiness, eagerness, playfulness of Hiro and Fenny have brightened my life and I thank them for their unconditional love.

Format of Dissertation

Chapter 3 of this dissertation is presented in the format of a peer-reviewed publication and is copied with permission of the Journal of Colloid and Interface Science. Chapters 4 and 5 are presented as publications in preparation for submission. Each of these chapters contain their own respective introductions, experimental methods, results, discussion, and conclusions.

Table of Contents

List of Figures

List of Tables

Chapter 1 - Introduction

1.1 Background and Motivation

Cellulose nanocrystals (CNCs) offer unique optical, mechanical, and rheological properties which can be utilized for a wide variety of applications. Due to their anisotropic properties, such as birefringence, and their tendency to self-organize in suspension, these nanoscale rod-shaped particles have seen use in a variety of optical[1-4] and electronic[5, 6] systems as well as polymer composites.[7-9] While considerable research has been conducted on nanocellulosics, additional characterization of their complex self-interactions, their interactions with similar materials, and their interactions with dissimilar materials would greatly benefit the field in continuing to develop novel materials with unique properties.

CNC suspensions are well known for their liquid crystalline (LC) phase transition between isotropic and chiral nematic phases above a critical concentration.[10] This phase transition yields a characteristic fingerprint texture when illuminated under crossed-polarized light and gives rise to tunable iridescence. To fully elucidate the optical capability of CNC films, further control of the LC structure outside of its preferred cholesteric phase is required. This has been achieved through magnetic[11-13] and shear[1, 14, 15] forces to generate uniaxial particle alignment. While these technologies offer tunable orientation in nanocellulosics, they require large energy investments, such as an 8 T magnetic field,[11] to induce and maintain orientation. A low energy alternative method for imparting controlled orientation of CNCs would aid the development of novel low cost nanocellulosics devices. We propose evaporation induced self-assembly (EISA) of CNC suspensions as an energy efficient method to meet this demand while providing a route to additional outcomes such as energy efficient patterning and templating of oriented structures.

Exploring this opportunity will require investigation of the interparticle interactions acting in CNC suspensions and their impact on rheological functions.

Another promising avenue for nanocellulosics is in their utility for composite materials. In this domain, intermolecular forces between CNC particles as well as between CNCs and polymer matrices are critical to the performance of the material as a whole. Several studies have demonstrated decreases in the moduli of CNC composites when CNC interactions are disrupted, commonly by the introduction of a solvent such as water.[16-22] These composites mechanically adapt to environmental stimuli and thus can be implemented in the design of mechanical actuators and sensors. Thus, we propose an exploration of these interactions by studying the diffusive transport mechanism of solvent in to a CNC composite. Crucially, the interactions between the solvent and CNCs as well as between the solvent and polymer matrix need to be explored to fully take advantage of this behavior and provide tunable functionality.

Finally, the nature of CNCs to interact with similar materials such as cellulose nanofibrils that are oxidized in part with 2,2,6,6- tetramethylpiperidine 1-oxyl (TEMPO) radical (TOCNFs) posits additional avenues for the design of novel composite materials. Together, these materials resemble the natural structure of wood, whereby several morphological features of increasing complexity can be observed at increasing length scales.[23] We explored the combination of CNCs and TOCNFs to develop strong lightweight composite materials. In doing so, revealing the structure-property relationships between CNCs and TOCNFs will be critical to understanding the ultimate behavior of these composite systems in practical applications. Thus, we propose the analysis of morphology and structure-property relationships between CNCs and TOCNFs to develop materials which can transfer stresses between morphological features of varying length scales.

1.2 Research Hypothesis and Objectives

The research objectives set forth in this dissertation seek to discover the relationship between interactions of CNCs and macroscopic properties. These research goals will advance the knowledge base by providing insight into the complex and difficult to characterize behavior of CNCs for utilization in a variety of systems. Further, it would be possible to extend this work to the characterization and evaluation of other strongly interacting rod-shaped nanomaterials.

1.2.1 Hypotheses

1. Evaporating sessile droplets of CNC suspensions develop particle orientation during drying as a result of the dynamic changes in local particle concentration which governs the relative influence of the interactions between these rod-shaped particles.
2. The mechanical softening exhibited in CNC-TPU nanocomposites is driven by the diffusion of water into the matrix which disrupts inter CNC hydrogen bonding, thus mechanical performance of these materials can be described as a function of water diffusion and transient hydrogen bonding state.
3. The interactions between cellulose nanocrystals and TEMPO oxidized cellulose nanofibrils can be tailored to provide cooperative enhancements to the mechanical performance of these materials.

1.2.2 Research Objectives

1. Analyze the influence of interactions between rod-shaped particles, such as CNCs, on the dynamic particle orientation developed during evaporation induced self-assembly within drying sessile droplets.
2. Evaluate the fundamental diffusive transport mechanism driving transport of water in cellulose nanocrystal-thermoplastic polyurethane nanocomposites, focusing on the local

transport at CNC and TPU interfaces to better explain the relationship between water diffusion and mechanical softening.

3. Evaluate the structure-property relationships in cellulose nanocrystal-TEMPO oxidized cellulose nanofibril composites to understand how these multiscale materials and their interactions impact morphological, structural behavior, and mechanical properties such as modulus, strength, and toughness.

References

1. Cranston, E. D.; Gray, D. G., Birefringence in spin-coated films containing cellulose nanocrystals. *Colloids and Surfaces A: Physicochemical and Engineering Aspects* **2008,** *325* (1-2), 44-51.
2. Dumanli, A. G.; van der Kooij, H. M.; Kamita, G.; Reisner, E.; Baumberg, J. J.; Steiner, U.; Vignolini, S., Digital color in cellulose nanocrystal films. *ACS Appl Mater Interfaces* **2014,** *6* (15), 12302-6.
3. Tardy, B. L.; Ago, M.; Guo, J.; Borghei, M.; Kamarainen, T.; Rojas, O. J., Optical Properties of Self-Assembled Cellulose Nanocrystals Films Suspended at Planar-Symmetrical Interfaces. *Small* **2017,** *13* (47).
4. He, Y. D.; Zhang, Z. L.; Xue, J.; Wang, X. H.; Song, F.; Wang, X. L.; Zhu, L. L.; Wang, Y. Z., Biomimetic Optical Cellulose Nanocrystal Films with Controllable Iridescent Color and Environmental Stimuli-Responsive Chromism. *ACS Appl Mater Interfaces* **2018,** *10* (6), 5805-5811.
5. Najafabadi, E.; Zhou, Y. H.; Knauer, K. A.; Fuentes-Hernandez, C.; Kippelen, B., Efficient organic light-emitting diodes fabricated on cellulose nanocrystal substrates. *Applied Physics Letters* **2014,** *105* (6).
6. Hoeng, F.; Denneulin, A.; Bras, J., Use of nanocellulose in printed electronics: a review. *Nanoscale* **2016,** *8* (27), 13131-13154.
7. Favier, V.; Chanzy, H.; Cavaille, J. Y., Polymer Nanocomposites Reinforced by Cellulose Whiskers. *Macromolecules* **1995,** *28* (18), 6365-6367.
8. Mounika, M.; Ravindra, K., Characterization of Nanocomposites Reinforced with Cellulose Whiskers: A Review. *Materials Today: Proceedings* **2015,** *2* (4-5), 3610-3618.
9. Meesorn, W.; Shirole, A.; Vanhecke, D.; de Espinosa, L. M.; Weder, C., A Simple and Versatile Strategy To Improve the Mechanical Properties of Polymer Nanocomposites with Cellulose Nanocrystals. *Macromolecules* **2017,** *50* (6), 2364-2374.
10. Revol, J. F.; Bradford, H.; Giasson, J.; Marchessault, R. H.; Gray, D. G., Helicoidal self-ordering of cellulose microfibrils in aqueous suspension. *International Journal of Biological Macromolecules* **1992,** *14* (3), 170-172.
11. Tatsumi, M.; Kimura, F.; Kimura, T.; Teramoto, Y.; Nishio, Y., Anisotropic polymer composites synthesized by immobilizing cellulose nanocrystal suspensions specifically oriented under magnetic fields. *Biomacromolecules* **2014,** *15* (12), 4579-4589.
12. De France, K. J.; Yager, K. G.; Hoare, T.; Cranston, E. D., Cooperative Ordering and Kinetics of Cellulose Nanocrystal Alignment in a Magnetic Field. *Langmuir* **2016,** *32* (30), 7564-7571.
13. Dhar, P.; Kumar, A.; Katiyar, V., Magnetic Cellulose Nanocrystal Based Anisotropic Polylactic Acid Nanocomposite Films: Influence on Electrical, Magnetic, Thermal, and Mechanical Properties. *ACS Appl Mater Interfaces* **2016,** *8* (28), 18393-18409.
14. Tatsumi, M.; Teramoto, Y.; Nishio, Y., Different orientation patterns of cellulose nanocrystal films prepared from aqueous suspensions by shearing under evaporation. *Cellulose* **2015,** *22* (5), 2983-2992.
15. Chen, S.; Schueneman, G.; Pipes, R. B.; Youngblood, J.; Moon, R. J., Effects of crystal orientation on cellulose nanocrystals-cellulose acetate nanocomposite fibers prepared by dry spinning. *Biomacromolecules* **2014,** *15* (10), 3827-3835.

16. Auad, M. L.; Contos, V. S.; Nutt, S.; Aranguren, M. I.; Marcovich, N. E., Characterization of nanocellulose- reinforced shape memory polyurethanes. *Polymer International* **2008,** *57* (4), 651-659.
17. Capadona, J. R.; Shanmuganathan, K.; Tyler, D. J.; Rowan, S. J.; Weder, C., Stimuli-responsive polymer nanocomposites inspired by the sea cucumber dermis. *Science* **2008,** *319* (5868), 1370-4.
18. Shanmuganathan, K.; Capadona, J. R.; Rowan, S. J.; Weder, C., Stimuli-responsive mechanically adaptive polymer nanocomposites. *ACS Appl Mater Interfaces* **2010,** *2* (1), 165-74.
19. Rusli, R.; Shanmuganathan, K.; Rowan, S. J.; Weder, C.; Eichhorn, S. J., Stress-transfer in anisotropic and environmentally adaptive cellulose whisker nanocomposites. *Biomacromolecules* **2010,** *11* (3), 762-8.
20. Dagnon, K. L.; Shanmuganathan, K.; Weder, C.; Rowan, S. J., Water-Triggered Modulus Changes of Cellulose Nanofiber Nanocomposites with Hydrophobic Polymer Matrices. *Macromolecules* **2012,** *45* (11), 4707-4715.
21. Dagnon, K. L.; Way, A. E.; Carson, S. O.; Silva, J.; Maia, J.; Rowan, S. J., Controlling the Rate of Water-Induced Switching in Mechanically Dynamic Cellulose Nanocrystal Composites. *Macromolecules* **2013,** *46* (20), 8203-8212.
22. Annamalai, P. K.; Dagnon, K. L.; Monemian, S.; Foster, E. J.; Rowan, S. J.; Weder, C., Water-responsive mechanically adaptive nanocomposites based on styrene-butadiene rubber and cellulose nanocrystals--processing matters. *ACS Appl Mater Interfaces* **2014,** *6* (2), 967-76.
23. Moon, R. J.; Martini, A.; Nairn, J.; Simonsen, J.; Youngblood, J., Cellulose nanomaterials review: structure, properties and nanocomposites. *Chem Soc Rev* **2011,** *40* (7), 3941-94.

Chapter 2 - Literature Review

2.1 Nanocellulose Types and Properties

Nanocellulose is frequently used in one of two forms each providing unique properties and characteristics: cellulose nanocrystals (CNC) and cellulose nanofibrils (CNF).

2.1.1 Cellulose Nanocrystals

CNCs are derived from a strong acid hydrolysis of cellulose, commonly sulfuric acid. Such hydrolysis removes the amorphous components of cellulose leaving crystalline domains on the order of 5-20 nm in width and 100-2000 nm in length and is highly dependent on the cellulose source. Hydrolysis is typically followed by dialysis and filtration to further purify the product. Additionally, further reactions such as 2,2,6,6- tetramethylpiperidine 1-oxyl (TEMPO) radical-mediated oxidation can alter the surface functionality of the CNCs from sulfate half ester groups to carboxylic acid surface functional groups, Figure 2-1**Error! Reference source not found.**.[1]

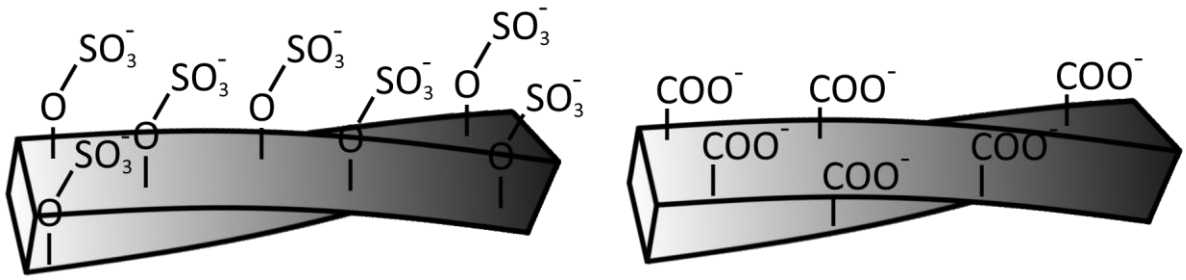

Figure 2-1 CNC surface functional groups after sulfuric acid hydrolysis (left) and post treatment with TEMPO mediated oxidation (right).

The size and aspect ratio is highly dependent on the cellulose source as soft and hardwoods yield shorter CNCs with smaller aspect ratios and CNCs derived from bacteria or tunicates yields long CNCs with high aspect ratios.

2.1.1.1 Morphology and Crystal Structure

CNCs are isolated crystalline domains from cellulose, Figure 2-2, which develops 3 primary crystallographic structures.

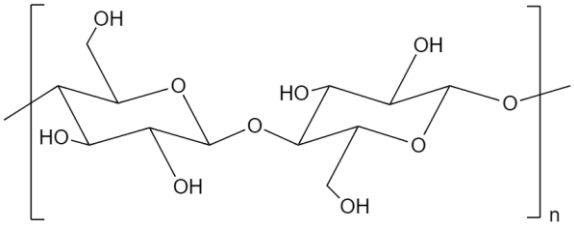

Figure 2-2. Chemical structure of cellulose

Cellulose I is divided in to two structures which maintain parallel chain conformations, monoclinic cellulose Iα and triclinic cellulose Iβ whereas Cellulose II is more thermodynamically stable and is characterized by its antiparallel chain conformation.[2] The most common polymorph of plant-based cellulose is cellulose Iβ and is found in CNCs derived from both soft and hardwoods.[2]

In suspension, CNCs develop liquid crystalline (LC) phases with orientational order when particles closely interact with one another. Above a critical concentration of 4.5 wt %, CNCs begin to separate into isotropic and chiral nematic phases.[3] These LC phases can be readily characterized via polarized light microscopy where the chiral nematic phase is identified by the pitch of its characteristic fingerprint structure.[4]

2.1.1.2 Mechanical Properties

The mechanical performance of CNCs have been evaluated with several techniques including those which characterize the mechanical properties of individual crystals and those which evaluate the behavior of CNC films typically generated from solution casting. There is great

interest in characterizing the behavior of these materials in cast CNC films as well as in composites to take advantage of their strong mechanical performance and reinforcement properties.

Atomic force microscopy (AFM) is a powerful tool which utilizes an ultrafine needle tip on the end of a cantilever coupled with a laser to measure the probes' deflection. This technique is capable of mapping the height profile of a given surface with nanometer precision as well as characterizing the stiffness of materials through a process similar to nanoindentation. AFM of isolated CNCs determined a single crystal CNC modulus of 130-200 GPa.[5, 6]

In addition to AFM, surface polarized Raman spectroscopy is another common tool used to characterize the material properties of an individual CNC. The process examines the absorption of infrared light in the sample in the Raman vibrational spectrum to characterize functional groups the modulus of a molecular structure. In such cases the modulus of individual CNCs determined by this method has been found to be comparable to reported moduli from AFM.[7, 8]

Bulk characterization of CNC mechanical properties is primarily characterized through tensile testing or dynamic mechanical analysis (DMA).[9] Tensile testing elucidates the ultimate properties of the materials, whereas, DMA is capable of revealing linear viscoelastic behavior which is frequency dependent. Tensile testing of CNC films has revealed ultimate tensile strengths on the order of 1.7 GPa[10, 11] and moduli in the range of 7-30 GPa.[12] A large discrepancy exists between the moduli reported in the bulk materials as compared to the individual crystals thus it is important to report the experimental testing procedure along with moduli. The reduced modulus in the bulk is due to probing different characteristic dimensions. Individual crystal techniques probe the strength at molecular length scales whereas bulk techniques probe the strength of interparticle interactions which are considerably weaker.

2.1.1.3 Particle Orientation

Orientation of CNCs directly relates to their performance as birefringent materials for optical applications or for mechanical reinforcement. Considerable efforts have investigated the tendency of CNCs to self-assemble into chiral nematic phases at high concentration.[4, 13, 14] Investigators seeking to impart designated orientations in CNC containing materials have implemented applied shear[15-17] and magnetic alignment.[18-20]

2.1.2 Cellulose Nanofibrils

CNFs are comprised of semicrystalline cellulose, Figure 2-3, that has been mechanical fibrillated to fibers of nanoscale diameter through high shear processes and typically range from 1-1000 μm in length depending on the degree of polymerization resulting from fibrillation.[21]

Figure 2-3. CNF cartoon depicting crystalline cellulose domains connected with amorphous tie-chains.

In contrast to CNCs, CNFs maintain an amorphous component connecting crystalline domains which results in different properties and uses. Typically CNFs appear as long fibrous structures on AFM and SEM and can form entangled networks.[21, 22] The capability to form entangled networks leads to drastic changes in the suspension rheology of CNFs compared to CNCs. In particular, CNFs exhibit shear thickening as a result of fiber entanglements at certain shear rates, however, at higher rates, such shear-induced structures are dismantled leading to shear thinning.[22] Further, the gelation concentration of CNFs, 1-2 wt % is drastically lowered, compared to CNCs, 10-14 wt %, as a direct result of the entanglements and interactions between CNFs that readily form a network structures.[23] Additionally, entanglements facilitate CNF incorporation in

polymer matrices leading to improved filler-matrix interactions enhanced mechanical properties in composite materials.[24]

2.1.2.1 TEMPO radical-mediated Oxidation

CNFs are often modified to enhance their suspension stability and improve their compatibility in various matrices. Commonly, TEMPO radical-mediated oxidation, Figure 2-4, is performed to convert hydroxyl groups to carboxylic acid functional groups.[25]

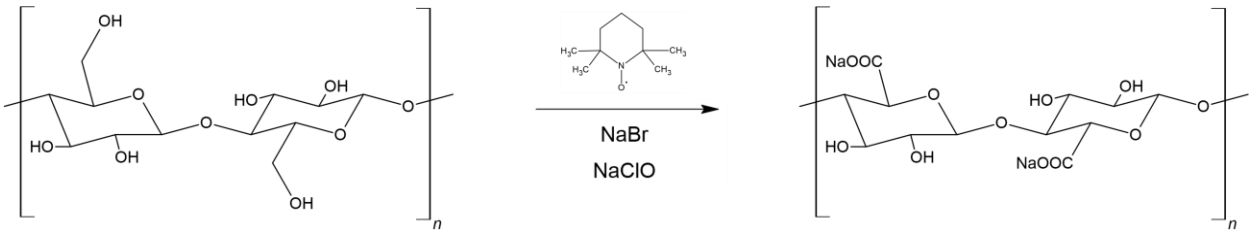

Figure 2-4. Carboxylation of cellulose by TEMPO radical-mediated oxidation.

This change in functionality increases the surface charge of these materials resulting in improved suspension stability and dispersion.[26] Additionally, the dimensions of nanofibrils are controlled during this treatment leading to smaller widths of approximately 4 nm.[27]

2.1.2.2 Mechanical Properties

Tensile testing of cast CNF films is a common technique for evaluating the mechanical performance of CNFs. As these materials contain both amorphous and crystalline cellulose, they tend to generate strong cohesive films which are flexible and optically transparent. Neat CNF films have a greater modulus than comparable CNC films, 6-7 GPa due to their improved capability to transfer stress through the entangled network.[24, 25, 28, 29] It has also been reported that TEMPO radical mediated oxidation of CNFs results in enhanced modulus, 11-12 GPa, compared to

unmodified CNFs.[28] Further, these materials tend to be more resilient than neat CNC films and can withstand more substantial strains before breaking.[29]

2.2 Evaporation

2.2.1 Evaporation of Pure Liquids

Pure liquids evaporate due to a concentration gradient between the liquid phase and the encapsulating vapor phase. Fick's second law describes this behavior well for most pure liquids, where the rate of diffusion is proportional to the Laplacian of the concentration field and the diffusivity. When the diffusivity is constant with respect to spatial coordinates, Fick's law is given by Equation (1).

$$\frac{\partial c}{\partial t} = D\nabla^2 c \tag{1}$$

Where c is the concentration of the species of interest and D is the diffusivity of the evaporating species in the vapor phase medium.

In droplet form, evaporating pure liquids have additional interactions, such as capillary flows and surface tension effects, governing the evaporation mechanism. Droplets may evaporate

in one of three primary mechanisms, illustrated in Figure 2-5: constant contact area, constant contact angle, and stick-slip which is a combination of the two prior mechanisms.[30]

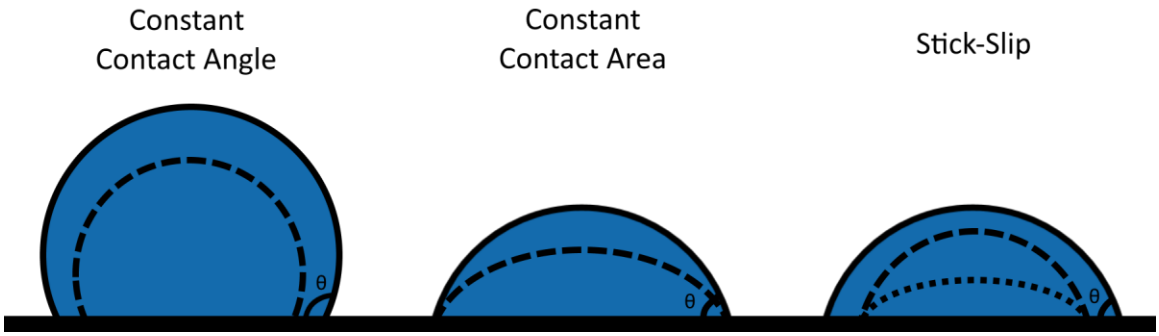

Figure 2-5. Evaporation modes of a sessile droplet. Solid lines represent the initial droplet configuration and dashed lines represent droplet geometry after a given time.

Droplets undergoing constant contact angle evaporation, often have initial contact angles greater than 90°.[31] Thus surfaces with high surface energy, having repelling interactions with the liquid phase, result in this behavior. Constant contact area evaporation follows droplets with initial contact angles less than 90°, on low surface energy surfaces.[32] The stick-slip mechanism is a mixture of constant contact angle followed by constant contact area evaporation where the droplets contact line is periodically fixed as evaporation progresses. The surface tension forces are in competition with the liquid adhesion to the substrate. As surface tension dominates over adhesive interactions a slip occurs at the contact line after which the forces equilibrate and the contact line sticks. This process can repeat several times until the evaporation completes and it can be a result of surfaces with non-uniform roughness.

2.2.2 Evaporation of Particle Suspensions

Sessile droplet evaporation with pinned contact lines and containing suspended particles lead to coffee-ring formation. Coffee rings form in a wide range of applications from inkjet

printing, self-assembly, templating, and fabrication of functional nanomaterials, but it is often an undesirable phenomenon that needs to be controlled to meet fabrication outcomes. In some cases, coffee rings have been exploited for industrial applications through controlled deposition via inkjet printing including fabrication of 3D structures,[33-35] conductive coatings[36-42] and wires.[37-40]

In coffee-ring deposition, particles within the droplet are carried to the contact line by outward, radial, capillary flows and deposited, Figure 2-6.

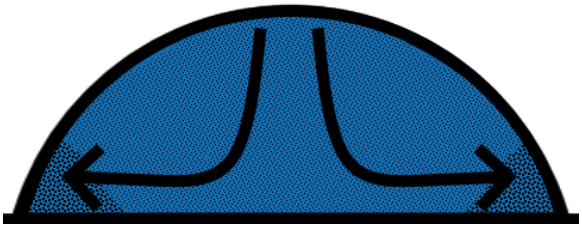

Figure 2-6. Coffee-ring deposition via radially outward capillary flow.

The particle deposits reinforce pinning at the contact line and the process continues until complete evaporation is reached. In the event that the droplet contact line is not pinned, particles carried to the edge of the droplet are deposited in mound formation, where the receding contact line limits the degree of deposition at the initial droplet radius but deposition is increased towards the center of the droplet. Further, stick-slip motion of the contact line can lead to concentric ring deposits where particles can deposit rings when the contact line is pinned after which the contact line will recede until it becomes pinned once more and a new deposition ring can be established. Thus the evaporation mode of drying droplets is critical to the formation of coffee-rings.

Constant contact area evaporation can be a result of surface pinning, where the droplet is pinned to the substrate and cannot move during evaporation. Pinning can result from any combination of van der Waals interactions on surfaces with high roughness, hydrogen bonding, or

electrostatic interactions with the substrate. This results in the height of the droplet decreasing during evaporation, yet the contact area remains constant. Surface pinning of the contact line is reinforced by particles transported to this boundary creating a stronger pinning effect. This suggests that evaporating under constant contact angle conditions where the contact area shrinks during drying can change the deposition profile. Deegan has shown this can lead to mound shaped depositions.[43]

Slowing the evaporation rate by modifying the environmental atmosphere reducing the concentration gradient between the liquid and vapor phases can lead to uniform depositions.[44] Evaporation under these conditions reduces the magnitude of capillary flows developed within the droplet which thereby hinders transport of suspended particles to the contact line. Evaporation completes before, in this case, particles reach an equilibrium position resulting in greater surface coverage of suspended particles.

Another modification to the flow profile within the droplet, generating inward Marangoni flows, can counteract the outward capillary flow which would normally result in coffee-ring deposits. Marangoni flows are developed when surface tension gradient on the surface of the droplet creates a shear stress which drives a flow on the underlying layers of fluid and leads to the development of recirculating flows. These flows are often driven by local temperature differences which alter the local surface tension, such as between the apex of the droplet and the contact line. When the edge of the droplet is cooler than its apex, outward radial Marangoni flows develop.[45] When the apex is cooler than the body, inward Marangoni flows arise which can entrain particles radially inward from the contact line to the apex. In this case hill shaped deposits can form.[46]

In most applications, it is desirable to restrict the formation of coffee-ring deposits, particularly where uniform surface coatings are desired. Recent literature has revealed several

opportunities to control particle deposition, leading to more uniform deposits. Coffee-ring suppression has been achieved through three mechanisms which aim to prevent a critical process in coffee-ring formation: (1) eliminating contact line pinning (2) disrupting capillary flows and (3) preventing particle motion to the contact line.[47]

2.2.2.1 Contact Angle Hysteresis

Moving contact lines during evaporation do not lead to coffee-ring deposits.[48, 49] Several coffee-ring prevention strategies thus revolve around preventing contact line pinning. This can be achieved through modification of the contact angle and contact angle hysteresis.

Typically, droplets with contact angles less than 90° dry with pinned contact lines[32, 45, 50-54] and those with contact angles greater than 90° evaporate instead with receding contact lines and constant contact angles.[51, 53-55] However, equilibrium contact angle measurements are not sufficient to evaluate pinning behavior during evaporation and can often be better explained through quantification of contact angle hysteresis (CAH). CAH is the difference in advancing, θ_a, and receding, θ_r, contact angles within a droplet with respect to the direction of applied force such as gravity in a water droplet held on a vertical window, Figure 2-7.[56]

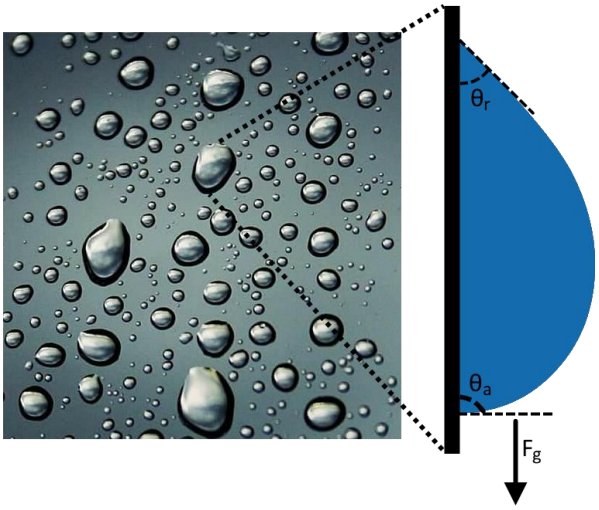

Figure 2-7. Contact angle hysteresis in a droplet on a vertical window subject to gravity. Water droplets on window adapted from https://pixabay.com/photos/drops-rain-window-lights-3141603/

CAH can be measured through careful addition or removal of liquid to a droplet with a syringe while monitoring contact angle during the change in volume or with goniometry performed on inclined surfaces where droplets are subject to gravity.[53]

In regards to surface pinning, evaporating droplets will remain pinned while having contact angles greater than the receding contact angle and less than the advancing contact angle, following Equation (2).[56]

$$\theta_r < \theta < \theta_a \quad (2)$$

Therefore, systems with small CAH are more susceptible to perturbations in contact angle which can lead to depinning, whereas, large CAH systems are more accommodating to contact angle changes while drying and can remain pinned throughout the entire process.[48, 49, 57] Further, θ_r and θ_a are functions of local surface roughness and inhomogeneities.[58] Such that pinning is largely governed by surface roughness and liquid-substrate interactions.

Modifying the pinning behavior of sessile droplets can therefore be instrumental in preventing coffee-ring deposition and can be achieved by modifying surface chemistry or roughness. These approaches can be implemented physically through lithographic patterning of substrates or chemically through surface modification with polymeric monolayers to induce hydrophobicity.

Chemical substrate modification with monolayers of hydrophobic polymers has been implemented successfully to create hydrophobic surfaces that suppress the coffee-ring effect. Ko et al. used self-assembled monolayers of octadecyltrichlorosilane on Si wafers generate a

hydrophobic substrate for inkjet printing of colloidal inks resulting in uniform deposits with a high degree of packing.[59, 60] However, this technique may consequently modify the surface roughness and thus CAH measurements should be performed post-treatment to ensure the undesired pinning behavior is suppressed.

Physical coffee-ring suppression techniques revolve around the fabrication of patterned substrates resembling closely spaced linear grooves and have also been shown to produce hydrophobic and superhydrophobic interactions.[60] Two theoretical models have been developed to describe interactions on such patterned substrates, namely the Cassie[61] and Wenzel[62] models. Cassie and Baxter describe the formation of air pockets trapped in the grooves of rough or patterned substrates which generate an additional liquid-vapor interface supporting the droplet, Figure 2-8.[61] Thus roughness contributes to increasing hydrophobicity. Wenzel understood surface roughness to increase the wetting behavior of the substrate such that roughened hydrophilic and hydrophobic substrates would become increasingly hydrophilic hydrophobic, respectively, due to an increase in surface area.[62] As a result, droplets would fill the space created by the rough surface, Figure 2-8.

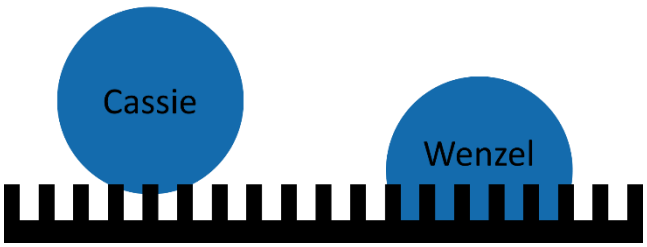

Figure 2-8. Cassie (left) and Wenzel (right) droplets on a patterned superhydrophobic substrate.

The transition between the two states has been shown to revolve around the balance of the Laplace, Equation (3), and capillary pressures, Equation (4),

$$P_L = \frac{2\gamma}{R} \tag{3}$$

$$P_c = -4\gamma cos\theta_Y \left(\frac{\phi}{w(1-\phi)}\right) \tag{4}$$

where γ is the liquid surface tension, R is the droplet radius, θ_Y is the Young's contact angle, ϕ is the solid surface volume fraction, and w is the pillar width.[47, 63] When Laplace pressure is greater than the capillary pressure Cassie droplets transition to the Wenzel state.[64]

Coffee-ring suppression was achieved by Dicuangco in Cassie droplets on superhydrophobic Teflon-coated substrates with patterned micropillars, yet Wenzel droplets in the same study maintained coffee-ring deposits.[64] While the Wenzel state is commonly associated with pinned contact lines and thus coffee-ring formation, Dai et al. demonstrated that Wenzel droplets can have moving contact lines in superhydrophobic patterned substrates with lubrication applied to the solid interface.[65] Further Cui et al. demonstrated that evaporation of Wenzel droplets can suppress the coffee-ring effect due to modification of the flow profile within the droplet during drying primarily due to the inward growth of a porous gel near the edge of the droplet pushing flow inward.[66]

2.2.2.2 Electronic Effects

Electronic manipulation of droplet interactions with a substrate can eliminate coffee-ring deposits in evaporating suspensions through modification of CAH or through stimulation of the contact line. The electrocapillary effect developed by Lipmann describes the tendency of liquids to deform their contact angles in response to an applied electric field.[67, 68] Later coined electrowetting, a droplet placed on a conductive substrate with a thin coating of a dielectric material is applied an electric field through a thin wire, Figure 2-9.

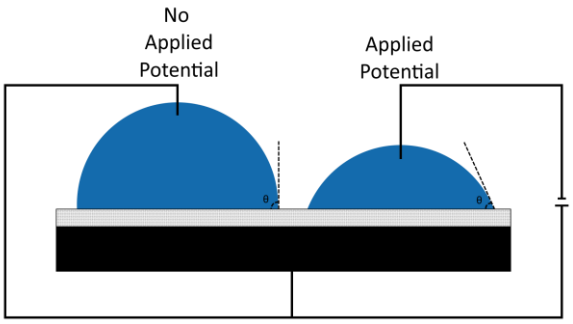

Figure 2-9. Electrowetting of a droplet resting on a thin layer of dielectric coating on top of a conductive material in response to an applied voltage.

Electric fields for electrowetting can be resultant from either direct (DC) or alternating current (AC) and the contact line behavior for each mode is distinct. Electrowetting with DC fields smooths the motion of contact lines which tend to recede in a stick-slip fashion without an applied field. Thus, DC electrowetting has been utilized to prevent concentric ring deposits and promote uniform deposition.[69] Alternatively, electrowetting with AC fields generates oscillatory contact line motion which prevents pinning of the contact line during evaporation.[70, 71] Furthermore, the boundary oscillations drive secondary fluid motion competing with the evaporative capillary flow resulting in uniform deposits.[72-74] Frequency of the applied AC field has been shown to impact the coffee-ring suppression of AC electrowetting in that a critical frequency exists such that above which coffee-ring deposition is restored.[74]

2.2.2.3 Capillary Flow Disruption

Suppression of the coffee-ring effect can be established through the disruption of radially outward capillary flow generated in evaporating sessile droplets. The introduction of secondary flows, which compete with the capillary flow, will reduce the tendency of entrained particles to be transported to the contact line thereby limiting the development of coffee-rings. Recent research

has shown that manipulation of the capillary flow within droplets during evaporation can reverse the coffee-ring effect and lead to more uniform deposits, typically mound shaped.[75]

Kim et al. developed a device to impart electroosmotic flow on drying sessile droplets and characterized the resulting deposition patterns. They revealed that through control over the direction of the applied electroosmotic field they could enhance or suppress the coffee-ring effect. An inward induced flow, with an electroosmotic strength parameter of -0.025 balanced the outward capillary flow and was found to have a uniform deposition pattern.[76]

Marangoni flow has seen a great deal of recent interest regarding suppression of the coffee-ring effect. Commonly observed near the meniscus of wine in a glass, where small drops of wine travel up the curved surface of the glass before reaching a critical height and falling back into the bulk. The upward motion is driven by the Marangoni effect through a gradient in surface tension between the bulk surface of the wine and the wine near meniscus. The surface tension of wine at the edge of the glass is stronger due to a non-uniform evaporation profile resulting in preferential evaporation of alcohol which leaves behind a water-rich phase with a greater surface tension thereby pulling wine up the wall of the glass.[77]

The Marangoni effect is therefore described by flow induced by surface tension gradients on the surface of an evaporating liquid which induce a shear stress on the liquid interface in order to balance the surface tension.[78] Surface tension gradients in evaporating droplets can result from temperature or surfactant concentration gradients. The former, deemed the thermal Marangoni effect develops due to a non-linear evaporative flux as a function of radial position. The thermal Marangoni stress is given by Equation (5),

$$\frac{d\sigma}{dr} = \frac{d\sigma_T}{dT}\frac{dT}{dr} \tag{5}$$

where σ_T is the surface tension, T is the temperature, and r is the radial position.[79] For small temperature deviations, the surface tension often decreases as temperature increases such that Equation (6) maintains a constant value, $-0.1657\,\frac{mN}{m\,^\circ C}$ for water.[79]

$$\frac{d\sigma_T}{dT} = \beta \tag{6}$$

Likewise, the Marangoni stress due to surfactant concentration gradients is given by Equation (7),

$$\frac{d\sigma}{dr} = -\frac{d\sigma_s}{dv}\frac{dv}{dr} \tag{7}$$

Where, v is the areal number density of surfactant molecules and σ_s is the surfactant induced surface tension given by Equation (8),

$$\sigma_s = -vk_BT \tag{8}$$

where, k_B is the Boltzmann constant.[79] Finally, in systems where both temperature and surfactant induced surface tension gradients exist, the complete Marangoni stress is given by Equation (9).[79]

$$\frac{d\sigma}{dr} = \frac{d\sigma_T}{dT}\frac{dT}{dr} - \frac{d\sigma_s}{dv}\frac{dv}{dr} \tag{9}$$

Marangoni stresses generate recirculating flows within evaporating sessile droplets and the direction of recirculation can be controlled through the direction of the surface tension gradient.[79] When evaporation-induced cooling is greatest at the apex of the drop and the base of the drop is in thermal equilibrium with the substrate, Marangoni flow carries solutes or particles that are near the surface of the drop radially inward toward the apex. However, outward Marangoni flows are

also possible and can be observed when the edge of a drop becomes cooler than its apex.[45] The droplet and substrate thermal conductivities have been shown experimentally[80] and theoretically[81] to impact the temperature profile within and evaporating droplet. The ratio of the solid, k_s, and liquid, k_l, thermal conductivities, Equation (10), is central to controlling this behavior.

$$k_r = \frac{k_s}{k_l} \tag{10}$$

When $k_r < 1.45$, the droplet is coolest at its contact line and recirculation with inward flow along the liquid-substrate interface develops, however, $k_r > 2$ leads to warmer contact lines and recirculation with outward radial flow along the liquid-substrate interface.[82] Xu later improved upon Ristenpart's analysis and suggested a new dimensionless group, Equation (11), governing the direction of circulatory flow driven by the Marangoni effect.[83]

$$R_N = \frac{h_s k_l}{R k_s} \tag{11}$$

Where h_s is the thickness of the substrate and R is the radius of the droplet. Further the direction of Marangoni flow was found to be a function of contact angle through Equation (12),

$$\alpha(\theta) = \frac{sin2\theta - 4\lambda \tan\left(\frac{\theta}{2}\right)}{4\lambda + 2\sin^2\theta} \tag{12}$$

where θ is the contact angle and λ is given by Hu and Larson as $\lambda = \frac{1}{2} - \frac{\theta}{\pi}$.[83, 84] When $R_N > \alpha(\theta)$, Marangoni flow drives radial outward circulation and when $R_n < \alpha(\theta)$ the current direction reverses.[83]

Several groups have also reported the occurrence of stagnation points near the edge of the drop which locally change the direction of flow, either due to a sudden change in the direction of

the surface tension gradient[78] or due to the opposing effects of the outward capillary and inward Marangoni flow.[85]

The introduction of recirculating Marangoni flow, in either direction has been shown to reduce the deposition of particles at the contact line.[82, 86, 87] However, complete coffee-ring suppression is best established by Marangoni currents which flow radially inward at the droplet-substrate interface, which can lead to hill-shaped deposits in the center of the drop.[46] Further, suppression has been achieve through both temperature and concentration induced Marangoni flow.

Evaporation of water at room temperature has weak Marangoni flow due to minute temperature gradients during drying.[79] Thus, elevated substrate temperatures are required to create the necessary surface temperature gradients to drive flow and to suppress the coffee ring effect.[88, 89] Alternatively, heating with laser irradiation has also been implemented to develop thermal Marangoni flow without heating the substrate.[90]

Introduction of additional species has widely implemented to suppress the coffee-ring effect through concentration dependent surface tension gradients. Commonly either surfactants[91-98] or solvent mixtures[87, 99-101] accomplish this goal. Yet both methods require incorporating additional molecules into the evaporating droplets which can have undesirable consequences relating to desired chemistry in manufacturing processes.

2.2.2.4 Particle-Interface Interactions

In addition to modifying the substrate's surface energy or creating secondary flow fields, modification to the suspended particles geometry and chemistry can subdue coffee-ring deposition. Here, the particles are modified in such a way as to have an unfavorable interaction with the continuous phase and thus preferring the vapor phase. Particles which preferentially favor the

vapor phase will migrate towards the interface during evaporation and will not be entrained by capillary flow. Further, colloidal particles resting at the liquid-vapor interphase distort the local shape of the interface, Figure 2-10, leading to additional capillary flow within this region which pulls the particles together.[102-104]

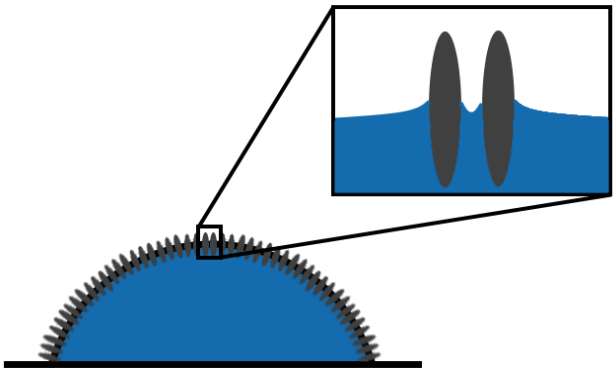

Figure 2-10. Ellipsoidal particle-water-vapor interface

Altering particle-particle interactions to achieve attractive as opposed to repulsive forces leads to aggregation. When such agglomerates reach a critical threshold in size and structure, they will withstand the capillary flow and deposit on the substrate without non-uniformities at the droplet periphery.[105-107]

Lastly, performing quick evaporation of sessile droplet suspensions can lead to the dispersed phase becoming confined at the liquid-vapor interface when the evaporation rate is faster than the ability for the particles to diffuse away from the interface, expressed in Equation (13).[108]

$$t_{evap} < 2\sqrt{\frac{Dt}{\pi}} \tag{13}$$

2.3 Fluid Flow in Evaporating Sessile Droplets

Fluid flow in evaporating droplets is a complex, multidimensional, and multiphysical phenomenon involving heat, mass, and fluid transport interacting concurrently. Fluid and mass transport in evaporating sessile droplets have been studied extensively as the common occurrence appears in a plethora of industrial processes.[109] To a lesser extent, the evaporation of sessile droplets containing suspended spherical particles have also been studied.[95, 110] However, there has been minimal investigation of the evaporating droplets containing non-spherical particles. Nevertheless, non-spherical particles present exciting opportunities in the development of patterning materials with anisotropic properties and evaporation induced self-assembly (EISA) provides a facile strategy for deposition of unique particle orientations.

2.3.1 Evaporation induced flow

Typically, evaporation of small droplets proceed with a spherical geometry, but is dependent on the three-phase interactions between vapor-liquid, liquid-solid, and vapor-solid surface tensions as well as the relationship between surface tension and gravitational forces described by the Bond number, Equation (14).

$$Bo = \frac{\Delta \rho g r^2}{\gamma} \tag{14}$$

Water droplets less than 3 mm can be described by surface tension which acts to maintain a spherical geometry. Water on hydrophobic substrates, Figure 2-11, have high contact angles and maintain close to spherical geometries. In contrast, small water droplets on hydrophilic substrates have low contact angles but maintain the spherical curvature required by surface tension acting to minimize surface area. In this case these droplets develop a spherical cap geometry comparable to the volume outside a planar slice of a sphere.

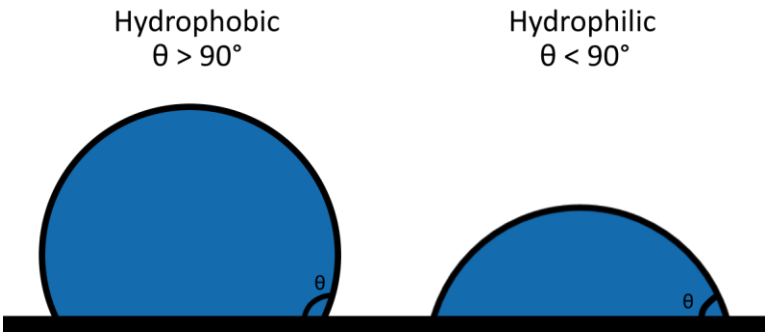

Figure 2-11. Droplet geometry as a function of liquid-substrate interactions.

Consequently, water on hydrophobic substrates can be modeled with the lubrication approximation where the droplet height is much less than its radius. Additional dimensional reduction can be realized by the droplets' rotational symmetry. Thus, water droplet evaporation on hydrophilic substrates is commonly modeled as 1-dimensional evaporation following lubrication theory for convection and diffusion.

2.3.2 Pure Liquids

Deegan et al. explored the evaporation of droplets containing suspended particles and its relevance to the coffee-ring effect. In particular, Deegan et al. focused on the evaporative flux of water during evaporation as a function of the droplet shape which is independent of the presence of suspended particles and approximated by Equation (15).[43]

$$J(r,t) = J_0(\theta)(1-\tilde{r}^2)^{-\lambda(\theta)} \tag{15}$$

Where $\tilde{r}$ is the dimensionless radial coordinate and $J_0(\theta)$ and $\lambda(\theta)$ are empirical relationships expressed as Equations (16) and (17) respectively.[84]

$$J_0(\theta) = \frac{Dc_v(1-H)}{R}(0.27\theta^2 + 1.30)\left(0.6381 - 0.2239\left(\theta - \frac{\pi}{4}\right)^2\right) \tag{16}$$

$$\lambda(\theta) = \frac{1}{2} - \frac{\theta}{\pi} \tag{17}$$

Where D is the diffusivity, c_v is the saturation vapor pressure of water, H is the humidity and R is the droplet radius. Hu and Larson developed a rigorous model for the evaporation of pure water droplets on a hydrophilic substrate following the lubrication approximation and Deegan's analysis of the evaporative flux.[84] Analytical solutions for the dimensionless radial and vertical velocities are reported in Equations (18) and (19) respectively.[84]

$$\begin{aligned}\tilde{u}_r = \frac{3}{8}\frac{1}{1-\tilde{t}}\frac{1}{\tilde{r}}\left[(1-\tilde{r}^2) - (1-\tilde{r}^2)^{-\lambda(\theta)}\right]\left(\frac{\tilde{z}^2}{\tilde{h}^2} - 2\frac{\tilde{z}}{\tilde{h}}\right) \\ + \left\{\frac{\tilde{r}h_0^2\tilde{h}}{R^2}\left(\tilde{J}\lambda(\theta)(1-\tilde{r}^2)^{\lambda(\theta)-1} + 1\left(\frac{\tilde{z}}{\tilde{h}} - \frac{3}{2}\frac{\tilde{z}^2}{\tilde{h}^2}\right)\right)\right\}\end{aligned} \tag{18}$$

$$\begin{aligned}\tilde{u}_z = \frac{3}{4}\frac{1}{1-\tilde{t}}\left[1 + \lambda(\theta)(1-\tilde{r}^2)^{-\lambda(\theta)-1}\right]\left(\frac{\tilde{z}^2}{3\tilde{h}^2} - \frac{\tilde{z}^2}{\tilde{h}}\right) \\ + \frac{3}{2}\frac{1}{1-\tilde{t}}\left[(1-\tilde{r}^2) - (1-\tilde{r}^2)^{-\lambda(\theta)}\right]\left(\frac{\tilde{z}^2}{2\tilde{h}^2} - \frac{\tilde{z}^3}{3\tilde{h}^3}\right)\tilde{h}(0,\tilde{t}) \\ - \left\{\frac{h_0^2}{R^2}\left(\tilde{J}\lambda(\theta)(1-\tilde{r}^2)^{-\lambda(\theta)-1} + 1\right)\left(\tilde{z}^2 - \frac{\tilde{z}^3}{\tilde{h}}\right)\right. \\ + \frac{\tilde{r}h_0^2}{R^2}\tilde{J}\lambda(\theta)(\lambda(\theta)+1)(1-\tilde{r}^2)^{-\lambda(\theta)-2}\left(\tilde{z}^2 - \frac{\tilde{z}^3}{\tilde{h}}\right) \\ \left. - \frac{\tilde{r}h_0^2}{R^2}\left(\tilde{J}\lambda(\theta)(1-\tilde{r}^2)^{-\lambda(\theta)-1} + 1\right)\left(\frac{\tilde{z}^3}{\tilde{h}^2}\right)\tilde{h}(0,\tilde{t})\right\}\end{aligned} \tag{19}$$

Hu and Larson further extended their model to incorporate the Marangoni effect on the fluid flow.[79]

2.3.3 Particle Suspensions and Particle-Particle Interactions

Fluid transport in particle suspensions introduce a great deal of complexity relating to the particle interactions with solvent, vapor, solid, and other particles. Additionally, the effects of scale

between the interactions and the macroscopic fluid flow introduce further complications to fluid dynamic modeling.

At the macroscopic level, particle interactions are predominantly considered through their influence on viscosity.[111] As described by DLVO theory, colloidal particles in suspension are stabilized through a balance between attractive van der Waals forces and repulsive electrostatic interactions.[112, 113] These interactions restrict the mobility of particles within the suspension as a function of concentration. As the number density, v, increases from dilute, $v < \frac{1}{L^3}$, to semi-dilute to concentrated, $v > \frac{1}{dL^2}$, according to Doi and Edwards, the strength of interparticle interaction is increased.[114] This is observed through the rotational diffusivity and viscosity for concentrated suspensions of rigid rods given in Equations (20), (21), and (22).[114]

$$D_r = \beta D_{r_0} \left(\frac{1}{vL^3}\right)^2 \tag{20}$$

$$D_{r_0} = \frac{2k_B T(\ln(p) - 0.8)}{\pi \eta_s L^3} \tag{21}$$

$$\eta \approx \eta_s + \frac{vk_B T}{30D_{r_0}} + \frac{vk_B T}{10D_r} \tag{22}$$

In Equation (20), β is fitting parameter, L, is the rigid rod length, v is the number density of particles, and D_{r_0} is the rotational diffusivity in dilute suspension. In Equation (21), k_B is the Boltzmann constant, T is the temperature, p is the particle aspect ratio, and η_s is the solvent viscosity.

Recently, Mansfield and Douglas highlighted the importance of modeling correct particle geometries. Traditional modeling of rod-like particles through ellipsoids,[115] which are simpler computationally, are inaccurate and more rigorous modeling of the shape-dependence of intermolecular interactions on viscosity should be evaluated.[111] Additionally, they highlighted the importance of polydispersity on the intrinsic viscosity of a suspension, where real suspensions often do not have a uniform size distribution and as a result the distribution in shape has a relevant influence on viscosity.[111] Finally, Bhardwaj et al. and Xu et al. have recently incorporated the effects of DLVO interactions into their simulations of evaporating droplet suspensions to account for the attractive forces between the substrate and suspended particles which aids deposition.[116, 117]

2.4 Transient Diffusion in Thin Films

In contrast to evaporation, the diffusion of water into CNC-polymer composites is of unique interest to the development of mechanically adaptive materials. Here we explore Fickian and non-Fickian diffusion acting in a single dimension to transport water into a CNC and thermoplastic polyurethane composite (TPU).

2.4.1 Fickian Diffusion

Fickian diffusion follows the transport of water according to Fick's second law, Equation (23), where the migration of a species is dependent on its spatial concentration gradient and a proportionality constant. The proportionality constant takes the form of a diffusivity, *D*, which represents the rate transport of a differential unit of area containing the diffusing species.

$$\frac{\partial c}{\partial t} = D\nabla^2 c \tag{23}$$

Where *c* is the concentration of the diffusing species and *t* is time. In one dimension, Fick's second law reduces to Equation (24).

$$\frac{\partial c}{\partial t} = D\frac{\partial^2 c}{\partial z^2} \tag{24}$$

Finally, the analytical solution for mass uptake is given in Equation (25) where D is the diffusivity and h is the diffusion length.[118]

$$\frac{m - m_i}{m_\infty - m_i} = 1 - \frac{8}{\pi^2}\sum_{j=1}^{\infty}\frac{1}{(2j+1)^2}e^{-\left[\frac{(2j+1)^2\pi^2 Dt}{h^2}\right]} \tag{25}$$

2.4.2 Non-Fickian Diffusion

When diffusive transport is not solely driven by concentration gradients it is said to be non-Fickian. Such deviations are characterized as anomalous behavior and can be realized in many polymeric and biological systems. Examples of anomalous behavior are characterized by an overshoot in mass uptake and the presence of a secondary equilibrium indicated by an additional plateau at long times.[119]

Carter and Kibler introduced one such model to account for non-Fickian behavior which differentiates between bound and mobile species. Where bound species are hindered or otherwise restricted from diffusive transport by either physical or chemical interactions.[119] Mobile species diffuse as a result of concentration gradients. In one dimension, Carter and Kibler's hindered diffusion model is represented by Equations (26) and (27).[119]

$$\frac{\partial n}{\partial t} + \frac{\partial N}{\partial t} = D\frac{\partial^2 n}{\partial z^2} \tag{26}$$

$$\frac{\partial N}{\partial t} = \gamma n - \beta N \tag{27}$$

Where n and N are the concentration of mobile and bound species respectively. The probabilities of mobile species becoming bound, γ, and of bound species becoming mobile, β,

describe the ability of both species to transition between states as they continue to diffuse. Carter and Kibler also provided the analytical solution for the mass uptake as a function of time given in Equations (28), (29), and (30) where D is the diffusivity and 2δ is the diffusion distance.[119]

$$\frac{m_t}{m_\infty} = 1 - \frac{8}{\pi^2} \sum_{l=1}^{\infty(odd)} \frac{r_l^+ e^{-r_l^- t} - r_l^- e^{-r_l^+ t}}{l^2 (r_l^+ - r_l^-)} + \frac{8}{\pi^2} \frac{\kappa\beta}{\gamma + \beta} \sum_{l=1}^{\infty(odd)} \frac{e^{-r_l^- t} - e^{-r_l^+ t}}{r_l^+ - r_l^-} \tag{28}$$

$$r_l^{\pm} = \frac{1}{2}\left[(\kappa l^2 + \gamma + \beta) \pm \sqrt{(\kappa l^2 + \gamma + \beta)^2 \pm 4\kappa\beta l^2}\right] \tag{29}$$

$$\kappa = \frac{\pi^2 D}{(2\delta)^2} \tag{30}$$

The hindered diffusion model was developed to capture the absorption of water in polymers in humid environments and was originally found to apply very well except at exceedingly long times, > 100 days, where the tested resins experienced increasingly non-Fickian behavior following a secondary plateau in their mass uptake. More recently, however, a number of researchers have found utility in this formulation.[120-123]

2.5 Mechanically Adaptive Materials

Materials which respond mechanically to stimuli are of increasing interest in recent years especially in the development of smart materials.[124-126] Mechanically adaptive materials can respond to a variety of stimuli including but not limited to humidity, pH, solvent exposure, temperature, and electromagnetic radiation. These changes can result in modifications to one or more of a materials' mechanical properties, shape, or morphology. Thus they can be readily used in the design of both sensors and actuators which operate in response to a given stimulus. In some

cases, these materials can develop memory of a preprogrammed shape where the stimulus can trigger the material to return to is preferred configuration.[127]

2.5.1 Mechanically Adaptive CNC Composites

CNCs have been widely used in recent years as fillers in nanocomposite systems either to provide mechanical reinforcement[128, 129] or introduce mechanical adaptivity.[130] Early development of CNC-based mechanically adaptive materials aimed to develop reinforced shape memory properties[131] or were inspired by the ability of sea cucumbers to modulate the stiffness of their dermises.[132] In the latter case, CNCs were incorporated in an ethylene oxide-epichlorohydrin copolymer and exhibited a drastic decrease in modulus, 814 to 10.8 MPa, upon the introduction of an artificial cerebrospinal fluid.[132] Additionally, Capadona et al. reported an approximately two fold increase in storage modulus upon adding 20 % CNCs by volume.[132] CNCs have been incorporated into a variety of polymers including polyvinyl acetate and polyurethanes in order to take advantage of these reinforcing properties in conjunction with their mechanical response to stimuli.[130, 131, 133-141]

Such composites rely on the reinforcement of CNCs through interparticle hydrogen bonding. Above a critical concentration, X_c, given in Equation (31), relative to the particle aspect ratio, p, these composites develop a percolating network such that a continuous pathway of CNCs through the matrix develops and connections via interparticle hydrogen bonding is established.[132]

$$X_c = \frac{0.7}{p} \tag{31}$$

This hydrogen bonding network enables the mechanical adaptivity through solvent interactions. In particular, solvents competing for the hydrogen bonding sites on CNC particles will break up the network and thus hamper their reinforcement, illustrated in Figure 2-12.[132, 142]

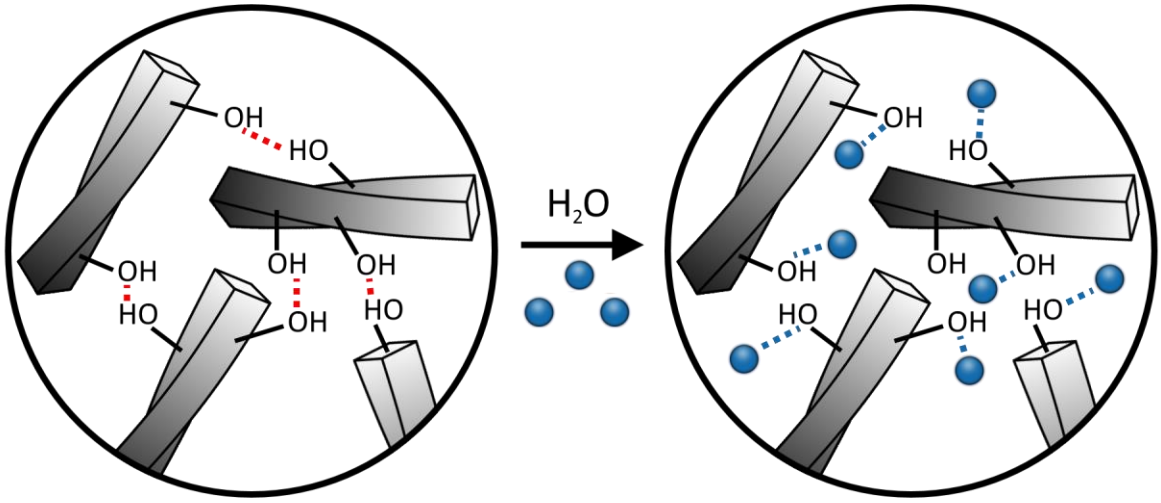

Figure 2-12. Mechanism for mechanical adaptivity in CNC-polymer composites. Water competes with hydrogen bonding between CNCs in the dry state

Further, the reversibility of this phenomenon follows as solvent is removed from the system, CNCs may once again develop interparticle hydrogen bonds and form its network structure.

Although orientation of rod-shaped particle composites is expected to contribute to the total reinforcement, few studies have explored this avenue with CNCs. Fallon et al. showed there was a minimal effect of orientation on both the mechanical adaptivity and reinforcement in samples prepared with uniaxial orientation compared to isotropically oriented CNCs.[140] However, concentration appears to play a primary role in developing a percolating network of CNCs to provide reinforcement and introduce softening in the presence of water.

2.5.2 Mechanical models in CNC composites

The modulus of CNC composites has been successfully predicted by Percolation and Halpin-Kardos models in both the dry and wet states, respectively. The Halpin-Kardos model

describes the wet state modulus due to its assumption of lack of interparticle interactions whereas the percolation model describes the dry state modulus while considering interactions between filler particles.

The Halpin-Kardos model treats the composite as a homogeneous matrix such that the material is treated as a continuum and the composite modulus, E_c, is given by Equations (32) and (33).[131, 143, 144]

$$E_c = \frac{1 + 2p\eta\phi_f}{1 - \eta\phi_f} \tag{32}$$

$$\eta = \frac{\frac{E_f}{E_m} - 1}{\frac{E_f}{E_m} + 2p} \tag{33}$$

Where p is the aspect ratio, ϕ_{CNC} is the filler volume fraction, and E_f and E_m are the filler and matrix moduli respectively.

The percolation model allows for interparticle interactions, such as hydrogen bonding between CNCs, via its dependence on the critical percolation concentration, X_c. Above this critical value, the filler particles are assumed to interact strongly, providing substantial reinforcement to the matrix. Thus the composite modulus can be evaluated as a function of filler volume fraction, ϕ_f, and X_c as demonstrated by equations (34) and (35).[144-146]

$$E_c = \frac{\left(1 - 2\psi + \psi\phi_f\right)E_s E_r + \left(1 - \phi_f\right)\psi E_r^2}{\left(1 - \phi_f\right)E_r + \left(\phi_f - \psi\right)E_s} \tag{34}$$

$$\psi = \begin{cases} 0 & \phi_{CNC} < X_c \\ \phi_f \left(\frac{\phi_f - X_C}{1 - X_c} \right)^{0.4} & \phi_{CNC} > X_c \end{cases} \quad (35)$$

Taken together, the suitability of both the percolation and Halpin-Kardos models to describe the interactions of CNC composites strongly suggests the development of a percolating network of CNCs which is broken upon the introduction of water.[128, 135-137] Thus, it follows that the mechanical softening mechanism is rooted in the competition between CNC-CNC hydrogen bonds and CNC-H_2O hydrogen bonds. As water replaces interparticle interactions, these particles are reduced in their ability to participate in mechanical reinforcement thereby softening the material.

References

1. Montanari, S.; Roumani, M.; Heux, L.; Vignon, M. R., Topochemistry of Carboxylated Cellulose Nanocrystals Resulting from TEMPO-Mediated Oxidation. *Macromolecules* **2005,** *38* (5), 1665-1671.
2. Hamad, W. Y., *Cellulose Nanocrystals Properties, Production, and Applications*. John Wiley & Sons Ltd: 2017; p 289.
3. Revol, J. F.; Bradford, H.; Giasson, J.; Marchessault, R. H.; Gray, D. G., Helicoidal self-ordering of cellulose microfibrils in aqueous suspension. *International Journal of Biological Macromolecules* **1992,** *14* (3), 170-172.
4. Mu, X.; Gray, D. G., Droplets of cellulose nanocrystal suspensions on drying give iridescent 3-D "coffee-stain" rings. *Cellulose* **2015,** *22* (2), 1103-1107.
5. Camarero Espinosa, S.; Kuhnt, T.; Foster, E. J.; Weder, C., Isolation of thermally stable cellulose nanocrystals by phosphoric acid hydrolysis. *Biomacromolecules* **2013,** *14* (4), 1223-30.
6. Lavoine, N.; Desloges, I.; Dufresne, A.; Bras, J., Microfibrillated cellulose - its barrier properties and applications in cellulosic materials: a review. *Carbohydr Polym* **2012,** *90* (2), 735-64.
7. Sturcova, A.; Davies, G. R.; Eichhorn, S. J., Elastic modulus and stress-transfer properties of tunicate cellulose whiskers. *Biomacromolecules* **2005,** *6* (2), 1055-61.
8. Moon, R. J.; Martini, A.; Nairn, J.; Simonsen, J.; Youngblood, J., Cellulose nanomaterials review: structure, properties and nanocomposites. *Chem Soc Rev* **2011,** *40* (7), 3941-94.
9. Foster, E. J.; Moon, R. J.; Agarwal, U. P.; Bortner, M. J.; Bras, J.; Camarero-Espinosa, S.; Chan, K. J.; Clift, M. J. D.; Cranston, E. D.; Eichhorn, S. J.; Fox, D. M.; Hamad, W. Y.; Heux, L.; Jean, B.; Korey, M.; Nieh, W.; Ong, K. J.; Reid, M. S.; Renneckar, S.; Roberts, R.; Shatkin, J. A.; Simonsen, J.; Stinson-Bagby, K.; Wanasekara, N.;

Youngblood, J., Current characterization methods for cellulose nanomaterials. *Chem Soc Rev* **2018,** *47* (8), 2609-2679.
10. Yu, H.-Y.; Qin, Z.-Y.; Liu, L.; Yang, X.-G.; Zhou, Y.; Yao, J.-M., Comparison of the reinforcing effects for cellulose nanocrystals obtained by sulfuric and hydrochloric acid hydrolysis on the mechanical and thermal properties of bacterial polyester. *Composites Science and Technology* **2013,** *87*, 22-28.
11. Brinchi, L.; Cotana, F.; Fortunati, E.; Kenny, J. M., Production of nanocrystalline cellulose from lignocellulosic biomass: technology and applications. *Carbohydr Polym* **2013,** *94* (1), 154-69.
12. Alexander B. Reising, R. J. M., Jeffrey P. Youngblood, Effect of Particle Alignment on Mechanical Properties of Neat Cellulose Nanocrystal Films. *Journal of Science & Technology for Forest Products and Processes* **2012,** *2* (6), 32-41.
13. Dumanli, A. G.; van der Kooij, H. M.; Kamita, G.; Reisner, E.; Baumberg, J. J.; Steiner, U.; Vignolini, S., Digital color in cellulose nanocrystal films. *ACS Appl Mater Interfaces* **2014,** *6* (15), 12302-6.
14. Tardy, B. L.; Ago, M.; Guo, J.; Borghei, M.; Kamarainen, T.; Rojas, O. J., Optical Properties of Self-Assembled Cellulose Nanocrystals Films Suspended at Planar-Symmetrical Interfaces. *Small* **2017,** *13* (47).
15. Cranston, E. D.; Gray, D. G., Birefringence in spin-coated films containing cellulose nanocrystals. *Colloids and Surfaces A: Physicochemical and Engineering Aspects* **2008,** *325* (1-2), 44-51.
16. Tatsumi, M.; Teramoto, Y.; Nishio, Y., Different orientation patterns of cellulose nanocrystal films prepared from aqueous suspensions by shearing under evaporation. *Cellulose* **2015,** *22* (5), 2983-2992.
17. Chen, S.; Schueneman, G.; Pipes, R. B.; Youngblood, J.; Moon, R. J., Effects of crystal orientation on cellulose nanocrystals-cellulose acetate nanocomposite fibers prepared by dry spinning. *Biomacromolecules* **2014,** *15* (10), 3827-3835.
18. Tatsumi, M.; Kimura, F.; Kimura, T.; Teramoto, Y.; Nishio, Y., Anisotropic polymer composites synthesized by immobilizing cellulose nanocrystal suspensions specifically oriented under magnetic fields. *Biomacromolecules* **2014,** *15* (12), 4579-4589.
19. De France, K. J.; Yager, K. G.; Hoare, T.; Cranston, E. D., Cooperative Ordering and Kinetics of Cellulose Nanocrystal Alignment in a Magnetic Field. *Langmuir* **2016,** *32* (30), 7564-7571.
20. Dhar, P.; Kumar, A.; Katiyar, V., Magnetic Cellulose Nanocrystal Based Anisotropic Polylactic Acid Nanocomposite Films: Influence on Electrical, Magnetic, Thermal, and Mechanical Properties. *ACS Appl Mater Interfaces* **2016,** *8* (28), 18393-18409.
21. Gamelas, J. A.; Pedrosa, J.; Lourenco, A. F.; Mutje, P.; Gonzalez, I.; Chinga-Carrasco, G.; Singh, G.; Ferreira, P. J., On the morphology of cellulose nanofibrils obtained by TEMPO-mediated oxidation and mechanical treatment. *Micron* **2015,** *72*, 28-33.
22. Colson, J.; Bauer, W.; Mayr, M.; Fischer, W.; Gindl-Altmutter, W., Morphology and rheology of cellulose nanofibrils derived from mixtures of pulp fibres and papermaking fines. *Cellulose* **2016,** *23* (4), 2439-2448.
23. Foster, E. J.; Moon, R. J.; Agarwal, U.; Bortner, M. J.; Bras, J.; Camarero-Espinosa, S.; Chan, K. J.; Clift, M. J. D.; Cranston, E. D.; Eichorn, S.; Fox, D.; Hamad, W.; Heux, L.; Jean, B.; Korey, M.; Nieh, W.; Ong, K. J.; Reid, M. S.; Renneckar, S.; Roberts, R.; Shatkin, J. A.; Simonsen, J.; Stinson-Bagby, K.; Wanasekara, N.;

Youngblood, J., Current characterization methods for cellulose nanomaterials. *Chemical Society Reviews* **2018,** *47*, 2609-2679.
24. Xu, X.; Liu, F.; Jiang, L.; Zhu, J. Y.; Haagenson, D.; Wiesenborn, D. P., Cellulose nanocrystals vs. cellulose nanofibrils: a comparative study on their microstructures and effects as polymer reinforcing agents. *ACS Appl Mater Interfaces* **2013,** *5* (8), 2999-3009.
25. Isogai, A.; Saito, T.; Fukuzumi, H., TEMPO-oxidized cellulose nanofibers. *Nanoscale* **2011,** *3* (1), 71-85.
26. Okita, Y.; Saito, T.; Isogai, A., Entire surface oxidation of various cellulose microfibrils by TEMPO-mediated oxidation. *Biomacromolecules* **2010,** *11* (6), 1696-700.
27. Fukuzumi, H.; Saito, T.; Isogai, A., Influence of TEMPO-oxidized cellulose nanofibril length on film properties. *Carbohydr Polym* **2013,** *93* (1), 172-7.
28. Qing, Y.; Sabo, R.; Zhu, J. Y.; Agarwal, U.; Cai, Z.; Wu, Y., A comparative study of cellulose nanofibrils disintegrated via multiple processing approaches. *Carbohydr Polym* **2013,** *97* (1), 226-34.
29. Henriksson, M.; Berglund, L. A.; Isaksson, P.; Lindstrom, T.; Nishino, T., Cellulose nanopaper structures of high toughness. *Biomacromolecules* **2008,** *9* (6), 1579-85.
30. Hwang, I. G.; Kim, J. Y.; Weon, B. M., Droplet evaporation with complexity of evaporation modes. *Applied Physics Letters* **2017,** *110* (3).
31. Picknett, R. G.; Bexon, R., The evaporation of sessile or pendant drops in still air. *Journal of Colloid and Interface Science* **1977,** *61* (2), 336-350.
32. Erbil, H. Y.; McHale, G.; Newton, M. I., Drop Evaporation on Solid Surfaces: Constant Contact Angle Mode. *Langmuir* **2002,** *18* (7), 2636-2641.
33. Norris, D. J.; Arlinghaus, E. G.; Meng, L.; Heiny, R.; Scriven, L. E., Opaline Photonic Crystals: How Does Self-Assembly Work? *Advanced Materials* **2004,** *16* (16), 1393-1399.
34. Zhang, J.; Sun, Z.; Yang, B., Self-assembly of photonic crystals from polymer colloids. *Current Opinion in Colloid & Interface Science* **2009,** *14* (2), 103-114.
35. Choi, S.; Stassi, S.; Pisano, A. P.; Zohdi, T. I., Coffee-ring effect-based three dimensional patterning of micro/nanoparticle assembly with a single droplet. *Langmuir* **2010,** *26* (14), 11690-8.
36. Layani, M.; Gruchko, M.; Milo, O.; Balberg, I.; Azulay, D.; Magdassi, S., Transparent conductive coatings by printing coffee ring arrays obtained at room temperature. *ACS Nano* **2009,** *3* (11), 3537-42.
37. Bromberg, V.; Ma, S.; Singler, T. J., High-resolution inkjet printing of electrically conducting lines of silver nanoparticles by edge-enhanced twin-line deposition. *Applied Physics Letters* **2013,** *102* (21).
38. Zhang, Z.; Zhang, X.; Xin, Z.; Deng, M.; Wen, Y.; Song, Y., Controlled inkjetting of a conductive pattern of silver nanoparticles based on the coffee-ring effect. *Adv Mater* **2013,** *25* (46), 6714-8.
39. Zhang, Z.; Zhu, W., Controllable fabrication of a flexible transparent metallic grid conductor based on the coffee ring effect. *J. Mater. Chem. C* **2014,** *2* (45), 9587-9591.
40. Ma, S.; Liu, L.; Bromberg, V.; Singler, T. J., Fabrication of highly electrically conducting fine patterns via substrate-independent inkjet printing of mussel-inspired organic nano-material. *J. Mater. Chem. C* **2014,** *2* (20), 3885-3889.

41. Li, Y.; Lan, L.; Xiao, P.; Sun, S.; Lin, Z.; Song, W.; Song, E.; Gao, P.; Wu, W.; Peng, J., Coffee-Ring Defined Short Channels for Inkjet-Printed Metal Oxide Thin-Film Transistors. *ACS Appl Mater Interfaces* **2016,** *8* (30), 19643-8.
42. Dinh, N. T.; Sowade, E.; Blaudeck, T.; Hermann, S.; Rodriguez, R. D.; Zahn, D. R. T.; Schulz, S. E.; Baumann, R. R.; Kanoun, O., High-resolution inkjet printing of conductive carbon nanotube twin lines utilizing evaporation-driven self-assembly. *Carbon* **2016,** *96*, 382-393.
43. Deegan, R. D.; Bakajin, O.; Dupont, T. F.; Huber, G.; Nagel, S. R.; Witten, T. A., Contact line deposits in an evaporating drop. *Phys Rev E Stat Phys Plasmas Fluids Relat Interdiscip Topics* **2000,** *62* (1), 756-765.
44. Maillard, M.; Motte, L.; Pileni, M. P., Rings and Hexagons Made of Nanocrystals. *Advanced Materials* **2001,** *13* (3), 200-204.
45. Cachile, M.; Bénichou, O.; Poulard, C.; Cazabat, A. M., Evaporating Droplets. *Langmuir* **2002,** *18* (21), 8070-8078.
46. Hu, H.; Larson, R. G., Evaporation of a Sessile Droplet on a Substrate. *The Journal of Physical Chemistry B* **2002,** *106* (6), 1334-1344.
47. Mampallil, D.; Eral, H. B., A review on suppression and utilization of the coffee-ring effect. *Adv Colloid Interface Sci* **2018,** *252*, 38-54.
48. Frastia, L.; Archer, A. J.; Thiele, U., Dynamical model for the formation of patterned deposits at receding contact lines. *Phys Rev Lett* **2011,** *106* (7), 077801.
49. Freed-Brown, J., Evaporative deposition in receding drops. *Soft Matter* **2014,** *10* (47), 9506-10.
50. Langmuir, I., The Evaporation of Small Spheres. *Physical Review* **1918,** *12* (5), 368-370.
51. Birdi, K. S.; Vu, D. T., Wettability and the evaporation rates of fluids from solid surfaces. *Journal of Adhesion Science and Technology* **1993,** *7* (6), 485-493.
52. Birdi, K. S.; Vu, D. T.; Winter, A., A study of the evaporation rates of small water drops placed on a solid surface. *The Journal of Physical Chemistry* **1989,** *93* (9), 3702-3703.
53. Kulinich, S. A.; Farzaneh, M., Effect of contact angle hysteresis on water droplet evaporation from super-hydrophobic surfaces. *Applied Surface Science* **2009,** *255* (7), 4056-4060.
54. Rowan, S. M.; Newton, M. I.; McHale, G., Evaporation of Microdroplets and the Wetting of Solid Surfaces. *The Journal of Physical Chemistry* **1995,** *99* (35), 13268-13271.
55. McHale, G.; Rowan, S. M.; Newton, M. I.; Banerjee, M. K., Evaporation and the Wetting of a Low-Energy Solid Surface. *The Journal of Physical Chemistry B* **1998,** *102* (11), 1964-1967.
56. Gao, L.; McCarthy, T. J., Contact angle hysteresis explained. *Langmuir* **2006,** *22* (14), 6234-7.
57. Man, X.; Doi, M., Ring to Mountain Transition in Deposition Pattern of Drying Droplets. *Phys Rev Lett* **2016,** *116* (6), 066101.
58. Eral, H. B.; 't Mannetje, D. J. C. M.; Oh, J. M., Contact angle hysteresis: a review of fundamentals and applications. *Colloid and Polymer Science* **2012,** *291* (2), 247-260.
59. Ko, H.-Y.; Park, J.; Shin, H.; Moon, J., Rapid Self-Assembly of Monodisperse Colloidal Spheres in an Ink-Jet Printed Droplet. *Chemistry of Materials* **2004,** *16* (22), 4212-4215.
60. Tian, D.; Song, Y.; Jiang, L., Patterning of controllable surface wettability for printing techniques. *Chem Soc Rev* **2013,** *42* (12), 5184-209.

61. Cassie, A. B. D.; Baxter, S., Wettability of porous surfaces. *Transactions of the Faraday Society* **1944,** *40*.
62. Wenzel, R. N., Resistance of Solid Surfaces to Wetting by Water. *Industrial & Engineering Chemistry* **1936,** *28* (8), 988-994.
63. Semprebon, C.; Forsberg, P.; Priest, C.; Brinkmann, M., Pinning and wicking in regular pillar arrays. *Soft Matter* **2014,** *10* (31), 5739-48.
64. Dicuangco, M.; Dash, S.; Weibel, J. A.; Garimella, S. V., Effect of superhydrophobic surface morphology on evaporative deposition patterns. *Applied Physics Letters* **2014,** *104* (20).
65. Dai, X.; Stogin, B. B.; Yang, S.; Wong, T. S., Slippery Wenzel State. *ACS Nano* **2015,** *9* (9), 9260-7.
66. Cui, L.; Zhang, J.; Zhang, X.; Li, Y.; Wang, Z.; Gao, H.; Wang, T.; Zhu, S.; Yu, H.; Yang, B., Avoiding coffee ring structure based on hydrophobic silicon pillar arrays during single-drop evaporation. *Soft Matter* **2012,** *8* (40).
67. Lippmann, P. M. G., Relations in Electric Phenomonon and Capillaries. *Annales de Chimie et de physique* **1875,** *5*, 494-549.
68. Mugele, F.; Baret, J.-C., Electrowetting: from basics to applications. *Journal of Physics: Condensed Matter* **2005,** *17* (28), R705-R774.
69. Orejon, D.; Sefiane, K.; Shanahan, M. E., Evaporation of nanofluid droplets with applied DC potential. *J Colloid Interface Sci* **2013,** *407*, 29-38.
70. Li, F.; Mugele, F., How to make sticky surfaces slippery: Contact angle hysteresis in electrowetting with alternating voltage. *Applied Physics Letters* **2008,** *92* (24).
71. Wray, A. W.; Papageorgiou, D. T.; Craster, R. V.; Sefiane, K.; Matar, O. K., Electrostatic suppression of the "coffee stain effect". *Langmuir* **2014,** *30* (20), 5849-58.
72. Mampallil, D.; Eral, H. B.; van den Ende, D.; Mugele, F., Control of evaporating complex fluids through electrowetting. *Soft Matter* **2012,** *8* (41).
73. Zhang, J.; Borg, M. K.; Ritos, K.; Reese, J. M., Electrowetting Controls the Deposit Patterns of Evaporated Salt Water Nanodroplets. *Langmuir* **2016,** *32* (6), 1542-9.
74. Eral, H. B.; Augustine, D. M.; Duits, M. H. G.; Mugele, F., Suppressing the coffee stain effect: how to control colloidal self-assembly in evaporating drops using electrowetting. *Soft Matter* **2011,** *7* (10).
75. Gencer, A.; Van Rie, J.; Lombardo, S.; Kang, K.; Thielemans, W., Effect of Gelation on the Colloidal Deposition of Cellulose Nanocrystal Films. *Biomacromolecules* **2018,** *19* (8), 3233-3243.
76. Kim, S. J.; Kang, K. H.; Lee, J. G.; Kang, I. S.; Yoon, B. J., Control of particle-deposition pattern in a sessile droplet by using radial electroosmotic flow. *Anal Chem* **2006,** *78* (14), 5192-7.
77. Berg, J. C., *An Introduction to Interfaces and Colloids The Bridge to Nanoscience*. World Scientific Publishing Co. Pte. Ltd.: 2010; p 785.
78. Xu, X.; Luo, J., Marangoni flow in an evaporating water droplet. *Applied Physics Letters* **2007,** *91* (12).
79. Hu, H.; Larson, R. G., Analysis of the effects of Marangoni stresses on the microflow in an evaporating sessile droplet. *Langmuir* **2005,** *21* (9), 3972-80.
80. David, S.; Sefiane, K.; Tadrist, L., Experimental investigation of the effect of thermal properties of the substrate in the wetting and evaporation of sessile drops. *Colloids and Surfaces A: Physicochemical and Engineering Aspects* **2007,** *298* (1-2), 108-114.

81. Dunn, G. J.; Wilson, S. K.; Duffy, B. R.; David, S.; Sefiane, K., A mathematical model for the evaporation of a thin sessile liquid droplet: Comparison between experiment and theory. *Colloids and Surfaces A: Physicochemical and Engineering Aspects* **2008,** *323* (1-3), 50-55.
82. Ristenpart, W. D.; Kim, P. G.; Domingues, C.; Wan, J.; Stone, H. A., Influence of substrate conductivity on circulation reversal in evaporating drops. *Phys Rev Lett* **2007,** *99* (23), 234502.
83. Xu, X.; Luo, J.; Guo, D., Criterion for reversal of thermal Marangoni flow in drying drops. *Langmuir* **2010,** *26* (3), 1918-22.
84. Hu, H.; Larson, R. G., Analysis of the microfluid flow in an evaporating sessile droplet. *Langmuir* **2005,** *21* (9), 3963-71.
85. Wang, L.; Harris, M. T., Stagnation Point of Surface Flow during Drop Evaporation. *Langmuir* **2018,** *34* (20), 5918-5925.
86. Wang, J.; Evans, J. R., Segregation in multicomponent ceramic colloids during drying of droplets. *Phys Rev E Stat Nonlin Soft Matter Phys* **2006,** *73* (2 Pt 1), 021501.
87. Park, J.; Moon, J., Control of colloidal particle deposit patterns within picoliter droplets ejected by ink-jet printing. *Langmuir* **2006,** *22* (8), 3506-13.
88. Li, Y.; Lv, C.; Li, Z.; Quere, D.; Zheng, Q., From coffee rings to coffee eyes. *Soft Matter* **2015,** *11* (23), 4669-73.
89. Parsa, M.; Harmand, S.; Sefiane, K.; Bigerelle, M.; Deltombe, R., Effect of substrate temperature on pattern formation of nanoparticles from volatile drops. *Langmuir* **2015,** *31* (11), 3354-67.
90. Ta, V. D.; Carter, R. M.; Esenturk, E.; Connaughton, C.; Wasley, T. J.; Li, J.; Kay, R. W.; Stringer, J.; Smith, P. J.; Shephard, J. D., Dynamically controlled deposition of colloidal nanoparticle suspension in evaporating drops using laser radiation. *Soft Matter* **2016,** *12* (20), 4530-6.
91. Hu, H.; Larson, R. G., Marangoni effect reverses coffee-ring depositions. *J Phys Chem B* **2006,** *110* (14), 7090-7094.
92. Larson, R. G., Re-shaping the coffee ring. *Angew Chem Int Ed Engl* **2012,** *51* (11), 2546-8.
93. Singh, A.; Gunning, R. D.; Ahmed, S.; Barrett, C. A.; English, N. J.; Garate, J.-A.; Ryan, K. M., Controlled semiconductor nanorodassembly from solution: influence of concentration, charge and solvent nature. *J. Mater. Chem.* **2012,** *22* (4), 1562-1569.
94. Still, T.; Yunker, P. J.; Yodh, A. G., Surfactant-induced Marangoni eddies alter the coffee-rings of evaporating colloidal drops. *Langmuir* **2012,** *28* (11), 4984-8.
95. Larson, R. G., Transport and deposition patterns in drying sessile droplets. *AIChE Journal* **2014,** *60* (5), 1538-1571.
96. Anyfantakis, M.; Geng, Z.; Morel, M.; Rudiuk, S.; Baigl, D., Modulation of the coffee-ring effect in particle/surfactant mixtures: the importance of particle-interface interactions. *Langmuir* **2015,** *31* (14), 4113-20.
97. Erbil, H. Y., Control of stain geometry by drop evaporation of surfactant containing dispersions. *Adv Colloid Interface Sci* **2015,** *222*, 275-90.
98. Li, P.; Li, Y.; Zhou, Z. K.; Tang, S.; Yu, X. F.; Xiao, S.; Wu, Z.; Xiao, Q.; Zhao, Y.; Wang, H.; Chu, P. K., Evaporative Self-Assembly of Gold Nanorods into Macroscopic 3D Plasmonic Superlattice Arrays. *Adv Mater* **2016,** *28* (13), 2511-7.

99. de Gans, B. J.; Schubert, U. S., Inkjet printing of well-defined polymer dots and arrays. *Langmuir* **2004,** *20* (18), 7789-93.
100. Lim, J. A.; Lee, W. H.; Lee, H. S.; Lee, J. H.; Park, Y. D.; Cho, K., Self-Organization of Ink-jet-Printed Triisopropylsilylethynyl Pentacene via Evaporation-Induced Flows in a Drying Droplet. *Advanced Functional Materials* **2008,** *18* (2), 229-234.
101. Jin, H.; Qian, J.; Zhou, L.; Yuan, J.; Huang, H.; Wang, Y.; Tang, W. M.; Chan, H. L., Suppressing the Coffee-Ring Effect in Semitransparent MnO2 Film for a High-Performance Solar-Powered Energy Storage Window. *ACS Appl Mater Interfaces* **2016,** *8* (14), 9088-96.
102. Stamou, D.; Duschl, C.; Johannsmann, D., Long-range attraction between colloidal spheres at the air-water interface: the consequence of an irregular meniscus. *Phys Rev E Stat Phys Plasmas Fluids Relat Interdiscip Topics* **2000,** *62* (4 Pt B), 5263-72.
103. Yunker, P. J.; Still, T.; Lohr, M. A.; Yodh, A. G., Suppression of the coffee-ring effect by shape-dependent capillary interactions. *Nature* **2011,** *476* (7360), 308-11.
104. Dasgupta, S.; Katava, M.; Faraj, M.; Auth, T.; Gompper, G., Capillary assembly of microscale ellipsoidal, cuboidal, and spherical particles at interfaces. *Langmuir* **2014,** *30* (40), 11873-82.
105. Crivoi, A.; Duan, F., Amplifying and attenuating the coffee-ring effect in drying sessile nanofluid droplets. *Phys Rev E Stat Nonlin Soft Matter Phys* **2013,** *87* (4), 042303.
106. Crivoi, A.; Duan, F., Elimination of the coffee-ring effect by promoting particle adsorption and long-range interaction. *Langmuir* **2013,** *29* (39), 12067-74.
107. Crivoi, A.; Zhong, X.; Duan, F., Crossover from the coffee-ring effect to the uniform deposit caused by irreversible cluster-cluster aggregation. *Phys Rev E Stat Nonlin Soft Matter Phys* **2015,** *92* (3), 032302.
108. Li, Y.; Yang, Q.; Li, M.; Song, Y., Rate-dependent interface capture beyond the coffee-ring effect. *Sci Rep* **2016,** *6*, 24628.
109. Erbil, H. Y., Evaporation of pure liquid sessile and spherical suspended drops: a review. *Adv Colloid Interface Sci* **2012,** *170* (1-2), 67-86.
110. Brutin, D.; Starov, V., Recent advances in droplet wetting and evaporation. *Chem Soc Rev* **2018,** *47* (2), 558-585.
111. Mansfield, M. L.; Douglas, J. F., Transport Properties of Rodlike Particles. *Macromolecules* **2008,** *41* (14), 5422-5432.
112. Derjaguin, B.; Landau, L., Theory of the stability of strongly charged lyophobic sols and of the adhesion of strongly charged particles in solutions of electrolytes. *Progress in Surface Science* **1993,** *43* (1-4), 30-59.
113. E. J. W. Verwey, J. T. O., *Theory of the Stability of Lyophobic Colloids*. Dover Publications: 1949.
114. M. Doi, S. F. E., *The Theory of Polymer Dynamics*. Clarendon Press: Oxford: 1988.
115. Onsager, L., The Effects of Shape on the Interaction of Colloidal Particles. *Annals of the New York Academy of Sciences* **1949,** *51* (4), 627-659.
116. Xu, G.; Hong, W.; Sun, W.; Wang, T.; Tong, Z., Effect of Salt Concentration on the Motion of Particles near the Substrate in Drying Sessile Colloidal Droplets. *Langmuir* **2017,** *33* (3), 685-695.
117. Bhardwaj, R.; Fang, X.; Somasundaran, P.; Attinger, D., Self-assembly of colloidal particles from evaporating droplets: role of DLVO interactions and proposition of a phase diagram. *Langmuir* **2010,** *26* (11), 7833-42.

118. Crank, J., *The Mathematics of Diffusion*. Oxford Uniiversity Press: 1979.
119. Carter, H. G.; Kibler, K. G., Langmuir-Type Model for Anomalous Moisture Diffusion In Composite Resins. *Journal of Composite Materials* **2016,** *12* (2), 118-131.
120. Boukhoulda, F. B.; Guillaumat, L.; Lataillade, J. L.; Adda-Bedia, E.; Lousdad, A., Aging-impact coupling based analysis upon glass/polyester composite material in hygrothermal environment. *Materials & Design* **2011,** *32* (7), 4080-4087.
121. Joliff, Y.; Belec, L.; Chailan, J. F., Modified water diffusion kinetics in an unidirectional glass/fibre composite due to the interphase area: Experimental, analytical and numerical approach. *Composite Structures* **2013,** *97*, 296-303.
122. Sridhar, R.; Narasimha Murthy, H. N.; Karthik, B.; Vishnu Mahesh, K. R.; Krishna, M.; Ratna, P., Moisture diffusion through nanoclay/vinylester processed using twin-screw extrusion. *Journal of Vinyl and Additive Technology* **2014,** *20* (3), 152-159.
123. Guloglu, G. E. Moisture absorption of thermosetting polymers and nanocomposites. University of Oklahoma, Norman, Oklahoma, 2018.
124. Liu, F.; Urban, M. W., Recent advances and challenges in designing stimuli-responsive polymers. *Progress in Polymer Science* **2010,** *35* (1-2), 3-23.
125. Cui, H.; Zhao, Q.; Wang, Y.; Du, X., Bioinspired Actuators Based on Stimuli-Responsive Polymers. *Chem Asian J* **2019,** *14* (14), 2369-2387.
126. Sun, H.; Kabb, C. P.; Sims, M. B.; Sumerlin, B. S., Architecture-transformable polymers: Reshaping the future of stimuli-responsive polymers. *Progress in Polymer Science* **2019,** *89*, 61-75.
127. Mu, T.; Liu, L.; Lan, X.; Liu, Y.; Leng, J., Shape memory polymers for composites. *Composites Science and Technology* **2018,** *160*, 169-198.
128. Favier, V.; Chanzy, H.; Cavaille, J. Y., Polymer Nanocomposites Reinforced by Cellulose Whiskers. *Macromolecules* **1995,** *28* (18), 6365-6367.
129. Mounika, M.; Ravindra, K., Characterization of Nanocomposites Reinforced with Cellulose Whiskers: A Review. *Materials Today: Proceedings* **2015,** *2* (4-5), 3610-3618.
130. Qiu, X.; Hu, S., "Smart" Materials Based on Cellulose: A Review of the Preparations, Properties, and Applications. *Materials (Basel)* **2013,** *6* (3), 738-781.
131. Auad, M. L.; Contos, V. S.; Nutt, S.; Aranguren, M. I.; Marcovich, N. E., Characterization of nanocellulose- reinforced shape memory polyurethanes. *Polymer International* **2008,** *57* (4), 651-659.
132. Capadona, J. R.; Shanmuganathan, K.; Tyler, D. J.; Rowan, S. J.; Weder, C., Stimuli-responsive polymer nanocomposites inspired by the sea cucumber dermis. *Science* **2008,** *319* (5868), 1370-4.
133. Rusli, R.; Shanmuganathan, K.; Rowan, S. J.; Weder, C.; Eichhorn, S. J., Stress-transfer in anisotropic and environmentally adaptive cellulose whisker nanocomposites. *Biomacromolecules* **2010,** *11* (3), 762-8.
134. Shanmuganathan, K.; Capadona, J. R.; Rowan, S. J.; Weder, C., Stimuli-responsive mechanically adaptive polymer nanocomposites. *ACS Appl Mater Interfaces* **2010,** *2* (1), 165-74.
135. Dagnon, K. L.; Shanmuganathan, K.; Weder, C.; Rowan, S. J., Water-Triggered Modulus Changes of Cellulose Nanofiber Nanocomposites with Hydrophobic Polymer Matrices. *Macromolecules* **2012,** *45* (11), 4707-4715.

136. Dagnon, K. L.; Way, A. E.; Carson, S. O.; Silva, J.; Maia, J.; Rowan, S. J., Controlling the Rate of Water-Induced Switching in Mechanically Dynamic Cellulose Nanocrystal Composites. *Macromolecules* **2013,** *46* (20), 8203-8212.
137. Annamalai, P. K.; Dagnon, K. L.; Monemian, S.; Foster, E. J.; Rowan, S. J.; Weder, C., Water-responsive mechanically adaptive nanocomposites based on styrene-butadiene rubber and cellulose nanocrystals--processing matters. *ACS Appl Mater Interfaces* **2014,** *6* (2), 967-76.
138. Chen, Y.; Li, G.; Yin, Q.; Jia, H.; Ji, Q.; Wang, L.; Wang, D.; Yin, B., Stimuli-responsive polymer nanocomposites based on styrene-butadiene rubber and bacterial cellulose whiskers. *Polymers for Advanced Technologies* **2018,** *29* (5), 1507-1517.
139. Tian, M.; Zhen, X.; Wang, Z.; Zou, H.; Zhang, L.; Ning, N., Bioderived Rubber-Cellulose Nanocrystal Composites with Tunable Water-Responsive Adaptive Mechanical Behavior. *ACS Appl Mater Interfaces* **2017,** *9* (7), 6482-6487.
140. Fallon, J. J.; Kolb, B. Q.; Herwig, C. J.; Foster, E. J.; Bortner, M. J., Mechanically adaptive thermoplastic polyurethane/cellulose nanocrystal composites: Process-driven structure-property relationships. *Journal of Applied Polymer Science* **2019,** *136* (4).
141. Urbina, L.; Alonso-Varona, A.; Saralegi, A.; Palomares, T.; Eceiza, A.; Corcuera, M. A.; Retegi, A., Hybrid and biocompatible cellulose/polyurethane nanocomposites with water-activated shape memory properties. *Carbohydr Polym* **2019,** *216*, 86-96.
142. van den Berg, O.; Capadona, J. R.; Weder, C., Preparation of homogeneous dispersions of tunicate cellulose whiskers in organic solvents. *Biomacromolecules* **2007,** *8* (4), 1353-7.
143. Halpin, J. C.; Kardos, J. L., Moduli of Crystalline Polymers Employing Composite Theory. *Journal of Applied Physics* **1972,** *43* (5), 2235-2241.
144. Azizi Samir, M. A.; Alloin, F.; Dufresne, A., Review of recent research into cellulosic whiskers, their properties and their application in nanocomposite field. *Biomacromolecules* **2005,** *6* (2), 612-26.
145. Hammersley, J. M., Percolation processes. *Mathematical Proceedings of the Cambridge Philosophical Society* **2008,** *53* (3), 642-645.
146. Bréchet, Y.; Cavaillé, J. Y.; Chabert, E.; Chazeau, L.; Dendievel, R.; Flandin, L.; Gauthier, C., Polymer Based Nanocomposites: Effect of Filler-Filler and Filler-Matrix Interactions. *Advanced Engineering Materials* **2001,** *3* (8).

Chapter 3 - Multi-axis Alignment of Rod-like Cellulose Nanocrystals in Drying Droplets

Cailean Q. Pritchard[a], Fernando Navarro[b], Maren Roman[b,c,], and Michael J. Bortner[a,b,]**

*Corresponding authors

This chapter was published in Journal of Colloid and Interface Science, Pritchard, C.Q., et al., *Multi-axis alignment of Rod-like cellulose nanocrystals in drying droplets.* J Colloid Interface Sci, 2021. **603**: p. 450-458. https://doi.org/10.1016/j.jcis.2021.06.069.

The following contributions were made by other authors: the experiments and characterizations exhibited in Figure 3-1 and Figure 3-2 were conducted by Fernando Navarro.

The following people contributed to the writing of this chapter: Cailean Q. Pritchard (Original Draft), Maren Roman (Review and Editing), and Michael J. Bortner (Review and Editing)

3.1 Abstract

The dynamic local order in aqueous suspensions of cellulose nanocrystals (CNCs) in evaporating sessile droplets was investigated through time-resolved polarized light microscopy. Alignment of CNCs was explored as a function of nanoparticle concentration and droplet volume. Complex boundary interactions that depend strongly on the local particle concentration in the vicinity of the contact line were found to govern the ultimate alignment. Computational analysis of the rotational Péclet number further revealed that CNC alignment is independent of evaporation-induced shear flow during migration to the contact line. This was experimentally verified during the evaporation of pre-ordered CNC suspensions where particle orientation was not observed to be coupled to their entrainment. Finally, multiple modes of orientation were identified suggesting local control over CNC properties can be attained via droplet-based patterning methods.

3.2 Introduction

Droplets of colloidal suspensions that dry on non-absorbing, solid surfaces are ubiquitous phenomena. Coffee stains on table surfaces and water stains on kitchen and bathroom fixtures are two familiar examples of the ensuing particle deposits. Accordingly, evaporating sessile droplets commonly exhibit radial flow within the droplet while drying which carry suspended particles to the edge of the droplet.[1-3] Numerous investigations have sought to prevent the formation of these toroidal deposits, or "coffee-rings", in the pursuit of producing uniform films. These studies modify the solvent evaporation rate[4], induce Marangoni convection,[5, 6] suppress flow through gelation,[7, 8] or control the substrate's surface energy[2, 3] to suppress outward capillary flow. While these technologies are interesting, there has been minimal exploration of the benefits of non-uniform directed deposition methods, especially involving anisotropic nanomaterials. Anti-counterfeit coatings and patterning of nanoscale structures are excellent

examples of technologies that rely on spatially non-uniform directed deposition methods and can exploit the complex fluid dynamic profiles developed in drying droplets.[9-12]

Such technologies can further be developed through the use of optically and mechanically anisotropic materials such as cellulose nanocrystals (CNCs) which are rod-shaped nanoparticles that tend to organize into ordered liquid crystalline phases.[13-16] In these materials, the cellulose backbone is oriented parallel to the long-axis of the rod leading to birefringence and anisotropic mechanical properties.[17] Control over CNC orientation drives their performance as photonic crystals or smart nanomaterials, which is governed by the complex relationship between fluid transport, contact line dynamics, and interparticle interactions. To this end, evaporation-induced alignment is presented as a low energy alternative to orient CNCs and other rod shaped particles compared to conventional methods that apply magnetic,[18-20] shear forces,[21-23] electrospraying,[24] or gas flow induced alignment.[25] Mashkour et al. recently demonstrated excellent control over patterned structures of CNCs using contact line motion in evaporating CNC suspensions to impart alignment through a surface tension torque.[12, 26] Our work supports Mashkour's invocation of the surface tension torque's role in evaporation-based particle orientation and provides further insight into alternative orientation states that can be achieved through similar methods.

Here, we investigate the relative impact of flow-induced orientation compared to orientation governed by interparticle interactions and contact line motion. Computational fluid dynamic simulations were performed to analyze the rotational Péclet number which expresses the relative contribution of Brownian motion and shear forces on suspended particle alignment. Further, we identified conditions leading to the development of tangential and radial alignment through time-resolved polarized light microscopy (PLM). Additionally, an intermediate

orientation phase in evaporating droplet suspensions of CNCs was discovered, suggesting complex boundary interactions that depend strongly on the local particle concentration. Finally, the insight gained here can guide strategies to obtain tunable particle orientation patterns.

3.3 Materials and Methods

3.3.1 Cellulose nanocrystal preparation for atomic force microscopy.

CNCs were prepared from dissolving-grade softwood sulfite pulp (Temalfa 93A-A), kindly provided by Tembec, Inc. Lapsheets of the pulp were cut into pieces of approximately 1 cm × 1 cm and milled in a Wiley mill (Thomas Wiley Mini-Mill) to pass through 60-mesh screen. The milled pulp was hydrolyzed under stirring with 60 wt % sulfuric acid (10 mL/g cellulose) at 50 °C for 60 min. The hydrolysis was quenched by diluting the reaction mixture 10-fold with deionized water (Millipore Direct-Q 5, 18.2 MΩ·cm). The nanocrystals were collected by centrifugation at 4550 × g (Thermo IEC Centra-GP8R) for 10 min at 25 °C and washed once with deionized water. The CNCs were then dialyzed (Spectra/Por 4 dialysis tubing) against deionized water until the pH of fresh dialysis medium stayed constant over time. The nanocrystal suspension was sonicated (Sonics & Materials Model VC-505) for 10 min at 200 W under ice-bath cooling and filtered through a 0.45 µm polyvinylidene fluoride syringe filter (GD/XP, Whatman) to remove aggregates.

3.3.2 Cellulose nanocrystal preparation for polarized light microscopy

CNCs were purchased from The University of Maine Process Development Center (Lot # 2018-FPL-CNC-126) as a concentrated gel, 10.3 wt % solids and 1.1 wt % Sulfur on dry CNC Sodium form. CNCs were diluted to 0.1 – 3.9 wt % with deionized water and stirred at 600 rpm

for 30 min followed by an additional 30 min bath sonication (Branson 5800 using the high power setting). Prior to droplet casting, CNC suspensions were bath sonicated for 10 min.

3.3.3 Cleaning of Glass Substrates and Sample Preparation

A mixture of 75 % v/v hydrochloric acid (NF/FCC, Fisher chemical, 36.5-38%) and 25% v/v nitric acid (NF, Fisher Chemical, 69-70%) was prepared as described previously.[27] The solution was degassed in an ultrasonic bath (Branson 3510 Ultrasonic Cleaner) for 30 min at 45°C. Glass microscope slides, measuring 76.2 mm × 25.4 mm, (PEARL, MingZhu Industries) were then submerged into the cleaning solution and subjected to bath sonication for 10 min at 45°C. The treatment was followed by an additional ultrasonic treatment and rinsing with deionized water. Finally, the cleaned glass slides were dried under nitrogen flow and cut with a diamond-tipped glass cutter into 38.1 mm × 25.4 mm pieces. Alconox-cleaned slides were prepared following the above procedure, with a 1 wt % aqueous solution of Alconox instead of aqua regia. Rain-X cleaned slides were prepared following the manufacturer's instructions. Accordingly, slides were rinsed in DI water and subsequently wiped with Kim wipe until dry, Rain-X was sprayed on another Kim wipe and was used to thoroughly wipe the surface of the glass slide. Finally, the slides were dried once more with a Kim wipe before testing.

Droplets, 0.25 or 0.5 µL, of aqueous CNC suspensions ranging in concentration from 0.1 – 3.9 wt % were subsequently placed on cleaned glass slides loaded on the PLM or in a 50 mm polystyrene Petri dish for AFM samples. The Petri dishes were covered with polystyrene lids that were perforated in the center with a hole of approximately 1 mm in diameter, and the droplets was allowed to dry overnight.

3.3.4 Polarized light microscopy

Polarized light microscopy (PLM) experiments employed a Zeiss Axioskop 40 A POL, equipped with a 530 nm first-order retardation plate. The polarizer and analyzer were oriented in east–west and north–south direction, respectively. The first-order retardation plate was inserted so that its slow axis was oriented northeast–southwest and its fast axis northwest–southeast. Images were recorded with a Canon EOS 20D digital single-lens reflex camera (8.2 megapixels) mounted onto the microscope. Time-resolved PLM videos were recorded with an Omax A3518003 digital reflex camera (18 megapixels) with a 0.5x microscope adapter for mounting. Videos, 4x magnification, were initiated immediately before droplets were pipetted on cleaned glass slides. Once placed, the microscope stage was slightly repositioned to ensure capture of the droplets. Recording was manually terminated after evaporation was complete.

3.3.5 Atomic Force Microscopy

Atomic force microscopy (AFM) was performed with an Asylum Research MFP 3D mounted onto an Olympus IX 71 inverted fluorescence microscope. For images of CNCs, 100 µL of a 0.001 wt % aqueous suspension of CNCs was spin coated (3000 rpm, 1 min) onto an aqua regia-cleaned glass slide. The sample was scanned in intermittent contact mode in air, using Nanoworld SSS-NCH SuperSharp Silicon probes (nominal tip radius: 2 nm). Dried droplets were scanned in intermittent contact mode in air, using Olympus OMCL-AC160TS probes (nominal tip radius: <10 nm).

3.3.6 Finite Element Analysis

A 2.0 µL, sessile, single-phase water droplet was modeled with the finite element method in COMSOL Multiphysics®. The system was allowed to evaporate in air at 23.5 °C following Fick's second law of diffusion in three dimensions. Fluid and heat transport were accounted for utilizing Cauchy's momentum equation and the equation of energy derived from first principles.

A deforming mesh captured the change in volume with time in correspondence with the prescribed evaporation rate. To relate the pure fluid to the suspended media, a concentration-dependent viscosity correlation, given by Li et al., was implemented for CNCs to treat the fluid as a continuum.[28] Detailed discussion of the underlying equations of the model is available in the Supporting Information (SI). The rotational Péclet numbers were calculated from the shear rate the likelihood of flow-induced particle orientation.

The simulations were performed using a cluster of Intel® Xeon® 2× E5-2680v3 @ 2.5 GHz CPUs with 192 cores and 128GB RAM @ 2133 MHz and were completed in 1030 CPU hours (Advanced Research Computing, Blacksburg, VA).

3.4 Results and Discussion

To establish a reference for evaporation of droplets of CNC suspensions, sessile droplets of a 0.76 wt % aqueous suspension of CNCs were evaporated in air after inkjet printing onto an untreated glass slide. We achieved coffee-ring deposition near the periphery of the droplet which is common for droplets colloidal suspensions having a pinned contact line.[2, 3] The height profile of these deposits was subsequently characterized by atomic force microscopy (AFM), Figure 3-1, to investigate the arrangement of CNCs. The coffee-rings were approximately 90 nm in height which is consistent with coffee-rings of CNCs reported in literature.[7, 27, 29] The coffee-rings were also shorter than the average length, 123 nm, of CNCs used in this work suggesting that some degree of anisotropy is developed in the particles comprising the coffee-ring.

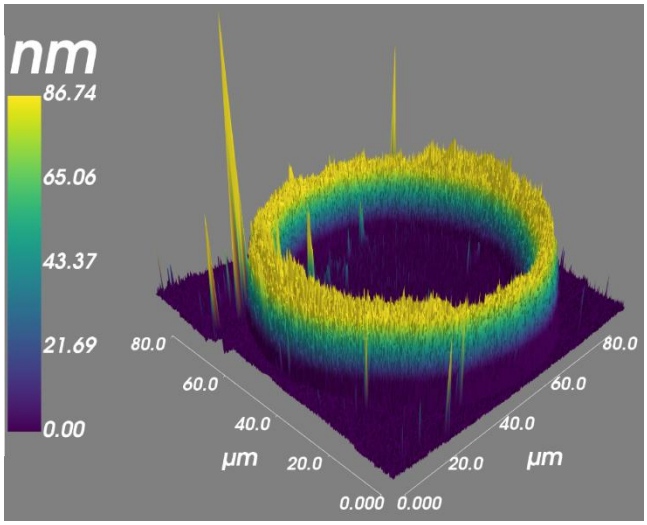

Figure 3-1. 3D AFM height profile of a deposited water droplet containing 0.76 wt % CNCs and resulting in a coffee-ring structure.

Polarized light microscopy (PLM) is widely used to characterize the self-assembly of CNCs into liquid crystalline phases[6-8, 22, 30] and therefore was implemented to characterize the particle orientation distribution post-evaporation. In addition to the suspected anisotropy within the coffee-ring, we previously investigated the influence of attractive electrostatic interactions between the positively charged substrate and negatively charged CNCs on the deposition of CNCs from droplet suspensions.[31] Deposition on aqua regia-cleaned glass, led to particle deposition in the center of the droplet in addition to the coffee-ring.[31] Here, 2 μL droplets of CNC suspensions were deposited with a micropipette onto aqua regia-cleaned glass slides to observe CNC orientation in the coffee-ring as well as throughout the remainder of the deposit. PLM revealed a Maltese cross-interference pattern, Figure 3-2a, indicating long range order and alignment of nanoparticles post-evaporation.[27, 29]

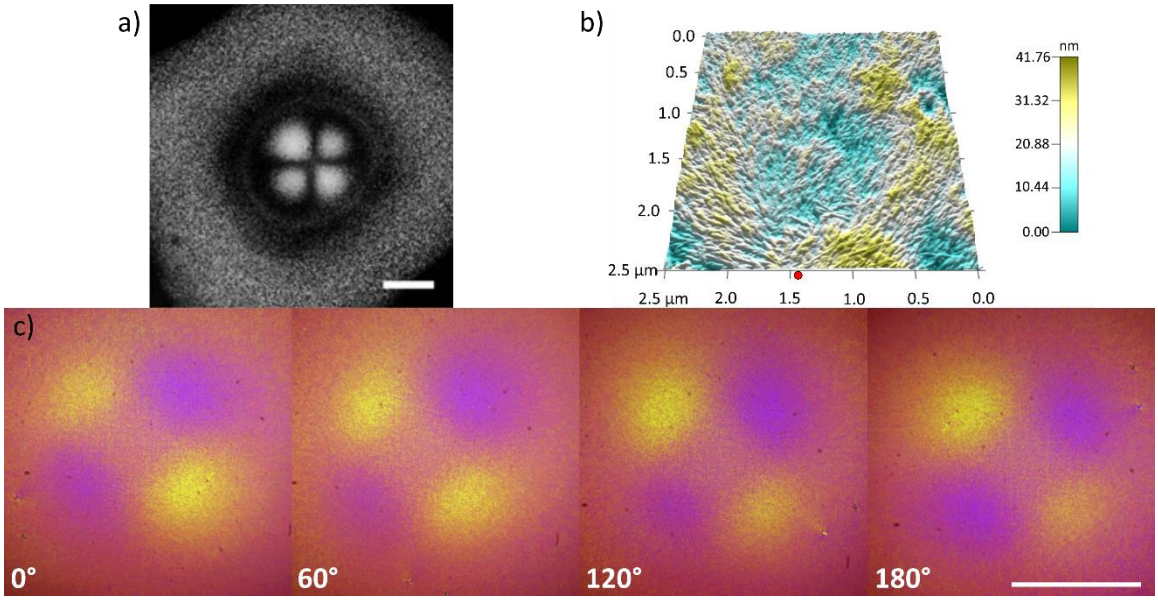

Figure 3-2. (a) Polarized-light micrographs of a 2 µL droplet of a CNC suspension exhibiting Maltese cross extinction patterns (scale bar = 500 µm). (b) AFM amplitude image of an area near the center of the droplet showing radial alignment of CNCs (scan size: 2.5 µm). The red dot on the lower horizontal axis indicates the direction of the approximate center of the CNC droplet. (c) Polarized optical micrographs of a 2 µL droplet of a CNC suspension with a first-order full-wave retardation plate illustrating radially aligned CNCs independent of sample rotation (scale bar = 500 µm).

In Figure 3-2b, AFM was performed on a smaller, 2.5 x 2.5 µm, targeted region near the center of the droplet to observe the particle orientation outside of the coffee-ring. The height profile in the central region is more uniform than within the coffee ring and as a result of the reduced particle count, CNCs were observed holding a radial orientation. Subsequently, a first order full-wave retardation plate, oriented with its slow axis in the northeast-southwest direction, was inserted to optically confirm the orientation observed via AFM. Accordingly CNCs observed herein, will show blue colors when their slow axis, corresponding to both the cellulose

chain direction and the long axis of the crystal,[17] aligns in the northeast-southwest direction.[30, 32, 33] Yellow colors indicate the slow axis of the CNCs are oriented northwest-southeast, parallel to the fast axis of the wave plate.[30, 32, 33] Symmetric radially oriented particles were observed in Figure 3-2c, as shown in PLM images of the samples after stage rotations of 0, 60, 120, and 180°. While others have reported tangential alignment of CNCs in evaporating droplets,[8] this is the first demonstration of radially aligned CNCs following evaporation-induced self-assembly indicating droplet-based deposition can provide tunable orientation of rod-shaped particles.

To investigate parameters governing the orientation of CNCs post-evaporation, the spatial alignment of CNCs from evaporated droplet suspensions was characterized as a function of initial CNC concentration and droplet volume. In Figure 3-3, 0.25 and 0.5 μL droplets of 0.1 – 3.9 wt % (0.07 – 2.7 vol %) CNC suspensions were deposited in triplicate via micropipette on Alconox-cleaned glass slides. Alconox was substituted as the cleaning agent to reduce the effect of electrostatic interactions from the substrate on the resulting particle depositions. The droplet radius, Figure 3-3b, was found to be independent of CNC concentration due to rapid contact line pinning after the initial spreading of the droplet during placement. Notably, outside of the 0.1 wt % CNC suspension, the width of coffee-rings was largely independent of CNC concentration. This suggests the droplet depins from the coffee-ring and may not maintain its pinned contact line throughout the entirety of evaporation. Likely, the 0.1 wt % CNC suspension deposited the large majority of is particles at the contact line before depinning resulting in negligible particle deposition within the droplet's center.

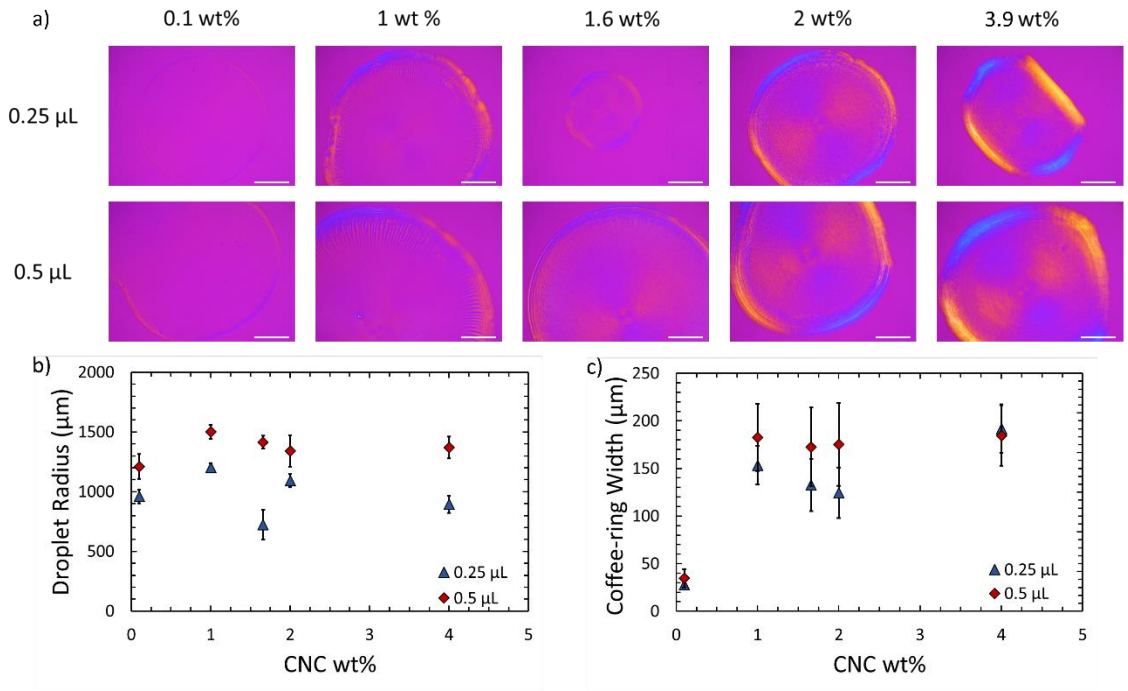

Figure 3-3. a) PLM of droplet suspensions of CNCs with initial concentrations ranging from 0.1 – 3.9 wt % with initial volumes of 0.25 µL (top) and 0.5 µL (bottom) viewed with a first order full wave retardation plate, scale bar = 500 µm, b) droplet radius, and c) coffee-ring width as a function of initial CNC concentration and volume.

Time-resolved PLM, supporting information: Droplet Evaporation Video 1, during evaporation confirms the maximal coffee-ring width as a result of the contact line depinning. Evaporation of droplets of CNCs suspensions on Alconox-cleaned glass thus proceed in a bimodal fashion. Initially, the contact line is pinned until remaining suspended particle concentration has dropped below a threshold to continue pinning the droplet.[34, 35] After depinning, the contact line recedes until evaporation is complete and the remaining suspended particles are deposited within the central region of the droplet.

Crucially, the switch to a dynamic contact line mid-evaporation leads to a change in the orientation of deposited CNCs within the center of the droplet as observed in snapshots of time-resolved PLM, supporting information: Droplet Evaporation Video 1 and Figure 3-4. Radially oriented CNCs near the contact line are initially observed, in Figure 3-4a, as a result of the droplet wetting the surface of the glass slide immediately following its placement. Droplets deposited on Alconox-cleaned glass typically develop a pinned contact line after placement and do not tend to wet in this manner which may have occurred as a result of chemical inhomogeneities on the glass surface after cleaning. Thus, an initial CNC orientation parallel to the contact line was detected in the majority of droplets deposited in this work.

After the formation of the coffee-ring, Figure 3-4b illustrates a change in CNC orientation after the onset of depinning is identified. Accordingly, CNCs can be seen ordering radially prior to deposition and near the receding contact line, highlighted by the shift in color patterns at the interior of the coffee ring and pointed out by blue and yellow arrows in Figure 3-4b. As the particles are driven to moving boundary, an intermediate phase develops with elevated viscosity due to the locally increased CNC concentration.[36] Further, the elevated concentration increases the relative strength of van der Waals and electrostatic forces between CNCs which contribute to their alignment.[15] This phenomenon illustrates the importance of local particle concentration on the evolution of the spatial distribution of particle arrangements. Ultimately once evaporation is complete, these CNCs arrange in coordination with their tangentially-oriented neighbors in Figure 3-4c. As the contact line depins, tangential orientation is observed until evaporation nears completion at the center of the droplet. Here, we observed deposition of radially aligned particles at the outer edge of the center that then tangentially align near the center at certain concentrations. In this central region, the radial particle alignment

developed near the dynamic contact line is maintained after evaporation completes. A distinct 90° rotation of CNCs deposited in the center of the droplet can be observed for initial concentrations greater than 1 wt % as evidenced by alternating blue and yellow colors progressing radially outward from the droplet center in Figure 3-4c. Finally, the centermost CNCs, illustrated in Figure 3-4d, reverted to a tangential alignment after deposition.

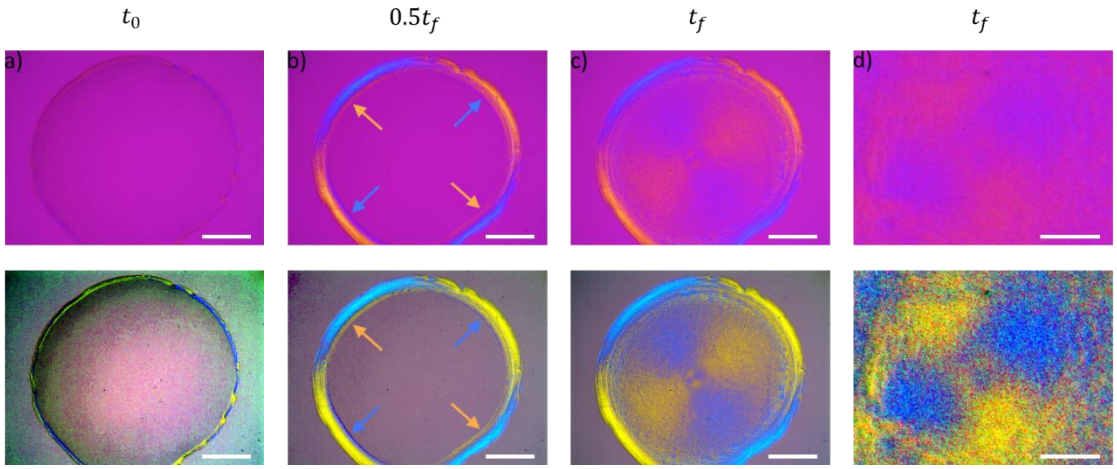

Figure 3-4. Snapshots of a 0.25 µL droplet of a 2 wt % CNC aqueous suspension evaporating on an Alconox-cleaned glass slide. Time points are observed after intial deposition, a) $t = 10$ s, halfway through evaporation b) $t = 82.5$ s where blue and yellow arrows highlight local changes in orientation, c) after evaporation completes, $t = 167$ s, and d) close up images of the center of the final deposits. The bottom images were enhanced to highlight the blue and yellow regions which are indicative of CNC alignment. a-c) Scale bar = 500 µm and d) 50 µm.

The spatial distribution of aligned CNCs after evaporation may depend on time-dependent variations in local CNC concentration as particles are removed from the suspension once deposited. The schematic in Figure 3-5 illustrates the evolution of CNC orientation as a function of time as observed via time-resolved PLM and is clearly highlighted in supporting

information: Droplet Evaporation Video 1. The surface tension torque,[12, 26] generated through the desire for CNCs to minimize the capillary energy,[37, 38] acting to rotate CNCs parallel to a static contact line is aided by the entrainment of new solids to the air-water interface. Additional particles are not only rotated through the effects of surface tension, but also through the hydrodynamic force generated from evaporation-induced radially outward flow[2, 3] acting on rod-shaped particles impinging against a fixed boundary. Together, these effects lead to the initial formation of a coffee-ring of tangentially-oriented CNCs, Figure 3-5a. Once the contact line begins to recede, Figure 3-5b, an end of a CNC affixed to the contact line could trail the inward motion of the contact line and align radially. Coupled with the inherent tendency of CNCs to align with their long axis parallel, with a slight twist,[33] to adjacent CNCs, a radial alignment in the vicinity of the dynamic contact line is achieved. Critically, at this stage, there is no longer a sufficient influx of additional CNCs to the boundary to create particle collisions that would otherwise rotate the CNCs parallel to the contact line. Once the contact line continues past the particles, the CNCs are able to relax into a more thermodynamically stable configuration[33] until the water between the CNCs evaporates sufficiently past the gel point. During this time, CNCs reorganize from a radial to tangential alignment. Next, near the center, Figure 3-5c, the remaining CNC concentration inside the droplet has continued to decrease. Once CNCs are deposited in this domain, they may no longer feel the effects of their neighbors and will instead maintain the alignment prescribed by the receding contact line. Finally, if CNCs remain suspended in the droplet, Figure 3-5d, the geometric constraints induced by the shrinking droplet begin to restrict the orientation once again to a tangential orientation.

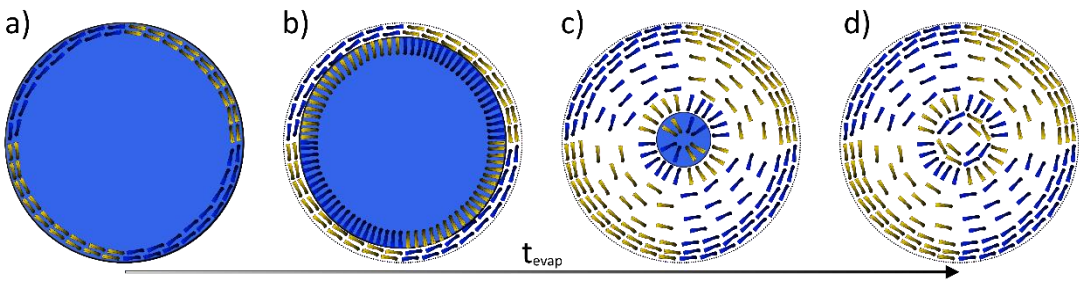

Figure 3-5. Schematic depicting the progression (a→d) of CNC alignment during evaporation. a) Tangentially aligned CNCs in the coffee-ring. b) Radially aligned CNCs during contact line motion. c) CNCs from the previous step reorganize to a tangential arrangement and radially aligned CNCs are deposited near the center. d) Evaporation is complete with tangentially aligned CNCs in the center of the deposit. Dashed lines indicate the initial contact line and the blue circle shows the progression of the current droplet shape.

Appreciating the desire to deposit CNCs in a preferential direction, it is important to understand whether hydrodynamic shear contributes to CNC orientation post-evaporation. One might suggest that shear forces acting on the nanoparticles during their entrainment to the boundary act to rotate CNCs in the flow direction, similar to many reported shear alignment techniques and given the apparent radial alignment observed near the air-water interface during contact line recession.[21, 39, 40] Thus, to investigate the development of nanoparticle alignment resulting in the final CNC orientation on the substrate, computational fluid dynamic analysis was performed to analyze the impact of droplet hydrodynamics on particle alignment in evaporating sessile droplets. The effects of surface tension and convection in both the droplet and surrounding medium were considered due to their substantial impact on flow behavior. Particle interactions were approximated through a concentration-dependent viscosity model, but the particles and their interactions were not explicitly and individually represented outside of a bulk

empirical viscosity model. Therefore, the proposed model may capture the effects of evaporation-induced convection, but not individual particle deposition events.

We focused our investigation on the impacts of hydrodynamic forces and Brownian motion on the alignment of nanoparticles in evaporation induced flows. A concentration-dependent viscosity model was implemented to decouple the multiple levels of interaction between continuum and particle dynamics. A fundamental representation of the viscosity for rigid rod-like particle suspensions could be implemented through the Krieger-Dougherty[41] or Doi-Edwards[42] models; however, these are not representative of concentrated suspensions $n > \frac{1}{dL^2}$ which are present at the late stages of the evaporation process where particle-particle interactions become dominant. Therefore, the empirical relationship proposed by Li et al. for particle concentrations from 0.25 to 1.5 wt % was employed:[28]

$$\eta_{sp} = 24832 c_{CNC}^2 + 283.8 c_{CNC} \tag{36}$$

where η_{sp} is the specific viscosity of the suspension of CNCs in water and c_{CNC} is the concentration of CNCs in the suspension in g mL^{-1}. Comparison of this model to other rheological characterization of aqueous CNC suspensions provides reasonable agreement of this model up to approximately 6 wt % as illustrated in Figure S3-9.[36]

Hydrodynamic-induced alignment was studied through the rotational Péclet number described by Willenbacher and Georgieva, Equations (37) and (38), which expresses the extent to which hydrodynamic forces overcome Brownian motion in controlling alignment.[43]

$$P\acute{e}_{rot} = \tau_{rot}\dot{\gamma} \tag{37}$$

$$\tau_{rot} = \frac{8\pi\eta_s a^3}{3k_B T(ln2r_p - 0.5)} \quad (38)$$

where $\dot{\gamma}$ is the shear rate, τ_{rot} is the rotational relaxation time, η_s is the solvent viscosity, a is the length of the semi-major axis of a prolate spheroid representing the rod-like particle, k_B is the Boltzmann constant, T is temperature in Kelvin, and r_p is the aspect ratio of the particle. Rotational Péclet numbers greater than unity describe systems in which shear induced flow alignment dominates. Alignment in systems with Péclet numbers less than unity is governed by Brownian motion acting to randomize the orientation of particles. The rotational relaxation time was evaluated with Equation (3) and was found to be 2.1 x 10^{-4} s for CNCs at 23.5 °C used in this work, corresponding to a solvent viscosity of 1 mPa s, CNC length of 123 nm, and CNC aspect ratio of 5.1. Therefore, shear rates greater than 4.73 x 10^3 s^{-1} should lead to hydrodynamic flow alignment.

Rotational Péclet numbers were calculated from Equation (37) for an evaporating water droplet and CNC suspension droplet over the course of evaporation at 23.5 °C, Figure S3-10 and were found to be constant with respect to time and droplet location in room temperature evaporation. The Rotational Péclet number, $3.2\ x\ 10^{-12}$, is very significantly less than unity suggesting that Brownian motion dominates, and particles remain in their initial isotropic (unaligned) orientation as they are carried to the edge of the droplet. The hydrodynamic forces calculated here are without specific particle interaction contributions and are not sufficient to induce significant orientation at 23.5 °C. Particles contained within the suspensions may be entrained in the flow and thus deposited at the edge of the droplet but would not necessarily develop long-range preferential orientation without the effects of additional interactions. Thus,

the bulk of CNC orientation occurs as a result of contact line dynamics, surface tension, and interparticle interactions, supporting Mashkour's[12, 26] advances in this space.

The absence of hydrodynamic alignment was confirmed experimentally, in triplicate, through the characterization of aqueous suspensions of chiral nematic CNCs evaporating on hydrophilic substrates. Isolation of anisotropic phase of a 3.9 wt % aqueous suspension of CNCs was carefully extracted after leaving the suspension to phase separate into its isotropic and chiral nematic phases for one week.[15] While the CNCs were exposed to shear stress during the withdrawal and ejection from the micropipette, the droplets maintained a significant order after placement which was visible through PLM as shown in Figure 3-6. Coupled with time-resolved PLM, supporting information: Droplet Evaporation Video 2, these results illustrate ordered CNCs migrating to the contact line during evaporation. In support of calculations of the rotational Péclet number, local particle orientation is unperturbed by the shear flow. Additionally, clusters of CNCs migrating to the contact line are observed rotating to match the tangential orientation of their neighbors upon their approach, highlighting the role of interparticle interactions governing the orientation of structured domains of deposited CNCs.

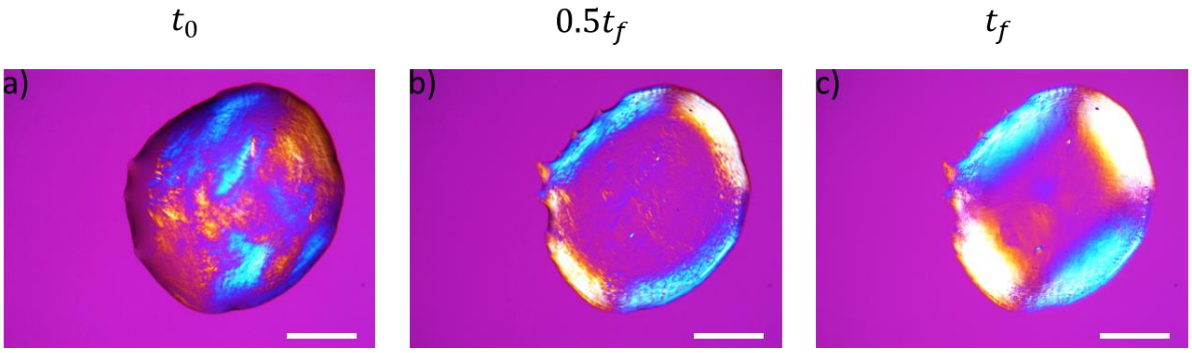

Figure 3-6. Snapshots of a 0.25 µL droplet of an initially chiral nematic 3.9 wt % CNC aqueous suspension evaporating on an Alconox-cleaned glass slide. Time points are observed after intial

deposition, a) t = 9 s, halfway through b) t = 132.5 s, and after evaporation completes c) t = 265 s. Scale bar = 500 µm.

Finally, to analyze the role of the contact line on the evolution of CNC orientation in drying droplets, we explore the effects of hydrophobicity on the ensuing particle deposition in triplicate as depicted in Figure 3-7 and supporting information: Droplet Evaporation Video 3. Hydrophobic droplets commonly evaporate with a receding contact line to maintain their contact angle with the substrate throughout evaporation and therefore serve as an excellent technique to observe the role of contact line motion in the development of CNC orientation.[1, 44] We expect the contact line to recede in droplets containing negatively-charged suspended CNCs, Figure 3-7a-c, until the CNC concentration exceeds the gel point.[45]

The initial stages of evaporation on a hydrophobic substrate are notably different from hydrophilic surfaces. The near instantaneous formation of CNC alignment near the contact line, as shown previously, is not observed. In fact, ordered domains of CNCs are not visibly apparent under PLM until nearly three-quarters of the evaporation time has elapsed, Figure 3-7c. While tangentially aligned CNCs are observed at this time, their ultimate configuration, Figure 3-7d, is difficult to discern. Once gelation is established and the droplet remains fixed, evaporation proceeds to evolve the remaining water within the CNC network. The removal of the interstitial water results in a collapse in the height of the droplet as well as a reduction in inter-CNC spacing.[46] This results in a semi-ordered deposit, likely comprised of many tactoids of aligned regions of CNCs, but lacks the regular arrangement of nanoparticles following evaporation on a hydrophilic substrate. In this case, CNCs are not given the opportunity to deposit at a pinned contact line during evaporation or cooperatively develop a tangentially aligned structure in the proximity of the contact line. Instead, the restricted time for reorganization after gelation and

before solvent removal reduces the free volume leading to severely hindered particle mobility and ultimately smaller domains of ordered structures.

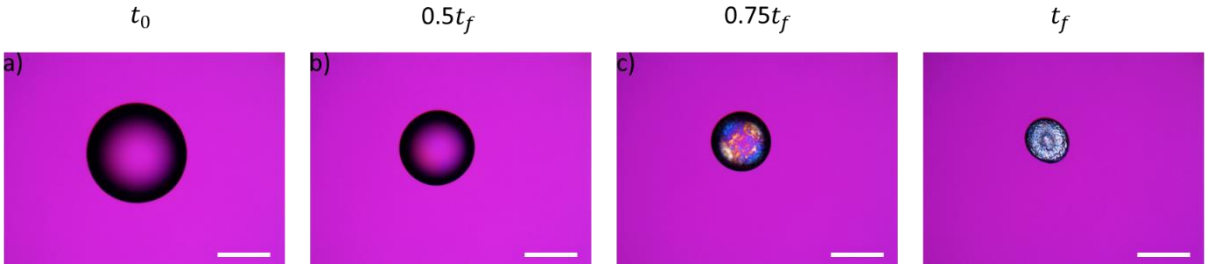

Figure 3-7. Snapshots of a 0.5 µL droplet of 2 wt % CNC aqueous suspension evaporating on a Rain-X-cleaned glass slide. Time points are observed after intial deposition, a) $t = 5$ s, halfway through b) $t = 225$ s, c) $t = 330\ s$, and after evaporation completes c) $t = 445$ s. Scale bar = 500 µm.

3.5 Conclusions

Time-resolved polarized light microscopy provides a powerful tool for the characterization of optically anisotropic nanomaterials which dynamically develop ordered structures larger than the wavelength of visible light. These structures can be identified in real-time thereby illuminating complex structural interactions, traditionally observed only in steady state flow or *ex post facto*. We present evidence of multiple modes of particle alignment in evaporating aqueous suspensions of cellulose nanocrystals (CNCs) as a function of the local particle concentration. Pinned droplets initially carry CNCs to the edge where they accumulate to form a coffee-ring and orient parallel to the droplet boundary. Below a critical particle concentration remaining in the liquid body, the contact line begins to recede until evaporation is complete. During this recession, CNCs proximate to the contact line temporarily develop a radial orientation, but ultimately deposit tangentially. Further, as the local particle concentration at the

moving interface decreases below a packing threshold, CNCs are able to deposit while maintaining their radial alignment near the center of the droplet and near the end of evaporation. Finally, as the droplet volume shrinks towards complete evaporation, particles become further confined leading to a tangential particle alignment at the very center of the droplet.

The evolution of particle orientation throughout the droplet is highly dependent on the interfacial surface tension and cooperative interactions between CNCs. The surface tension acts to aid the initial CNC rotation coincident to the contact line which defines the orientation for particles deposited within the coffee-ring. Additionally, variations in particle concentration during evaporation enable shifts in particle orientation. We present the deposition of highly ordered ring structures from dilute CNC suspensions which can be varied in size through the droplet volume. Accordingly, a comprehensive analysis of the concentration- and shear rate-dependent nature of viscosity and interparticle interactions, especially in highly concentrated systems, may further elucidate parameters associated with the development of highly ordered, radial or tangential, structures applicable to the next generation of spatially and directionally ordered systems of anisotropic nanomaterials.

3.6 Associated Content

Supporting Information

The following files are available free of charge.

Computational fluid dynamic model (CFD) description, CFD Meshes, CFD Governing Equations, CFD Material Parameters, Viscosity model validation, Rotational Péclet number

analysis, Evaporation of droplets of CNC suspensions on a hydrophobic substrate as a function of CNC concentration

Droplet Evaporation Video 1: PLM video of a 0.25 µL droplet of a 2 wt % CNC aqueous suspension evaporating on an Alconox-cleaned glass slide.

Droplet Evaporation Video 2: PLM video of a 0.25 µL droplet of an initially chiral nematic 3.9 wt % CNC aqueous suspension evaporating on an Alconox-cleaned glass slide.

Droplet Evaporation Video 3: PLM video of a 0.5 µL droplet of a 2 wt % CNC aqueous suspension evaporating on a Rain-X-cleaned glass slide.

Author Contributions

F. N. contributed to the experimental droplet evaporation studies and characterization via PLM and AFM. C. Q. P. contributed to the time-resolved PLM, finite element modeling, and all data analysis. All authors discussed the results and contributed to writing the manuscript.

Funding Sources

Department of Education GAANN Fellowship program (DEd-23039). USDA Cooperative State Research, Education and Extension Service (2005-35504-16088).

Notes

The authors declare no competing financial interest.

3.7 Acknowledgements

The authors gratefully acknowledge generous scholarship support for F. N. by the Mexican department of Education (SEP) through its Professional Development for Teachers program

(PROMEP). This project was further supported by the National Research Initiative of the USDA Cooperative State Research, Education and Extension Service, grant number 2005-35504-16088. We thank OMNOVA, Inc. and Tembec, Inc. for supplying the cellulose pulp used in this work. Additionally, we would like to acknowledge the Department of Education GAANN Fellowship program (DEd-23039) for their funding and support for this work.

3.8 Abbreviations

CNC, cellulose nanocrystal; FEM, finite element modeling; PLM, polarized light microscopy; AFM, atomic force microscopy.

References

1. Petsi, A. J.; Burganos, V. N., Evaporation-induced flow in an inviscid liquid line at any contact angle. *Physical Review E - Statistical, Nonlinear, and Soft Matter Physics* **2006,** *73*, 1-9.
2. Deegan, R. D.; Bakajin, O.; Dupont, T. F.; Huber, G.; Nagel, S. R.; Witten, T. A., Capillary flow as the cause of ring stains from dried liquid drops. *Nature* **1997,** *389* (6653), 827-829.
3. Deegan, R. D.; Bakajin, O.; Dupont, T. F.; Huber, G.; Nagel, S. R.; Witten, T. A., Contact line deposits in an evaporating drop. *Phys Rev E Stat Phys Plasmas Fluids Relat Interdiscip Topics* **2000,** *62* (1), 756-765.
4. Maillard, M.; Motte, L.; Pileni, M. P., Rings and Hexagons Made of Nanocrystals. *Advanced Materials* **2001,** *13* (3), 200-204.
5. Hu, H.; Larson, R. G., Marangoni effect reverses coffee-ring depositions. *J Phys Chem B* **2006,** *110* (14), 7090-7094.
6. Gencer, A.; Schutz, C.; Thielemans, W., Influence of the Particle Concentration and Marangoni Flow on the Formation of Cellulose Nanocrystal Films. *Langmuir* **2017,** *33* (1), 228-234.
7. Gencer, A.; Van Rie, J.; Lombardo, S.; Kang, K.; Thielemans, W., Effect of Gelation on the Colloidal Deposition of Cellulose Nanocrystal Films. *Biomacromolecules* **2018,** *19* (8), 3233-3243.
8. Mu, X.; Gray, D. G., Droplets of cellulose nanocrystal suspensions on drying give iridescent 3-D “coffee-stain” rings. *Cellulose* **2015,** *22* (2), 1103-1107.
9. Ye, S.; Fu, Q.; Ge, J., Invisible Photonic Prints Shown by Deformation. *Advanced Functional Materials* **2014,** *24* (41), 6430-6438.

10. Saha, P.; Ansari, N.; Kitchens, C. L.; Ashurst, W. R.; Davis, V. A., Microelectromechanical Systems from Aligned Cellulose Nanocrystal Films. *ACS Appl Mater Interfaces* **2018,** *10* (28), 24116-24123.
11. Hoeng, F.; Denneulin, A.; Bras, J., Use of nanocellulose in printed electronics: a review. *Nanoscale* **2016,** *8* (27), 13131-13154.
12. Mashkour, M.; Kimura, T.; Mashkour, M.; Kimura, F.; Tajvidi, M., Printing Birefringent Figures by Surface Tension-Directed Self-Assembly of a Cellulose Nanocrystal/Polymer Ink Components. *ACS Appl Mater Interfaces* **2019,** *11* (1), 1538-1545.
13. Foster, E. J.; Moon, R. J.; Agarwal, U. P.; Bortner, M. J.; Bras, J.; Camarero-Espinosa, S.; Chan, K. J.; Clift, M. J. D.; Cranston, E. D.; Eichhorn, S. J.; Fox, D. M.; Hamad, W. Y.; Heux, L.; Jean, B.; Korey, M.; Nieh, W.; Ong, K. J.; Reid, M. S.; Renneckar, S.; Roberts, R.; Shatkin, J. A.; Simonsen, J.; Stinson-Bagby, K.; Wanasekara, N.; Youngblood, J., Current characterization methods for cellulose nanomaterials. *Chem Soc Rev* **2018,** *47* (8), 2609-2679.
14. Revol, J. F.; Bradford, H.; Giasson, J.; Marchessault, R. H.; Gray, D. G., Helicoidal self-ordering of cellulose microfibrils in aqueous suspension. *International Journal of Biological Macromolecules* **1992,** *14* (3), 170-172.
15. Schutz, C.; Agthe, M.; Fall, A. B.; Gordeyeva, K.; Guccini, V.; Salajkova, M.; Plivelic, T. S.; Lagerwall, J. P.; Salazar-Alvarez, G.; Bergstrom, L., Rod Packing in Chiral Nematic Cellulose Nanocrystal Dispersions Studied by Small-Angle X-ray Scattering and Laser Diffraction. *Langmuir* **2015,** *31* (23), 6507-6513.
16. Lagerwall, J. P. F.; Schütz, C.; Salajkova, M.; Noh, J.; Hyun Park, J.; Scalia, G.; Bergström, L., Cellulose nanocrystal-based materials: from liquid crystal self-assembly and glass formation to multifunctional thin films. *NPG Asia Materials* **2014,** *6* (1), 1-12.
17. Hamad, W. Y., *Cellulose Nanocrystals Properties, Production, and Applications*. John Wiley & Sons Ltd: 2017; p 289.
18. Tatsumi, M.; Kimura, F.; Kimura, T.; Teramoto, Y.; Nishio, Y., Anisotropic polymer composites synthesized by immobilizing cellulose nanocrystal suspensions specifically oriented under magnetic fields. *Biomacromolecules* **2014,** *15* (12), 4579-4589.
19. De France, K. J.; Yager, K. G.; Hoare, T.; Cranston, E. D., Cooperative Ordering and Kinetics of Cellulose Nanocrystal Alignment in a Magnetic Field. *Langmuir* **2016,** *32* (30), 7564-7571.
20. Dhar, P.; Kumar, A.; Katiyar, V., Magnetic Cellulose Nanocrystal Based Anisotropic Polylactic Acid Nanocomposite Films: Influence on Electrical, Magnetic, Thermal, and Mechanical Properties. *ACS Appl Mater Interfaces* **2016,** *8* (28), 18393-18409.
21. Tatsumi, M.; Teramoto, Y.; Nishio, Y., Different orientation patterns of cellulose nanocrystal films prepared from aqueous suspensions by shearing under evaporation. *Cellulose* **2015,** *22* (5), 2983-2992.
22. Cranston, E. D.; Gray, D. G., Birefringence in spin-coated films containing cellulose nanocrystals. *Colloids and Surfaces A: Physicochemical and Engineering Aspects* **2008,** *325* (1-2), 44-51.
23. Chen, S.; Schueneman, G.; Pipes, R. B.; Youngblood, J.; Moon, R. J., Effects of crystal orientation on cellulose nanocrystals-cellulose acetate nanocomposite fibers prepared by dry spinning. *Biomacromolecules* **2014,** *15* (10), 3827-3835.

24. O'Shea, J. N.; Taylor, J. B.; Swarbrick, J. C.; Magnano, G.; Mayor, L. C.; Schulte, K., Electrospray deposition of carbon nanotubes in vacuum. *Nanotechnology* **2007,** *18*.
25. Xin, H.; Woolley, A. T., Directional orientation of carbon nanotubes on surfaces using a gas flow cell. *Nano Letters* **2004,** *4*, 1481-1484.
26. Mashkour, M.; Kimura, T.; Kimura, F.; Mashkour, M.; Tajvidi, M., Tunable self-assembly of cellulose nanowhiskers and polyvinyl alcohol chains induced by surface tension torque. *Biomacromolecules* **2014,** *15* (1), 60-65.
27. Roman, M.; Navarro, F., Deposition of Cellulose Nanocrystals by Inkjet Printing. In *Model Cellulosic Surfaces*, American Chemical Society: 2009; Vol. 1019, pp 157-171 SE - 7.
28. Li, M. C.; Wu, Q.; Song, K.; Lee, S.; Qing, Y.; Wu, Y., Cellulose Nanoparticles: Structure-Morphology-Rheology Relationships. *ACS Sustainable Chemistry and Engineering* **2015,** *3*, 821-832.
29. Mu, X.; Gray, D. G., Droplets of cellulose nanocrystal suspensions on drying give iridescent 3-D "coffee-stain" rings. *Cellulose* **2015,** *22*, 1103-1107.
30. Ghasemi, S.; Rahimzadeh-Bajgiran, P.; Tajvidi, M.; Shaler, S. M., Birefringence-based orientation mapping of cellulose nanofibrils in thin films. *Cellulose* **2019,** *27* (2), 677-692.
31. Maren Roman, F. N., Deposition of Cellulose Nanocrystals by Inkjet Printing. In *Model Cellulosic Surfaces*, ACS Publications: 2009; pp 157-171.
32. Roman, M.; Gray, D. G., Parabolic focal conics in self-assembled solid films of cellulose nanocrystals. *Langmuir* **2005,** *21* (12), 5555-5561.
33. Gray, D. G.; Mu, X., Chiral Nematic Structure of Cellulose Nanocrystal Suspensions and Films; Polarized Light and Atomic Force Microscopy. *Materials (Basel)* **2015,** *8* (11), 7873-7888.
34. Al-Milaji, K. N.; Zhao, H., Probing the Colloidal Particle Dynamics in Drying Sessile Droplets. *Langmuir* **2019,** *35* (6), 2209-2220.
35. Shanahan, M. E. R., Simple Theory of "Stick-Slip" Wetting Hysteresis. *Langmuir* **1995,** *11* (3), 1041-1043.
36. Liao, J.; Pham, K. A.; Breedveld, V., Rheological characterization and modeling of cellulose nanocrystal and TEMPO-oxidized cellulose nanofibril suspensions. *Cellulose* **2020,** *27* (7), 3741-3757.
37. Cavallaro, M., Jr.; Botto, L.; Lewandowski, E. P.; Wang, M.; Stebe, K. J., Curvature-driven capillary migration and assembly of rod-like particles. *Proc Natl Acad Sci U S A* **2011,** *108* (52), 20923-20928.
38. Botto, L.; Yao, L.; Leheny, R. L.; Stebe, K. J., Capillary bond between rod-like particles and the micromechanics of particle-laden interfaces. *Soft Matter* **2012,** *8* (18), 4971–4979.
39. Hoeger, I.; Rojas, O. J.; Efimenko, K.; Velev, O. D.; Kelley, S. S., Ultrathin film coatings of aligned cellulose nanocrystals from a convective-shear assembly system and their surface mechanical properties. *Soft Matter* **2011,** *7* (5), 1957–1967.
40. Alizadehgiashi, M.; Khabibullin, A.; Li, Y.; Prince, E.; Abolhasani, M.; Kumacheva, E., Shear-Induced Alignment of Anisotropic Nanoparticles in a Single-Droplet Oscillatory Microfluidic Platform. *Langmuir* **2018,** *34* (1), 322-330.
41. Krieger, I. M.; Dougherty, T. J., A Mechanism for Non-Newtonian Flow in Suspensions of Rigid Spheres. *Transactions of the Society of Rheology* **1959,** *3*, 137-152.

42. Doi, M.; Edwards, S. F., The Theory of Polymer Dynamics. **1988**, 391.
43. Willenbacher, N.; Georgieva, K., Rheology of Disperse Systems. In *Product Design and Engineering: Formulation of Gels and Pastes*, Brockel, U.; Meier, W.; Gerhard, W., Eds. 2013; pp 7-49.
44. Kim, D. O.; Pack, M.; Rokoni, A.; Kaneelil, P.; Sun, Y., The effect of particle wettability on the stick-slip motion of the contact line. *Soft Matter* **2018,** *14* (47), 9599-9608.
45. Gray, D. G., Order and gelation of cellulose nanocrystal suspensions: an overview of some issues. *Philos Trans A Math Phys Eng Sci* **2018,** *376* (2112), 1-7.
46. Jativa, F.; Schutz, C.; Bergstrom, L.; Zhang, X.; Wicklein, B., Confined self-assembly of cellulose nanocrystals in a shrinking droplet. *Soft Matter* **2015,** *11* (26), 5374-5380.

3.9 Supporting Information

3.9.1 Time-resolved Polarized Light Microscopy (PLM) Videos

Droplet Evaporation Video 1:

0.25 µL droplet of a 2 wt % CNC aqueous suspension evaporating on an Alconox-cleaned glass slide viewed under PLM with a 530 nm first-order retardation plate at 4X magnification.

Droplet Evaporation Video 2:

0.25 µL droplet of an initially chiral nematic 3.9 wt % CNC aqueous suspension evaporating on an Alconox-cleaned glass slide viewed under PLM with a 530 nm first-order retardation plate at 4X magnification.

Droplet Evaporation Video 3:

0.5 µL droplet of 2 wt % CNC aqueous suspension evaporating on a Rain-X-cleaned glass slide viewed under PLM with a 530 nm first-order retardation plate at 4X magnification.

3.9.2 Computational Fluid Dynamic (CFD) Model

3.9.2.1 Finite Element Boundary and Initial Conditions

COMSOL's deforming mesh physics module was implemented with the droplet-substrate interface as a fixed mesh to simulate constant contact area evaporation. The air-water interface was given a prescribed normal mesh velocity related to evaporation rate of water. Boundaries generated for symmetry were allowed to deform freely.

Mass transport was evaluated with COMSOL's transport of diluted species module. No flux was allowed to transport through the substrate, and water leaving the boundaries of the air domain was driven by convection. The initial concentration of water in the droplet and surrounding air was 55.5 M and 1.28 mM, the vapor pressure of water at 20°C, respectively.

Flow near the substrate was treated with the no-slip condition and initially the droplet was assumed to be stagnant. All flow was generated by evaporation induced gradients.

The fluid was treated as a phase change material in COMSOL taking into account the latent heat of vaporization. The boundaries of the air domain were held at room temperature, 23.5°C, and the droplet substrate treated maintained at 23.5°C. Initially the droplet was set to 23.5°C and the ambient air was room temperature. A Marangoni shear stress was also applied to the air-water interface as a function of the tangent temperature gradient and surface tension.

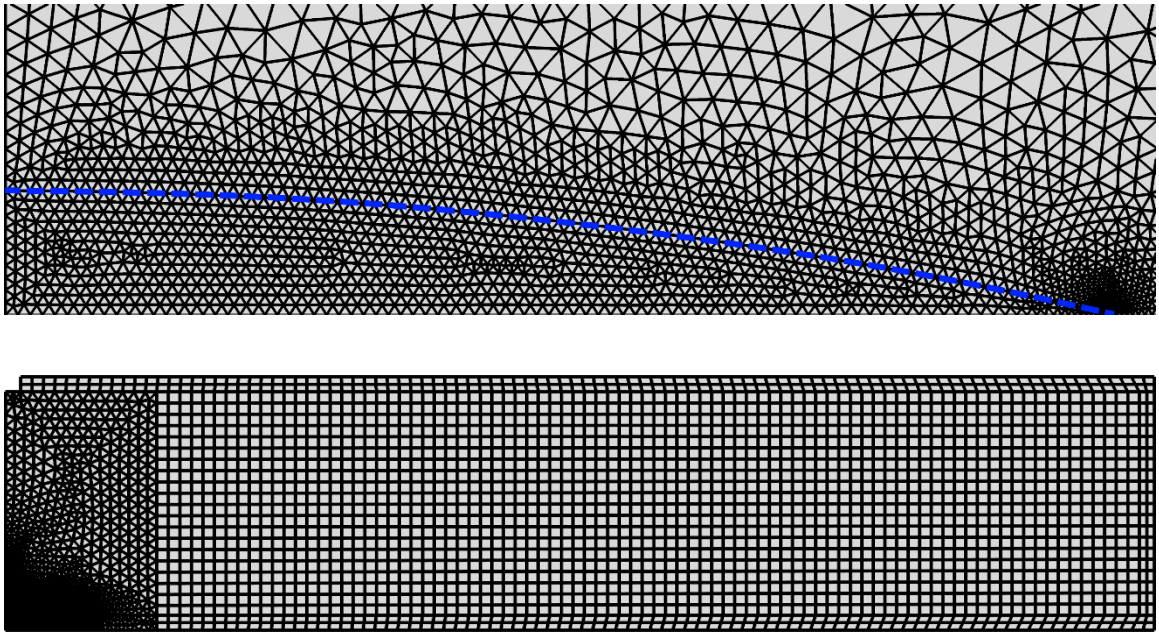

Figure S3-8. Finite element mesh of droplet (top) and surrounding petri dish (bottom)

Table S3-1. CFD model governing transport equations and mixture rules

Governing Equations

Continuity equation	$\frac{\partial \rho}{\partial t} + \boldsymbol{\nabla} \cdot (\rho \boldsymbol{u}) = 0$
Navier-Stokes (α, Droplet)	$\rho \frac{\partial \boldsymbol{u^{\alpha}}}{\partial t} + \rho(\boldsymbol{u^{\alpha}} \cdot \boldsymbol{\nabla})\boldsymbol{u^{\alpha}} = \boldsymbol{\nabla} \cdot \left[-p\boldsymbol{I} + \mu(\boldsymbol{\nabla u^{\alpha}} + (\boldsymbol{\nabla u^{\alpha}})^T) - \frac{2}{3}\mu(\boldsymbol{\nabla} \cdot \boldsymbol{u^{\alpha}})\boldsymbol{I}\right]$
Navier-Stokes (β, Air)	$\rho \frac{\partial \boldsymbol{u^{\beta}}}{\partial t} + \rho\left(\boldsymbol{u^{\beta}} \cdot \boldsymbol{\nabla}\right)\boldsymbol{u^{\beta}} = \boldsymbol{\nabla} \cdot \left[-p\boldsymbol{I} + \mu\left(\boldsymbol{\nabla u^{\beta}} + \left(\boldsymbol{\nabla u^{\beta}}\right)^T\right) - \frac{2}{3}\mu\left(\boldsymbol{\nabla} \cdot \boldsymbol{u^{\beta}}\right)\boldsymbol{I}\right]$
Mass transport	$\frac{\partial c_i}{\partial t} + \boldsymbol{\nabla} \cdot (-D\boldsymbol{\nabla} c_i) + \boldsymbol{u} \cdot \boldsymbol{\nabla} c_i = 0$
Deforming Mesh Velocity	$v_{interface} = \frac{\sqrt{r_{drop}^2 - x^2} - h_{offset}}{t_{evap}}$
Heat transport	$\rho C_p \left(\frac{\partial T}{\partial t} + \boldsymbol{u} \cdot \boldsymbol{\nabla} T\right) + \nabla \cdot (k\boldsymbol{\nabla} T) = Q$

Table S3-2 Fluid and chemical species properties for CFD model

Symbol	Name	Value	Units
$\boldsymbol{\rho_{H2O}}$	Density of water at 23.5°C	1000	$\frac{kg}{m^3}$
$\boldsymbol{\rho_{PS}}$	Density of polystyrene at 23.5°C	1000	$\frac{kg}{m^3}$
$\boldsymbol{k^{PS}}$	Thermal conductivity of polystyrene	0.033	$\frac{W}{m\,K}$
$\boldsymbol{C_p^{PS}}$	Heat Capacity of polystyrene[1]	1.19	$\frac{kJ}{kg \cdot K}$
$\boldsymbol{k^{glass}}$	Thermal conductivity of glass	1.40	$\frac{W}{m\,K}$
$\boldsymbol{C_p^{glass}}$	Heat Capacity of glass	0.730	$\frac{kJ}{kg \cdot K}$

$\boldsymbol{\Delta H_{vap}}$	Specific latent heat of vaporization for water	2.257×10^6	J/kg
$\boldsymbol{T_{amb}}$	Ambient air temperature	296.65	K
$\boldsymbol{T_{droplet}}$	Water droplet temperature	296.65	K
$\boldsymbol{c_0^{CNC}}$	Initial concentration of cellulose nanocrystals for viscosity correlation	7.65	$\frac{g}{L}$
$\boldsymbol{c_0^{\alpha}}$	Initial concentration of water in the liquid phase	5.55×10^4	mol/m^3
$\boldsymbol{c_0^{\beta}}$	Initial concentration of water in the vapor phase	1.28	mol/m^3
$\boldsymbol{D}$	Water-air Binary Diffusivity	2.62×10^{-5}	$\frac{m^2}{s}$
$\boldsymbol{\tau_{rot}}$	Rotational relaxation time	2.11×10^{-4}	s
$\boldsymbol{r_{drop}}$	Radius of spherical cap	10.27	mm
$\boldsymbol{h_{offset}}$	Spherical cap vertical offset	0.1	mm
$\boldsymbol{t_{evap}}$	Evaporation time	180	s
$\boldsymbol{V_0}$	Initial water droplet volume	2	μL

3.9.3 Viscosity Model Validation

While the implemented viscosity model from Li et al was originally measured with CNC concentrations ranging from 0.25 to 1.5 wt %, the model was extrapolated in our simulations to 5.2 wt %.[2] Here we address the validity of our extrapolation by comparison to additional literature data for the viscosity of CNC suspensions. Implementation of a piecewise power law-Cross model

from Liao et al reveals good agreement, Figure S3-9, between the models up to approximately 6 wt %.[3] This agreement fulfils the concentration regimes explored in this study and suggests that at low concentrations, where CNC suspensions do not strongly deviate from Newtonian behavior, the selected concentration-dependent viscosity model can be extrapolated to medium concentrations for CNC suspensions.

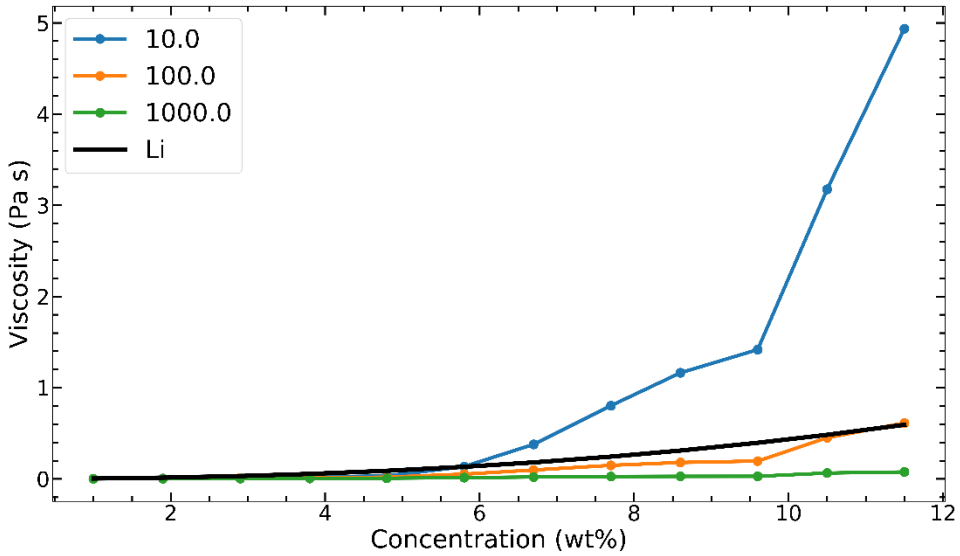

Figure S3-9. Comparison of CNC suspension viscosity models as a function of CNC concentration between Li et al. (black) and Liao et al. at various shear rates.

3.9.4 Rotational Péclet Number

The rotational Péclet number, Figure S3-10, was calculated from Equation (1), as reported in the main text, using the above CFD model to evaluate the influence of hydrodynamic shear on alignment of CNCs during evaporation. Rotational Péclet significantly less than one indicate Brownian motion dominates CNCs alignment and CNCs are not aligned as a result of their migration to the contact line.

$$P\acute{e}_{rot} = \tau_{rot}\dot{\gamma} \tag{39}$$

$$\tau_{rot} = \frac{8\pi\eta_s a^3}{3k_B T(ln2r_p - 0.5)} \tag{40}$$

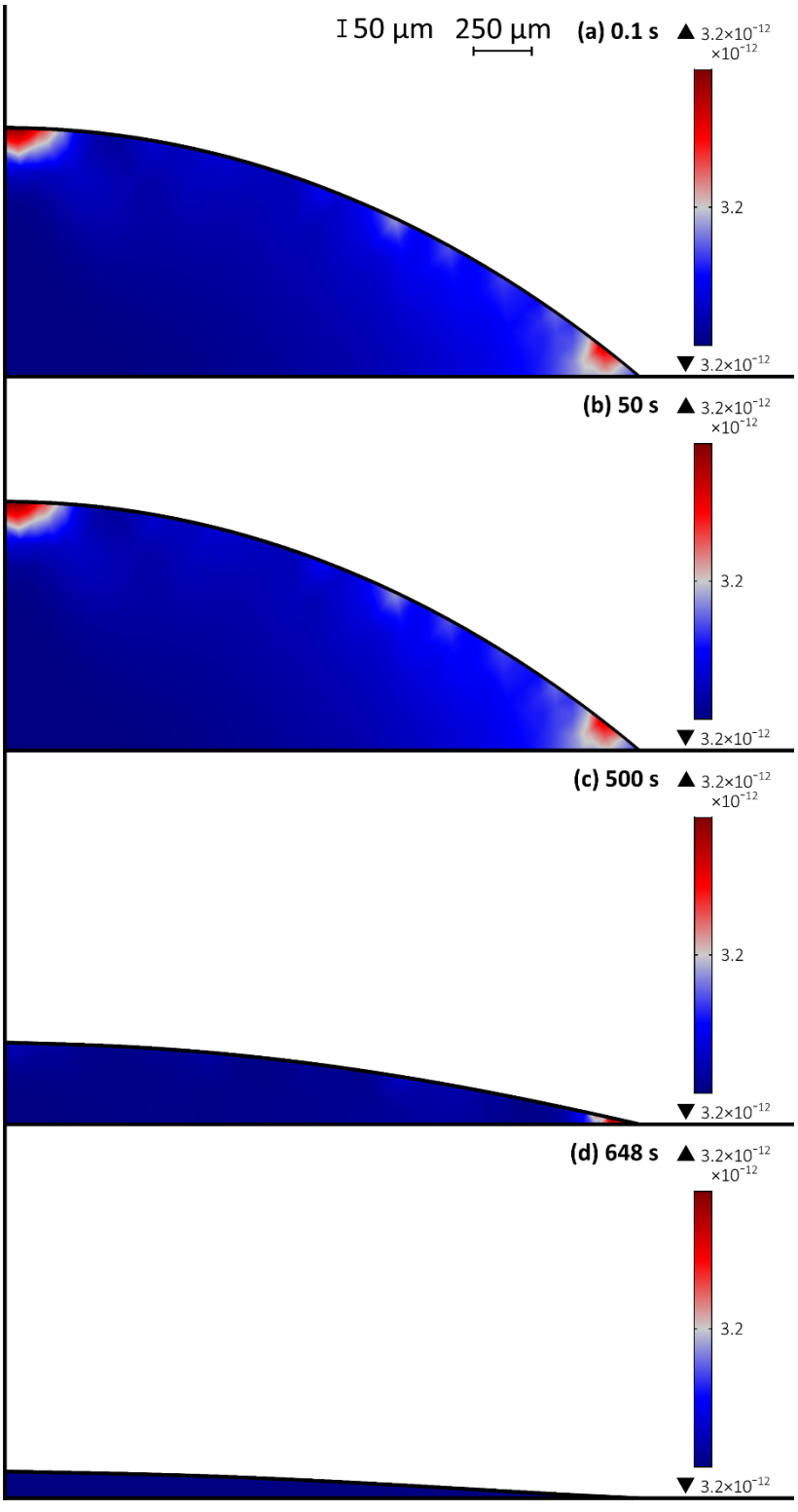
50 µm
250 µm
(a) 0.1 s
3.2×10⁻¹²
×10⁻¹²
3.2
3.2×10⁻¹²
(b) 50 s
3.2×10⁻¹²
×10⁻¹²
3.2
3.2×10⁻¹²
(c) 500 s
3.2×10⁻¹²
×10⁻¹²
3.2
3.2×10⁻¹²
(d) 648 s
3.2×10⁻¹²
×10⁻¹²
3.2
3.2×10⁻¹²

Figure S3-10. Rotational Péclet number distribution as a function of time in an evaporating droplet of a 1 wt % CNC at 23.5°C suspension indicating nanoparticle alignment is governed by Brownian motion as opposed to hydrodynamic shear.

3.9.5 Influence of CNC Concentration in Evaporation on a Hydrophobic Substrate

Deposits, Figure S3-11, resulting from the evaporation of droplets of CNC suspensions were evaluated as a function of the initial CNC concentration from 0.1 to 3.9 wt %. The deposits were observed to increase in radius with more CNCs beginning in the droplet. The increased concentration results in a larger volume of deposit as the total dry mass is increased. Additionally, the increased initial concentration leads to faster gelation limiting further recession of the contact line. As a result, the deposits in Figure S3-11a-e exhibit a doughnut morphology rather than a spherical deposit.

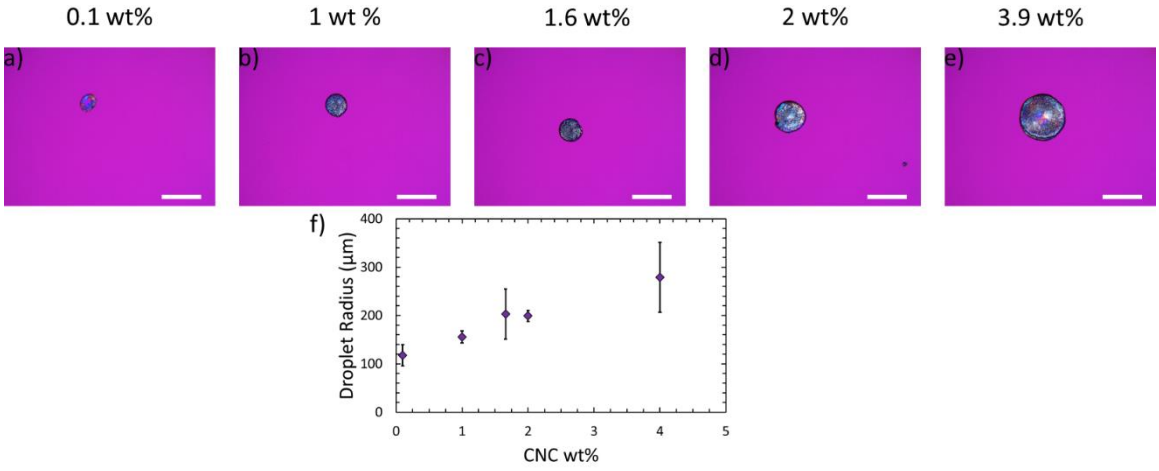

Figure S3-11. PLM of 0.5 µL droplets of aqueous CNC suspensions with a) 0.1, b) 1, c) 1.66, d) 2, e) 3.9 wt % CNCs evaporating on Rain-X-cleaned glass slides. f) the radius of the deposits after evaporation and as a function of CNC concentration.

References

1. Colbert, J. C., NIST SRM 705a - polystyrene. National Institue of Standards and Technology: 1990.
2. Li, M. C.; Wu, Q.; Song, K.; Lee, S.; Qing, Y.; Wu, Y., Cellulose Nanoparticles: Structure-Morphology-Rheology Relationships. *ACS Sustainable Chemistry and Engineering* **2015,** *3*, 821-832.
3. Liao, J.; Pham, K. A.; Breedveld, V., Rheological characterization and modeling of cellulose nanocrystal and TEMPO-oxidized cellulose nanofibril suspensions. *Cellulose* **2020,** *27* (7), 3741-3757.

Chapter 4 - Diffusion-softening of Cellulose Nanocrystal and Thermoplastic Polyurethane Composites

Cailean Q. Pritchard,[1,4,+] Jacob J. Fallon,[2,4,+] Jeffrey Shelton[1], Cody Weyhrich[3,4], Katherine Heifferon[3,4], Boer Liu[3,4], Timothy E. Long[3,4], E. Johan Foster[5], Michael J. Bortner,[*1,4]

[1]Department of Chemical Engineering, [2]Department of Macromolecular Science and Engineering, [3]Department of Chemistry, and [4]Macromolecules Innovation Institute, Virginia Tech
[5]Department of Chemical and Biological Engineering, The University of British Columbia

+Denotes Co-First Author
*Corresponding author

This chapter is presented in the format of a manuscript that is in preparation for submission to ACS Applied Materials and Interfaces.

The following contributions were made by other authors: Conceptualization of research scope and methodology were developed by Cailean Q. Pritchard and Jacob J. Fallon. Investigation of the storage modulus during water absorption was conducted by Jacob J. Fallon. Percolation and Halpin-Kardos models were implemented by Jacob J. Fallon. Mass uptake experiments were conducted by Cody Weyhrich, Katherine Heifferon, and Boer Liu. Time-dependent FTIR-ATR experiments were conducted by Jacob J. Fallon, Cailean Q. Pritchard, and Jeffrey Shelton.

The following people contributed to the writing of this chapter: Cailean Q. Pritchard (Original Draft), Jacob J. Fallon (Drafting of Preliminary Work), and Michael J. Bortner (Review and Editing)

4.1 Abstract

The mechanical adaptivity of polymer composites containing cellulose nanocrystals (CNCs) is of broad interest for the development of smart materials. The mechanism leading to diffusion-dependent mechanical softening in response to water uptake in these materials is well understood, however, the mass transport driving this phenomenon has not been completely resolved. Understanding such behavior would further enable the mechanism to be controlled and exploited for various applications. Here, we show that swelling of the bulk polymer composite during moisture uptake results in a decreased apparent diffusivity with increasing CNC concentration, despite the equilibrium water uptake increasing concurrently. Further, we demonstrate that a modification to the widely used percolation model predicts the full time-dependent evolution of storage modulus during the softening process by associating mass transport directly to the softening response. This model will be pertinent to studies of mechanical responses in CNC-polymer composites and is expected to be generally applicable to percolating networks which deactivate in response to a given stimulus.

4.2 Introduction

Mechanically adaptive materials are increasingly in demand due to their dynamic properties which enable the development of smart materials that can react to varying sources of stimuli. Several mechanically adaptive polymer composites have been developed to mimic the behavior of the sea cucumber dermis by utilizing cellulose nanocrystals (CNCs) to impart a softening response to water exposure.[1,2-6] These materials exploit the tendency of CNCs to develop network structures, interconnected via hydrogen bonding in polymer matrices, increasing the composite's stiffness. Prevailing literature reports suggest the diffusion of water into these CNC-containing polymer films results in a reduction in storage modulus as water disrupts the hydrogen bonding network connecting CNCs and softens the polymer film.[2, 3, 7-10]

The mechanical reinforcement of composites, containing CNCs have been widely studied and predicted using various mathematical models.[2, 11-14] In particular thermoplastic polyurethanes (TPUs) are commonly reinforced with CNCs to create smart materials which adapt to the presence of water while maintaining biocompatibility.[15-19] Notably, several studies have effectively implemented a percolation model, which describes the formation of a percolating network above a critical concentration of CNCs, to predict the dry state modulus.[10, 17] Above this percolation threshold, the storage modulus is drastically enhanced. However, this model is unable to describe the mechanical performance after water is introduced into the nanocomposites which disrupts the percolating network. Instead, the Halpin-Kardos model has been implemented to describe the wet state modulus as a function of filler concentration for such reinforced matrices that do not exhibit filler-filler interactions.[10, 17, 20]

The time associated with the diffusion of water into nanocomposites is highly significant as it enables additional control over the mechanical response. In this regard, the use of CNCs as fillers in polymer matrices can lead to enhanced tuning of mechanical performance to end-use applications. However, little is known about the filler-concentration-dependent diffusive behavior of water inside the polymer matrix. In particular, while a study showed the hydrophilicity of CNCs played a direct role in the rate of softening,[2] a consensus on the impact of CNC concentration and their resulting percolating structures on this behavior has not been reached. Currently, CNCs have been suggested to either enhance water transport through hydrophilic interactions[3, 17, 21, 22] or hinder water transport by acting as physical barriers which water must circumnavigate to diffuse[23, 24].

In this study, we attempt enhance our understanding of the water transport mechanism leading to mechanical adaptation in TPU composites. Additionally, we highlight the discrepancies

between the leading water transport theories and experimental behavior of CNC-TPU films in humid environments via dynamic mechanical analysis (DMA) and thermogravimetric analysis coupled with sorption analysis (TGA-SA). We explore both the macro- and micro-scopic diffusion characteristics of CNC-TPU composites as a function of CNC composition to understand the role of CNCs in this phenomenon, as they relate to both mechanical adaptivity and diffusion. Further, we provide a novel method to evaluate the transient mechanical properties of adaptive polymer nanocomposites, which describes both the initial and final moduli between the dry and wet states, as well as, thoroughly capturing the dynamic switching process. By correlating the dynamic mechanical response to the rate of diffusive transport a transient relationship between moisture uptake and mechanical performance is developed that will be consequential to the development of humidity-sensing actuators comprised of CNCs in polymer matrices.

4.3 Materials and Methods

4.3.1 Materials

Covestro Texin Rxt 70A (TPU, 80,000 - 120,000 kg mol^{-1}, density, 1.07 g cm^{-3}) was purchased from Independent Plastic, Inc. (Houston, TX). Melting endotherms of the second heating cycle in non-isothermal differential scanning calorimetry (-60 °C to 250 °C at 10 °C min^{-1}) were analyzed to extract the TPU soft-segment fraction of approximately 11 %. Cellulose nanocrystals (CNC, density, 1.5 g cm^{-3}) were obtained from the University of Maine (Orono, ME) in an aqueous suspension at a nominal concentration of 10.3 wt % and were produced from sulfuric acid hydrolyzed hardwood pulp by Forest Products Laboratory (Madison, WI). The size distribution of CNCs were reported previously.[25] The stock CNC suspension was refrigerated until use when the concentration was measured at approximately 11.8 wt %. Dimethylformamide (DMF) was purchased from Fisher Scientific (Hampton, NH) and used as received.

4.3.2 Sample Preparation

Nanocomposite films of CNCs incorporated into a TPU matrix were prepared via a three-step process comprising of a solvent exchange of the CNC suspension, mixing of CNC suspension and TPU solution, and followed by solvent casting in a controlled environment. CNCs and TPU were combined in a mutually compatible solvent, DMF, to facilitate mixing and achieve effective CNC dispersion. TPU was dissolved in DMF while stirring at 23 °C at 300 rpm over 24 h, yielding 9.92 wt % TPU in DMF. CNCs suspended in water at 11.8 wt % were mixed with DMF such that 1.24 wt % CNCs in DMF on a dry basis was obtained post water removal. Distillation of the CNC-H_2O-DMF mixture was performed using a Heidolph Instruments Laborota 4000 rotary evaporator at 80 °C for 30 min until all water had been removed. The resulting CNC-DMF mixture was stirred for 1 h and then sonicated in a Branson 5800 ultrasonic bath for 24 h. The two mixtures, CNC-DMF and TPU-DMF were subsequently combined proportionally to obtain CNC-TPU-DMF mixtures containing 0 – 15 wt % CNCs in TPU on a dry basis. These mixtures were stirred for 1 h at 300 rpm and then subjected to 8 h of sonication.

The final mixtures containing CNCs, TPU, and DMF was cast on a heated polytetrafluoroethylene (PTFE) surface at 100 °C for 30 min. Solvent casting was performed in a controlled environment under a continuous purge with dry air to maintain low humidity (<10% RH). The cast films were removed from the PTFE surface and placed in a vacuum oven at 60 °C for 1 day to remove any residual DMF. CNC-TPU films were then stored in a non-vacuum desiccator with silica gel until characterized.

4.3.3 Characterization

4.3.3.1 Thermogravimetric Analysis - Mass Uptake/Weight Loss

A TA Instruments Q5500 was used to measure the total mass uptake of water in CNC-TPU films. Water saturated samples were submerged in deionized (DI) H_2O for 48 h and, once removed,

immediately blotted dry with a Kimwipe and loaded in the TGA. The sample chamber was heated from room temperature to 115 °C at a rate of 50 °C min^{-1}. The temperature in the chamber was then maintained at 115 °C for 3 min. The difference in mass between the initial and final measurements was used to calculate the total water uptake.

4.3.3.2 Dynamic Mechanical Analysis

A TA Instruments DMA Q850 fitted with a RH accessory was used to measure the mechanical properties of the CNC-TPU films. Distilled water was used as the water source for the humidity accessory. Samples were cut using a metal blade to a width of 6.35 mm and a length of approximately 20 mm. The film thickness was determined using a Mitutoyo micrometer with a resolution of 2.54 µm. The modulus of each sample was recorded for approximately 100 s prior to exposure to the high humidity environment. The humidity chamber was allowed to equilibrate externally to 25 °C and 80% RH such that, once attached, the sample was immediately exposed to the high humidity air flow. After characterizing the modulus of the dry films, the humidity chamber was attached and subjected the samples to 25 °C and 80% RH air flow. This process was captured during the test run to establish the dry modulus as well as dynamic modulus as a water diffuses into the CNC-TPU films in the same experiment. The test was operated with a preload force of 0.35 N at a frequency of 1 Hz and 0.01% strain with data points collected every 1 s.

4.3.3.3 Thermogravimetric Analysis – Sorption Analysis

A TA Instruments Q5000 TGA SA dynamic vapor sorption analyzer was utilized to characterize the diffusive transport of water into CNC-TPU films. Cylindrical samples were cut to a diameter of 2.8 mm with a C.S. Osborne revolving die punch No 155. Samples were subsequently measured in diameter with a Pittsburgh caliper having a resolution of 0.01 mm and in thickness with a Mitutoyo micrometer with a resolution of 2.54 µm. Samples were vacuum dried for at least 24 h at 60 °C and stored in a desiccator until tested. Before analysis, CNC-TPU samples were

further dried in the TGA-SA at 60 °C and 0.0% relative humidity (RH) for 30 min. The samples then were allowed to equilibrate at 25 °C before initiating the sorption analysis comprising of an isothermal hold at 25 °C and 80.0% RH for 150 min.

4.3.3.4 Atomic Force Microscopy

An Asylum Research MFP-3D-Bio atomic force microscope was used to characterize the CNC dimensions. Sample dimensions were collected in tapping mode (1 Hz, 512 scans, and 512 scans/line) using Olympus AC200TS R3 tips with a radius of 7 nm and a nominal spring constant of 9 N/m. Dilute suspensions of CNCs were spin-coated onto poly-lysine-coated mica disks using a previously established methodology.[26] Over 100 CNCs were measured and their dimensions averaged to calculate an average aspect ratio of 56.6.

4.3.3.5 Attenuated Total Reflectance Fourier Transform Infrared Spectroscopy (ATR-FT-IR)

A Nicolet iS50 FT-IR purchased from Thermo Fischer Scientific (Waltham, MA) was used to perform chemical analysis of the CNC-TPU films and monitor D_2O diffusion as a function of time. D_2O was purchased from Cambridge Isotope Laboratories, Inc. (Andover, MA) and chosen to prevent overlap from FT-IR peaks of H_2O with CNCs or TPU in the measured spectra. CNC-TPU prepared as above were dissolved with DMF on a ZnSe ATR crystal and cast on heated PTFE at 100 °C for 30 min. The cast CNC-TPU sample was loaded into a Gateway ATR flow cell purchased from SPECAC (Orpington, Kent). Background spectra were collected on CNC-TPU cast on the ZnSe ATR crystal before D_2O exposure. Tygon tubing was then connected to the inlet and outlet of the gateway ATR flow cell and filled with 10 ml of D_2O to create a reservoir such that the top surface of the CNC-TPU would remain saturated with D_2O throughout the experiment. Dynamic ATR-FT-IR spectra were collected every 48 s over a period of 12 h from 4000-1000 cm^{-1} with a resolution of 0.482 cm^{-1}. D_2O diffusion was correlated to the rate of change of absorbance

in the peak range of 2200-2760 cm^{-1}. The D_2O peak was deconvoluted into five hydrogen bonding peaks[27] which were analyzed for CNC-TPU films ranging in CNC concentration from 0 - 15 wt %.

4.4 Results and Discussion

4.4.1 Mechanical Performance

We explored the capabilities of CNCs to reinforce TPU and introduce mechanical adaptivity in response to water exposure through transient DMA characterization of CNC-TPU films under controlled exposure to a humid environment. The storage modulus as a function of H_2O exposure was obtained while measuring both the equilibrium dry and wet moduli in the same experiment through careful delivery of humid air (80% RH) to the CNC-TPU films during continuous characterization at 1 Hz and 0.01 % strain. Humidity-controlled DMA (as opposed to submersion DMA) was selected to allow direct comparisons to our measurements of water diffusion from TGA-SA experiments which were collected in a humid chamber at a maximum of 80% RH. The mechanical response of CNC-TPU films ranging in CNC loadings from 0-15 wt% is detailed in Figure 4-1. The time axis is shifted such that $t = 0$ corresponds to the onset of humid air exposure (RH > 25%). Accordingly, times $t \leq 0$ correspond to the dry state modulus of the CNC-TPU film and the wet state modulus can be observed near the conclusion of the experiment.

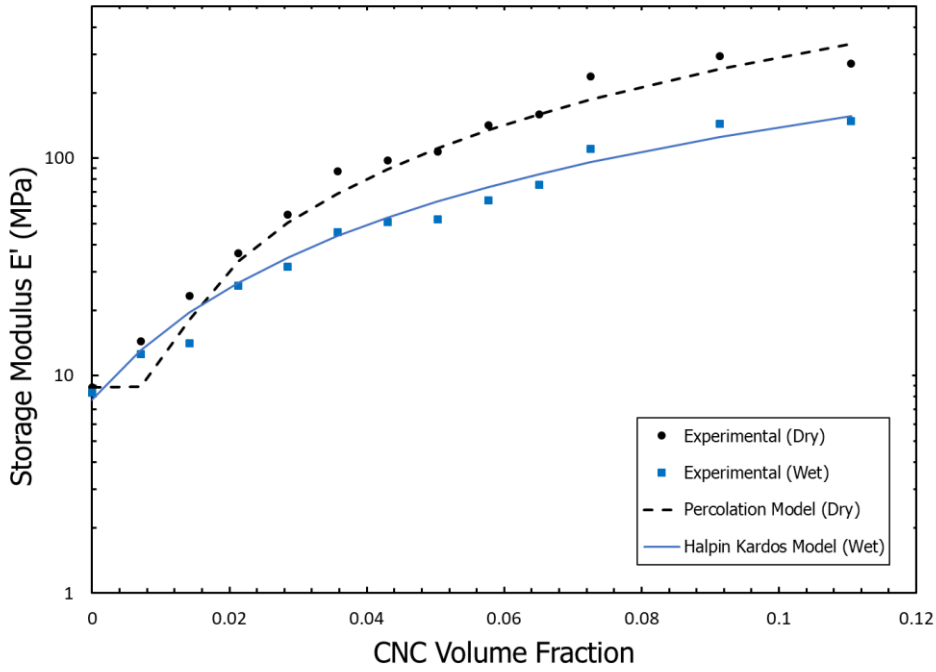

(a)

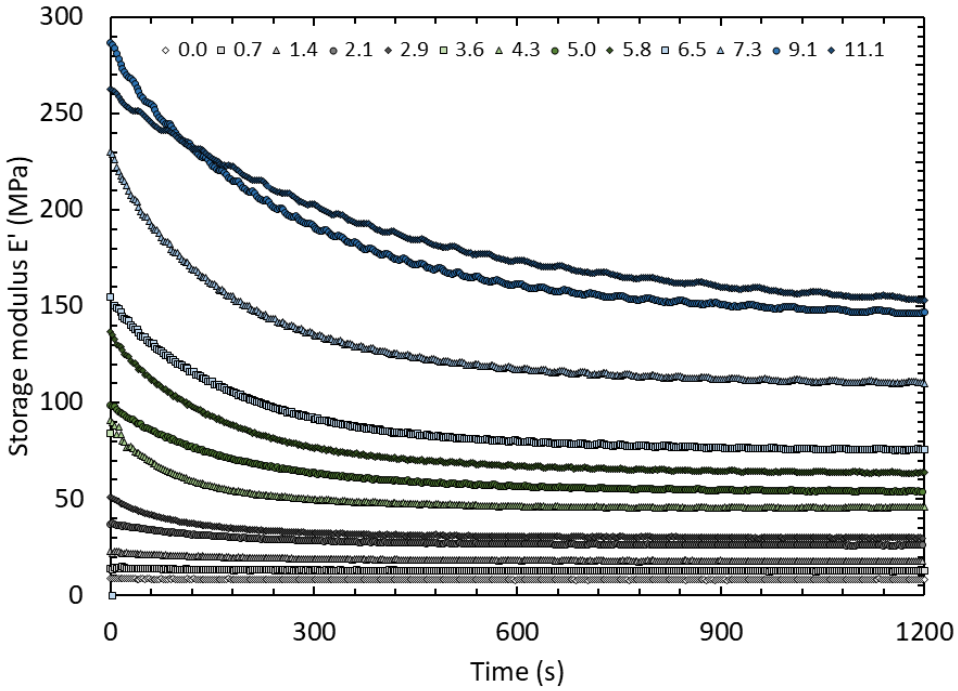

(b)

Figure 4-1. (a) Mechanical model fits to experimental data. Percolation model fit (dotted line) is fit to the experimental dry data (o) and Halpin Kardos model (solid line) is fit to the experimental wet data (x). (b) Swelling corrected storage modulus of CNC-TPU films as a function of

normalized time and CNC concentration from 0-15 wt %. CNC concentration increases from bottom to top. Initially dry samples were exposed to 80% RH at t = 0 marking the onset of a decrease in storage modulus.

The dry and wet state storage moduli increased as a function of CNC as well as the delta between the two moduli states, Figure 4-1a. Immediately upon the introduction of moisture, Figure 4-1b, the storage modulus rapidly decreases in all samples containing CNCs until a stable wet state storage modulus is obtained. In the pure TPU sample, however, moisture did not soften the material. This suggests that plasticization is not the cause of the softening mechanism. Rather, the experimentally observed softening is introduced as a result of the incorporation of a CNC networks within the polymer matrix as reported in other CNC-polymer systems.[2, 17]

The dry and wet state moduli can be further analyzed through implementation of a percolation[28, 29] and Halpin-Kardos[20] models, respectively. The critical concentration required for percolation, v_r^*, identifies the filler density above which a percolating network is developed based on geometric principles and is given by Equation (1)

$$v_r^* = 0.7/A \tag{1}$$

, where A is the aspect ratio which is taken to be 56.6 following atomic force microscopy measurements of the CNCs used in this study. This results in the percolation threshold of 1.2 vol %. While CNCs commonly exhibit a size distribution as a function of the cellulose source[30, 31] and hydrolysis conditions[32] resulting in a range of aspect ratios, the value calculated in Equation (1) serves as a good approximation for the critical concentration required for the development of a percolating network of CNCs. The percolation model is given by,

$$E_C' = \frac{(1 - 2\psi + \psi v_R)E_S'E_R' + (1 - v_R)\psi {E_R'}^2}{(1 - v_R)E_R' + (v_R - \psi)E_S'} \quad (2)$$

$$\psi = v_r \left(\frac{v_r - v_r^*}{1 - v_r^*}\right)^b \quad (3)$$

where E_c', E_s', and E_r' are the elastic moduli of the composite, matrix, and filler, respectively. The effect of the percolating network is dependent on the volume fraction of the filler, v_r, and is described by the fraction of filler which participates in the network, ψ. Finally, the critical percolation exponent, b, is 0.4 for 3D networks.[33, 34] As illustrated in Figure 4-1a, the percolation model, Equations (2) and (3), best fit the dry state mechanical properties as it accounts for the intermolecular bonds which form a percolating network.

The Halpin-Kardos model, which does not account for intermolecular bonds, is representative of the CNC composite in the wet state in which the water molecules have disrupted the percolating network structure. The parameters for the percolation and Halpin-Kardos models can be found in Table S4-1 and Table S4-2. The agreement of the dry state storage modulus, E'_{dry}, with the percolation model suggests that the CNCs are adequately dispersed and capable of forming an interconnected percolating network. Additionally, the wet state storage modulus, E'_{wet}, is effectively modeled with the Halpin-Kardos approach, corroborating the decoupling and weakening of the CNC network such that the CNCs are no longer interacting between particles post-water absorption.

Further, it is possible to control a wide range of moduli in between the initial and final states by governing the moisture content, as evidenced by the time-dependent decrease in storage moduli which is correlated to diffusive moisture uptake, Figure 4-1b. In this timeframe, the outer edges of the film are inactivated first as water infiltrates from the boundaries of the film.

Samples with greater CNC content respond quicker to the external stimulus noted by the significant increase in the magnitude of the negative slope in storage modulus as a function of time upon the introduction of humid air ($t = 0$). The decrease in storage modulus as a function of time illustrates a series of partial network disengagements where intermediate stages no longer allow CNCs to provide their full reinforcement. Diffusing water will have a higher probability of finding an inter-CNC hydrogen bond to disrupt in samples with a greater CNC concentration, therefore these disengagements will occur faster and to a greater extent. Further, each hydrogen bond replacement results in a greater loss in storage modulus as the reinforcement provided by CNCs is greatly enhanced at higher concentrations. Cumulatively, these interactions describe the softening performance as a function of CNC loading. We, later, explore the diffusive transport of water via TGA-SA to elucidate the mechanism of water transport and understand its role in mechanical actuation.

4.4.2 Bulk Diffusive Transport

Characterization of water transport into CNC-TPU films was implemented with TGA and TGA-SA to establish the equilibrium water uptake and water diffusivity respectively. Sulfuric acid-hydrolyzed CNCs, as used in this study, have a negative surface charge and are hydrophilic.[35] Accordingly, it is hypothesized that the addition of CNCs in the TPU matrix will facilitate water transport into the films. Measurement of the equilibrium water uptake, Figure 4-2a, after soaking in DI H_2O for 48 h clearly indicates that the incorporation of CNCs enables increased water absorption. The increased water uptake in films with high CNC content may very well contribute to the increased rate of softening as more water would foster competition over more interparticle hydrogen bonds.

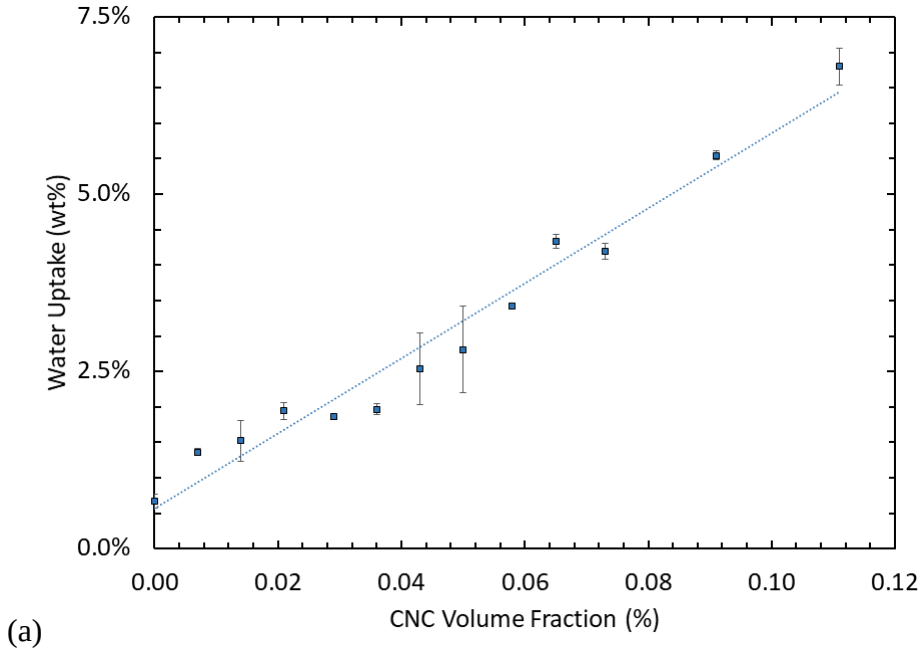

(a)

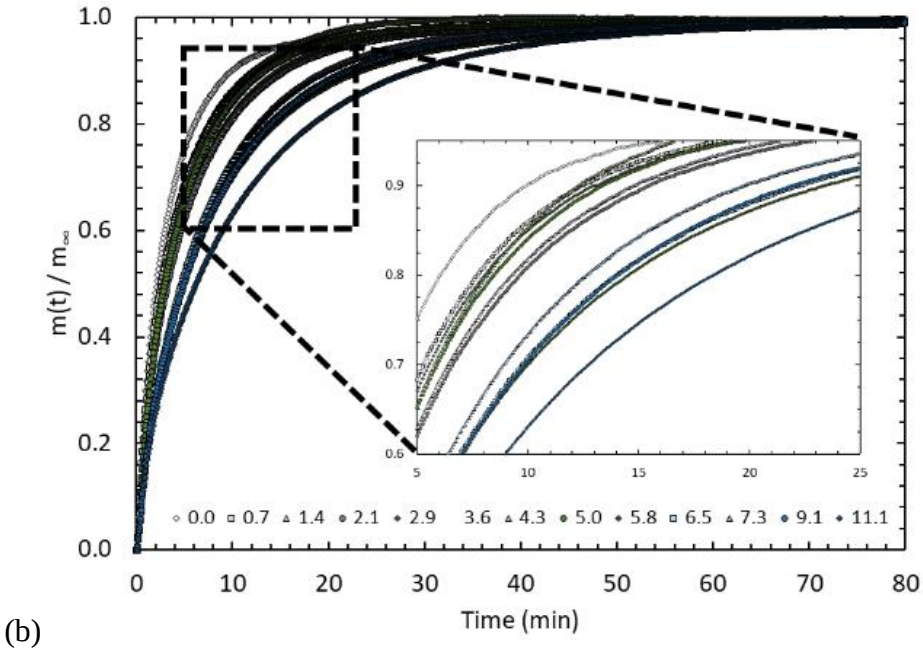

(b)

Figure 4-2. (a) Equilibrium water uptake as a function of CNC concentration measured by isothermal TGA at 115 °C after soaking in DI H_2O for 48 h. (b) Normalized mass uptake curves from TGA-SA at 80 % RH for CNC-TPU films as a function of time and CNC concentration from 0-15 wt % CNC. As CNC concentration increases, the slope of the curves decreases and is seen shifting to longer diffusion times, indicating a slower diffusivity.

The dynamics of this process was studied with TGA-SA where water uptake in CNC-TPU films was measured as a function of time when exposed to 80% RH. The humidity level was chosen to match the limitations of the DMA humidity accessory and to provide a direct comparison between softening and water uptake. The resulting normalized mass uptake, illustrated in Figure 4-2b, reveals a decrease in slope with increasing CNC content. This suggests water is absorbed at a slower rate as CNC concentration is increased, despite having greater equilibrium water uptake.

Several mechanisms have been hypothesized to explain the complex diffusion characteristics but they fall short of fully explaining the often superficially contradictory data. Some propose that CNCs comprise impenetrable regions which causes water to divert its course to continue motion, thus creating a tortuous path which lengthens the effective molecular diffusion distance thereby impeding diffusion.[36, 37] In contrast, the hydrophilic chemistry on the surface of CNCs may facilitate water transport in an otherwise hydrophobic system.[17] The CNC surface charge density may have a critical role on the rate of water diffusion as increased CNC surface charge density has been shown to increase equilibrium water uptake as well as increase the rate of water diffusion into CNC and poly(vinyl acetate) nanocomposite films.[2] Alternatively, CNCs may develop hydrogen bonds with solvent molecules which both act to draw water in, but additionally, maintain a hold on these molecules either preventing or hindering further diffusion.

In an effort to bridge the gap between DMA and TGA measurements, an extended analysis of the diffusion profile is required to fully evaluate the water transport mechanism. The nature of polymeric systems to stray from Fickian diffusive behavior, represented in Equation (4), and present anomalous diffusion characteristics due to additional interactions and structural constraints on the motion of solvent molecules presents additional complexities to be considered.[38]

$$D\frac{\partial^2 c}{\partial z^2} = \frac{dc}{dt} \tag{4}$$

Where, D, is the diffusivity, c, is the water concentration, z, is the 1-dimensional spatial coordinate, and t, is time. Equation (4) can be analytically represented as Equation (5),

$$\frac{m}{m_\infty} = 1 - \frac{8}{\pi^2}\sum_{n=0}^{\infty}\frac{1}{(2n+1)^2}e^{-\frac{(2n+1)^2\pi^2 Dt}{\delta^2}} \tag{5}$$

where, $\frac{m}{m_\infty}$ is the mass at time t normalized to the equilibrium mass uptake, m_∞, and δ is the diffusion length. While some CNC and polymer nanocomposites can be described by Fickian diffusion,[24, 37] the potential for strong hydrogen bonding with water may significantly impact solvent transport. We followed the hindered diffusion model developed by Carter and Kibler, Equations (6) and (7) to glean the mechanism of water transport in CNC-TPU nanocomposites and evaluate the relationship between diffusivity, D and CNC concentration.[38] Carter and Kibler modified Fick's 2nd law such that the time-dependent term is split into two components, *n* and *N*, representing the mobile and bound water concentrations respectively. Thus, the effects of hydrogen bonding between water and CNCs diffusing in the mobile phase can be isolated and the relative influence of each component can be evaluated.

$$D\frac{\partial^2 n}{\partial z^2} = \frac{\partial n}{\partial t} + \frac{\partial N}{\partial t} \tag{6}$$

$$\frac{\partial N}{\partial t} = \gamma n - \beta N \tag{7}$$

Bound and mobile water molecules are allowed to transition to the opposite hydrogen bonding state through γ and β which represent the probability of a mobile water molecules to become bound and the probability of bound water molecules to be released to the mobile phase, respectively. This contribution represents the ability of hydrogen bonds to reconnect and transfer

as a mobile water molecule replaces a bound water molecule on the surface of a CNC. An analytical solution for the fractional water uptake as a function of time was provided by Carter and Kibler are given in Equations (8), (9), and (10).[38]

$$\frac{m_t}{m_\infty} = 1 - \frac{8}{\pi^2}\sum_{l=1}^{\infty(odd)} \frac{r_l^+ e^{-r_l^- t} - r_l^- e^{-r_l^+ t}}{l^2(r_l^+ - r_l^-)} + \frac{8}{\pi^2}\frac{\kappa\beta}{\gamma+\beta}\sum_{l=1}^{\infty(odd)} \frac{e^{-r_l^- t} - e^{-r_l^+ t}}{r_l^+ - r_l^-} \tag{8}$$

$$r_l^{\pm} = \frac{1}{2}\left[(\kappa l^2 + \gamma + \beta) \pm \sqrt{(\kappa l^2 + \gamma + \beta)^2 - 4\kappa\beta l^2}\right] \tag{9}$$

$$\kappa = \frac{\pi^2 D_\gamma}{(2\delta)^2} \tag{10}$$

Analysis of diffusion coefficients evaluated from the Fickian and hindered diffusion models are illustrated in Figure 4-3.

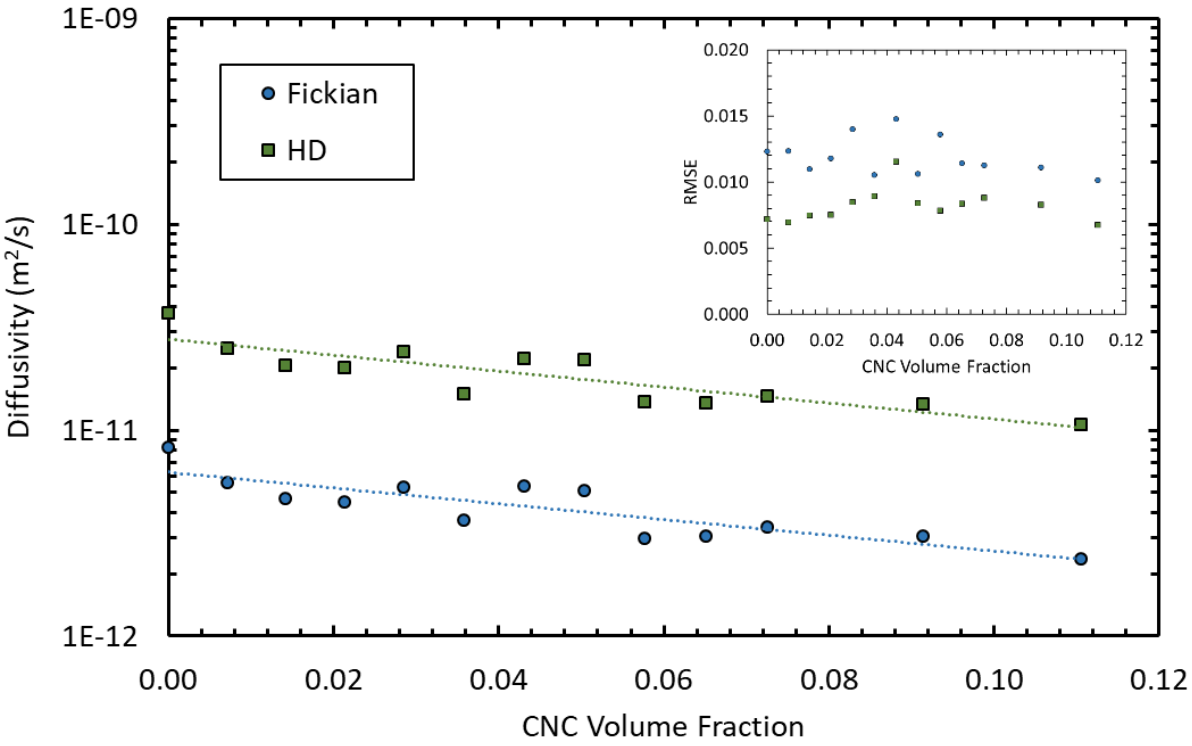

Figure 4-3. Diffusivity for water diffusing through CNC-TPU nanocomposites as a function of CNC concentration fit with Fickian (●) and Hindered diffusion (■) models. Dashed lines represent exponential fits for each diffusion model as a function of filler loading. Inset shows the root-mean-squared error (RMSE) of the model fits and highlights the improved accuracy of the Hindered diffusion model.

The diffusivities calculated from both models indicate that the rate of water diffusion decreases as more CNCs are incorporated into the matrix. While, a comparison of the two models reveals a deviation in the hindered diffusion model by a factor of approximately 4.5 from the Fickian prediction, the same trends with respect to CNC concentration are maintained. Further, the hindered diffusion model afforded a better fit to the data as affirmed by the reduced error associated with the model as illustrated in Figure 4-3. This can be attributed to the hindered diffusion model's capability to capture the small amount of anomalous diffusion behavior that is observed at extended times in Figure 4-2b. These non-Fickian characteristics can be attributed to water molecules being hindered in their transport when forming hydrogen bonds with CNCs, swelling of the matrix, as well as increased mobility of CNCs as inter-CNC hydrogen bonds are displaced. In totality, the increased ionic strength generated by increasing filler concentration leads to increased hydrophilicity and mass uptake as reported by Dagnon et al.[2] However, since the CNCs used in this work had the same surface charge density, these interactions cannot explain the decrease in diffusivity with higher CNC loadings. In fact, the γ and β parameters for the hindered diffusion model remained constant with increasing CNC concentration, Figure S4-7, corroborating the similar surface charge densities found in all films. Therefore, we can exclude molecular interactions from contributing to the observed decrease in diffusivity and focus on the impact of swelling on the observed behavior.

Swelling is perhaps the most commonly discussed factor contributing to anomalous diffusion among the literature and several exhaustive models based on polymer free volume have been developed to explain this phenomenon.[39-44] Here, the simplest approach is considered, Equation (11), which accounts for the change polymer free volume during swelling as a modification to the diffusivity, D, based on the diffusivity at equilibrium swelling, D_{eq}.[45]

$$D = D_{eq} e^{\alpha \phi^{\beta}} \tag{11}$$

Where ϕ is the volume fraction of polymer, α has been shown to be correlated to the size of solvent molecules,[41] and β is taken to be unity.[45] Here, we substitute ϕ with the volume fraction of CNCs as they provide the hydrophilicity responsible for increased mass uptake. The equilibrium diffusivity as predicted by the Fickian and hindered diffusion models was found to be $6.3\ x\ 10^{-12}\ \frac{m^2}{s}$ and $2.8\ x\ 10^{-11}\ \frac{m^2}{s}$, respectively. Further, the negative α parameters, -8.8 and -8.9, respectively, signify an exponential decay in diffusivity suggesting that swelling increases with increasing CNC concentration resulting in slower apparent diffusivities. We will later highlight the significance of accounting for swelling in the mechanical data.

4.4.3 Local Diffusive Transport

To supplement the bulk diffusive transport measured in Figure 4-2, further investigation into the role of hydrogen bonding during water diffusion was evaluated through *in-situ* ATR-FTIR. The migration of D_2O through CNC-TPU films as a function of time was monitored through changes in the absorbance between 2700-2200 cm^{-1}.[46] D_2O was selected to transition the spectral observation window from 3700-2900 cm^{-1} to 2700-2200 cm^{-1} such that the absorbance of the diffusant did not overlap with any secondary peaks from the chemical structure of either CNCs or TPU.[47] This shift, as a result of the isotopic substitution of hydrogen atoms, can be quantified such that the spectra of D_2O resembles a shifted H_2O spectra where $\nu_{D_2O} =$

$0.742\nu_{H_2O}$, where ν represents the vibrational frequency. Additionally, the self-diffusion coefficient for D_2O is approximately 80% lower than H_2O, owing to the greater moment of inertia of D_2O, therefore a direct comparison of diffusivities from TGA-SA cannot be made. However, the broad range of spectroscopic information provided by ATR-FTIR provides insight into various hydrogen bonding states of D_2O that can be attributed to the behavior observed in Figure 4-2.

A reservoir of D_2O was maintained above the thin film such that diffusion took place predominantly in one dimension through the bulk of the film where the ATR-FTIR spectra was collected in the bottom 1.25 μm of the film, based on the refractive indices of TPU and the ZnSe crystal.[48] Due to the change in boundary conditions from a symmetric water loading on both sides of the film in the TGA and DMA experiments to D_2O loading on only one side of the film, the spectra were recorded over a period of 12 h as opposed to 2.5 h for the previous experiments. A typical ATR-FTIR spectra is shown in Figure 4-4a for a 4 wt % CNC-TPU film showing increasing D_2O absorbance at 2503 cm^{-1} as a function of time. Positive peaks indicate an increase in concentration of functional groups vibrating at a given wavenumber, most prominently the peaks at 2465 and 1221 cm^{-1} are observed to increase and are associated with O-D vibrations and D-O-D bending modes respectively. Negative peaks represent a decrease in the concentration of a given functional group within the 1.25 μm penetration depth. These are associated with vibrations corresponding to CNCs and TPU. The introduction of D_2O leads to swelling of the TPU matrix within examined region and results in a decrease in TPU density locally. The TPU swelling may concurrently push CNCs outside the observation window, leading to decreases in the absorbance of the functional groups representing these materials.[49]

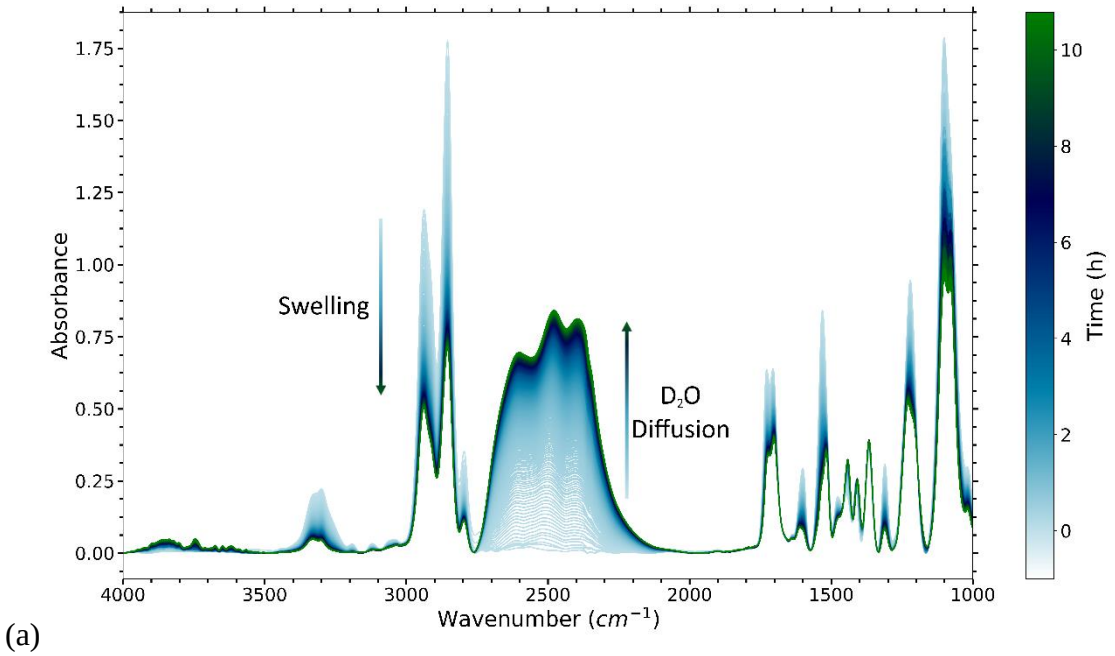

(a)

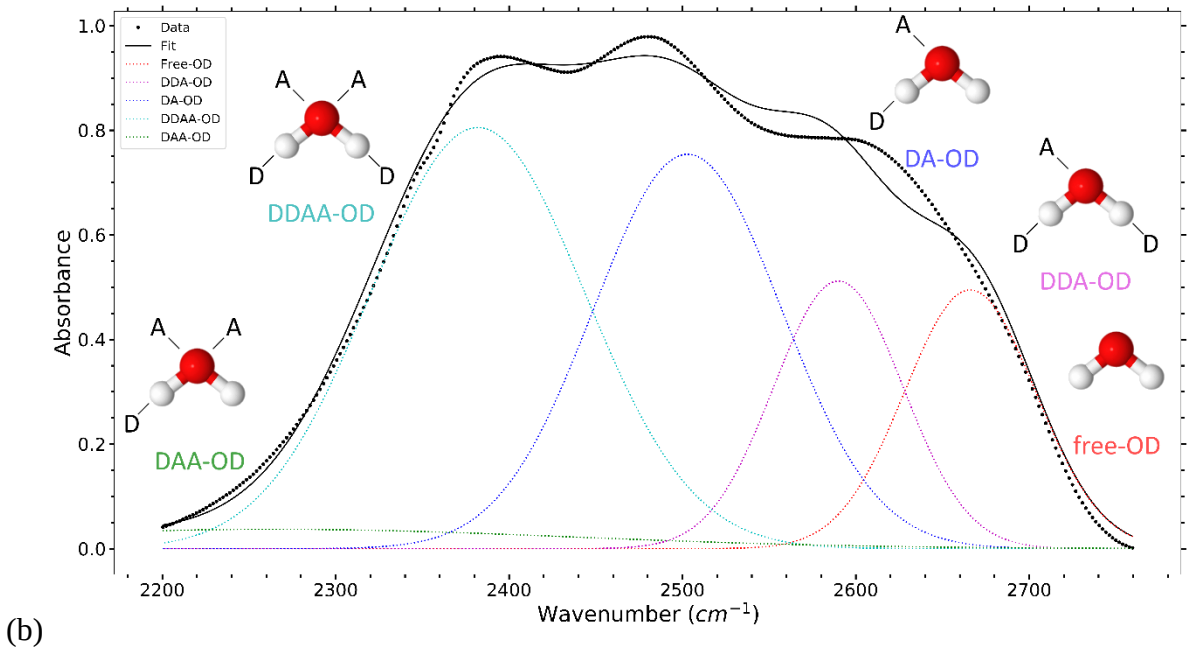

(b)

Figure 4-4. (a) ATR-FTIR absorbance spectra for D_2O diffusing into a 4 wt% CNC-TPU film over 12 h. Spectra were collected every 48s and its time evolution is represented by a change in color from light blue at short times to green near the end of the characterization period. ATR-FTIR background was collected on the dry 4 wt % CNC-TPU film before exposure to D_2O. (b)

Deconvolution of a 1 wt% CNC-TPU FTIR-ATR spectra from 2200-2760 cm-1 into five hydrogen bonding modes at $t = t_\infty$.

The D_2O peaks ranging from 2760-2200 cm^{-1} were deconvoluted with Gaussian distributions to isolate five primary hydrogen bonding states of D_2O, Figure 4-4b. D_2O can accept, A, and donate, D, hydrogen bonds, designated as DAA-OD, DDAA-OD, DA-OD, DDA-OD and free-OD, which are associated with vibrations at 2265, 2382, 2503, 2590, 2666 cm^{-1}, respectively.[27, 50] The fraction of D_2O molecules participating in hydrogen bonds, β, was calculated from Equation (12) as a function of time,

$$\beta = \frac{1 - A_{free-OD}}{\sum_{i=1}^{2}\sum_{j=1}^{2} D_i A_j - OD} \tag{12}$$

where $D_i A_j - OD$ is the peak absorbance of a hydrogen bonding mode with i donated hydrogen bonds and j accepted hydrogen bonds. The hydrogen bond fraction for D_2O alone was 0.86 whereas the fraction was initially high for most CNC concentrations, but rapidly reached an equilibrium value of 0.80, with respect to the total diffusion time. The fraction of hydrogen bonds interacting with CNCs can then be expressed as the ratio of these values to achieve a CNC hydrogen bond fraction of 0.92. Since the approximate maximal hydrogen bond densities for CNCs and TPU are 2.4 and 0.3 H-bonds nm^{-1}, respectively and the hard segments of TPU sterically hinder water from participating in hydrogen bonds, we assume hydrogen bonds are primarily occurring between CNCs and D_2O. Thus, the equilibrium value was attributed to the wet state hydrogen bonding fraction which is correlated with the disruption of the percolating network of CNCs.

Finally, a correction is required to adjust the experimentally characterized hydrogen bonding fraction as it overestimates the CNC hydrogen bonding when inter-CNC bonds are disrupted and

new hydrogen bonds are formed between CNCs and water. As D_2O molecules have five available hydrogen bonding modes[27] and the surface SO_3^- and OH functional groups of CNCs have only three hydrogen bonding modes accessible to water, a correction factor of $\frac{3}{5}$ is required to explain the CNC hydrogen bonding state. Thus, the experimentally observed hydrogen bonds participating with CNCs is 0.55.

4.4.4 Relationship between Diffusion and Mechanical Performance

Finally, a relationship between the diffusion of water into CNC-TPU films and their mechanical performance in terms of storage modulus can be obtained. We modify the filler contributions to the percolating network, ψ, in Equation (3) (5)to account for the breaking of hydrogen bonds between CNCs as water diffuses through the network. To that end, we introduce the term $\beta(t)$ to represent the fraction of formed hydrogen bonds between CNCs and replace Equation (3) with Equation (13).

$$\psi = \beta(t) v_r \left(\frac{v_r - v_r^*}{1 - v_r^*}\right)^b \tag{13}$$

A cursory application of Equations (2) and (13) to the mechanical data collected in Figure 4-1, where $\beta(t)$ is taken as the constant values of 1 and 0.5 for the dry and wet states, respectively, is illustrated in Figure 4-5. The optimized β values were in agreement with the experimental prediction of 0.55 and the model adequately fit both the dry and wet state moduli above the critical percolation concentration. The $\beta(t)$ parameter can be used to describe the change in modulus as a function of filler concentration for both equilibrium states of CNC-TPU films. We therefore, highlight the power of this modification to explain the mechanical adaptivity of CNC-TPU and other mechanically responsive polymer nanocomposites with a single unifying formulation. Consolidation of the two primary modeling tools from literature into

a single mechanical model will enable a greater understanding of the underlying phenomena associated with the deactivation of the percolating network in these materials.

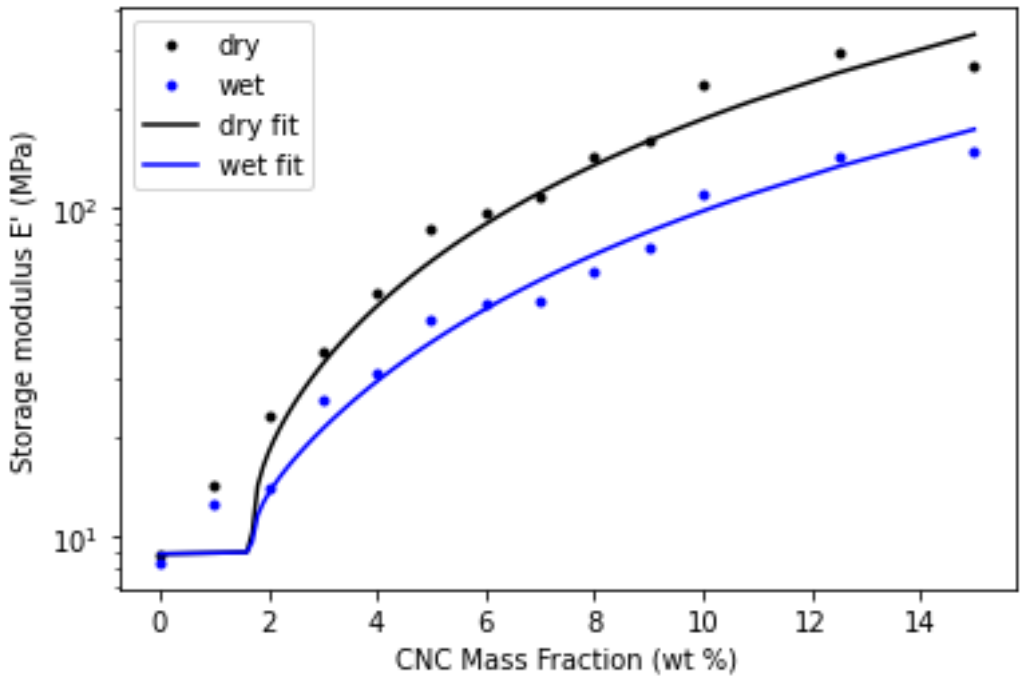

Figure 4-5. Percolation model adapted for dry and wet state modulus predictions. v_r^* = 0.012, beta = 1, 0.5 as a function of CNC mass fraction highlighting that the included beta term can be used to capture both dry and wet state moduli.

Additionally, this new formulation enables the prediction of the time dependence of the storage modulus during water uptake as well. Full encapsulation of the mechanical softening is provided through a time-dependent $\beta(t)$ which is expressed as

$$\beta(t) = \beta_{dry} - \beta_{wet}\frac{m(t)}{m_\infty} \tag{14}$$

, where β_{dry} and β_{wet} are dimensionless quantities representing the equilibrium fraction of hydrogen bonds between filler particles in the dry and wet state, respectively. Further, the equilibrium β values describe the degree of softening. The rate of switching is captured by the

$\frac{m(t)}{m_\infty}$ term which represents the solvent mass uptake as a function of time normalized to the equilibrium mass uptake. The diffusion term can be evaluated from an experimental dataset such as Figure 4-2 or any suitable mass transport derivation, including the Fickian and hindered diffusion models from Equations (5) and (8)-(10) which is demonstrated in Figure 4-6.

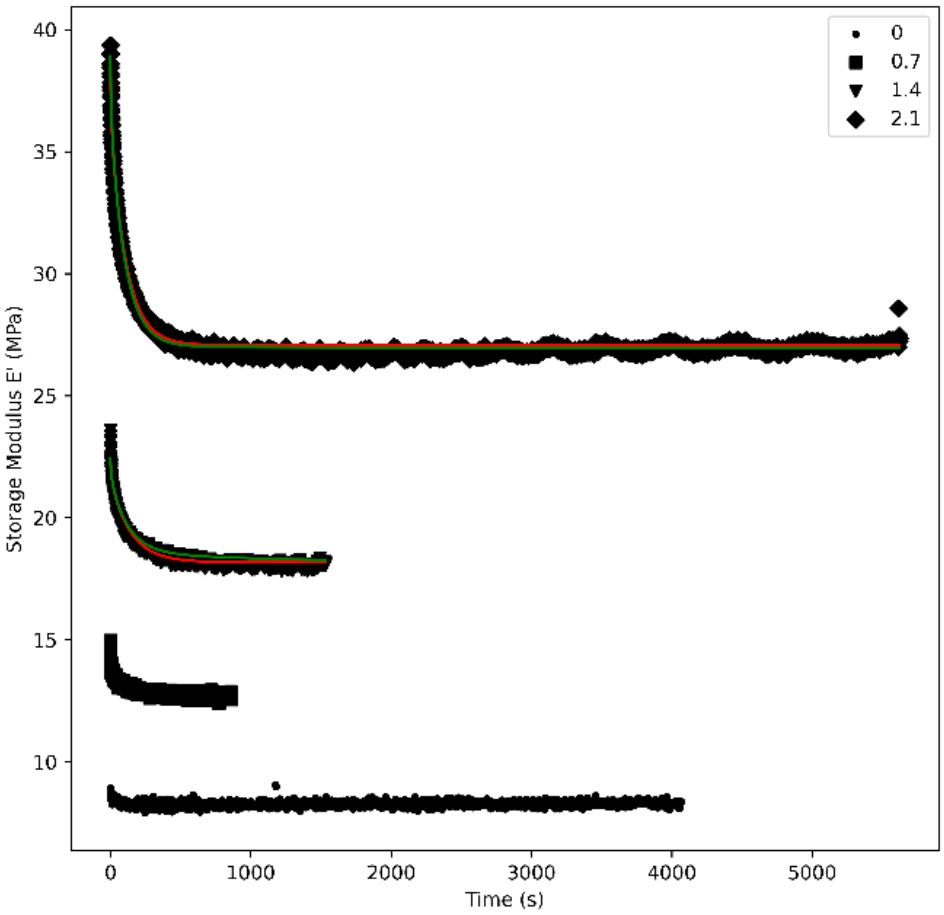

(a)

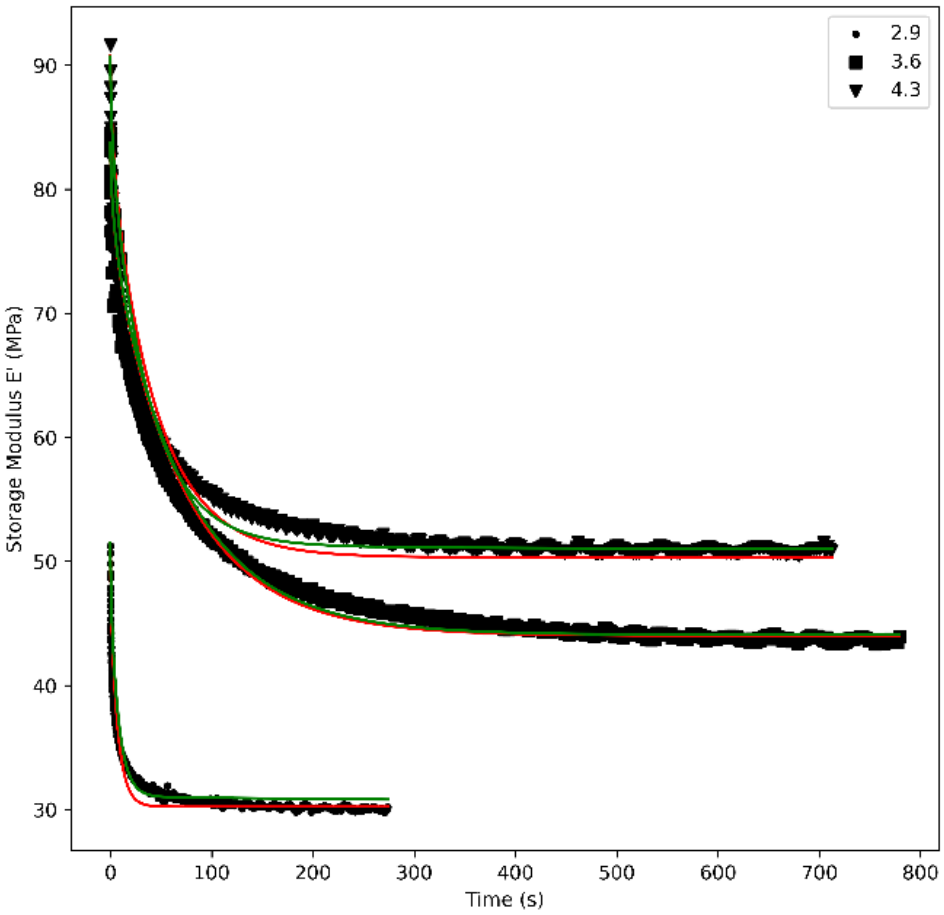
2.9
3.6
4.3
Storage Modulus E' (MPa)
Time (s)
90
80
70
60
50
40
30
0
100
200
300
400
500
600
700
800

(b)

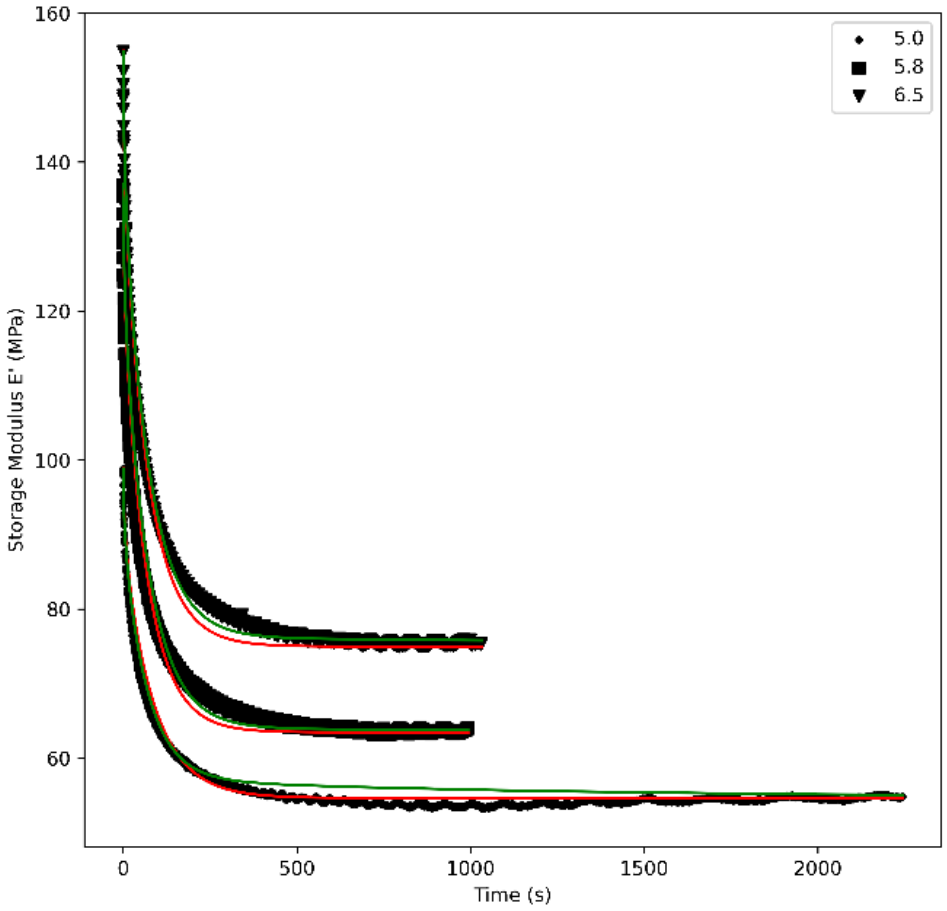
160
140
120
100
80
60
Storage Modulus E' (MPa)
0
500
1000
1500
2000
Time (s)
5.0
5.8
6.5

(c)

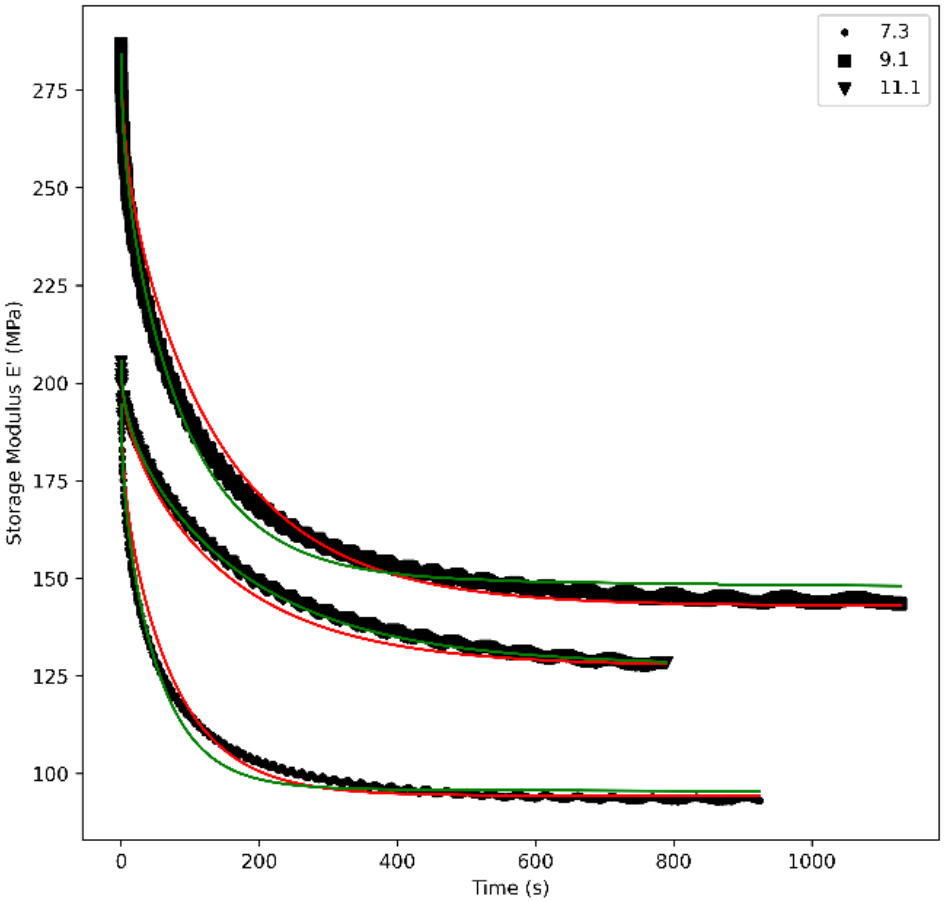
7.3
9.1
11.1
Storage Modulus E' (MPa)
275
250
225
200
175
150
125
100
0
200
400
600
800
1000
Time (s)

(d)

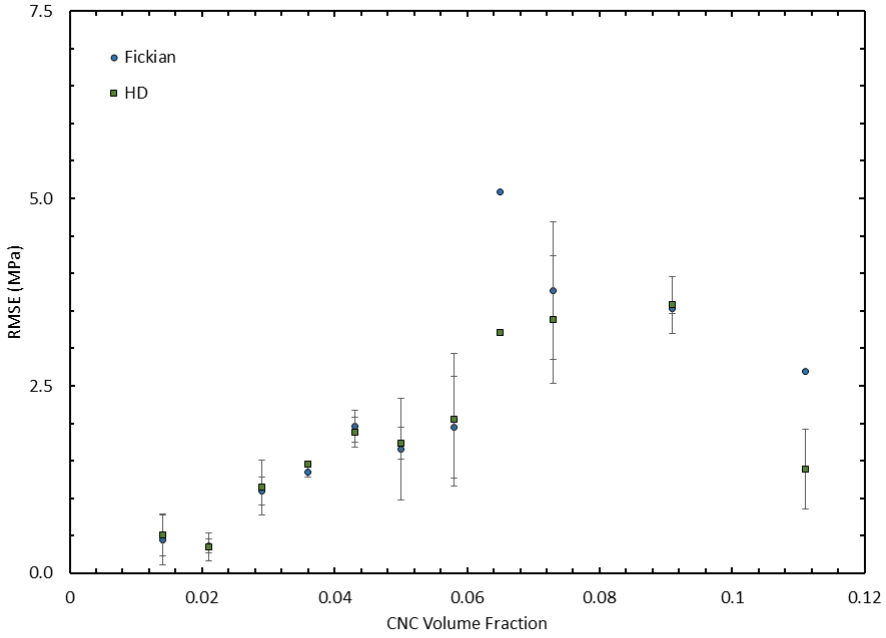

(e)

Figure 4-6. (a-d) Modified percolation model fits with Fickian (red) and Hindered diffusion (green) mass uptake profiles as a function of time and CNC volume fraction. (e) Root-mean-squared error of the preceding percolation models as a function of CNC volume fraction.

Limitations of the model to predict the modulus response in films with filler loadings below the critical percolation threshold is depicted in Figure 4-6a, where the TPU and 1 wt % CNC-TPU films were not effectively modeled. Therefore, the small amount of reinforcement provided by CNCs at low concentrations was not captured. In contrast to the mass uptake which was best fit with the hindered diffusion model, both percolation model implementations predicted the softening behavior well, Figure 4-6e. It was observed that the error generally increased with CNC concentration, however, the predicted diffusivities remained remarkably constant. The average diffusivities predicted by the modified percolation models, 3.3×10^{-11} and 1.2×10^{-10} m^2 s^{-1}, for the Fickian and hindered diffusion implementations respectively, were in agreement with the equilibrium diffusivity predicted by the hindered diffusion model as it was

applied to water uptake, 2.8 x 10^{-11} m^2 s^{-1}. This supports our conclusion that the decrease in the diffusivity predicted by the mass transport models as a function of CNC concentration, Figure 4-3, is a result of swelling of the matrix during water uptake as the CNC volume fraction used in the percolation models presented in Figure 4-6 were corrected for swelling at each time step.

4.4.5 Conclusion

We explored the mechanical adaptivity of CNC-TPU nanocomposites in response to water uptake through a comprehensive mass transport analysis coupled with traditional mechanical modeling. Emphasis was placed on resolving controversial diffusivity analyses of similar nanocomposites reported in literature.[2, 17, 36, 37] Here we found compelling evidence to support increasing charge and hydrophilicity will increase the diffusivity as reported by Dagnon et al.[2] Additionally, samples with the same charge density will have an apparent decrease in diffusivity as a function of CNC loading due to polymer swelling, despite the increased total water uptake observed experimentally.

Additionally, we extended the commonly implemented percolation model to describe both the dry and wet state storage moduli as a function of filler loading and introduced a time-dependent formulation to capture the full breadth of mechanical switching observed experimentally and is general as to apply to many other CNC-polymer nanocomposites. This unifying model will provide detailed insight into the dynamics of mechanical adaptivity for smart material development.

References

1. Montero de Espinosa, L.; Meesorn, W.; Moatsou, D.; Weder, C., Bioinspired Polymer Systems with Stimuli-Responsive Mechanical Properties. *Chemical Reviews* **2017,** *117* (20), 12851-12892.
2. Dagnon, K. L.; Way, A. E.; Carson, S. O.; Silva, J.; Maia, J.; Rowan, S. J., Controlling the rate of water-induced switching in mechanically dynamic cellulose nanocrystal composites. *Macromolecules* **2013,** *46* (20), 8203-8212.

3. Dagnon, K. L.; Shanmuganathan, K.; Weder, C.; Rowan, S. J., Water-triggered modulus changes of cellulose nanofiber nanocomposites with hydrophobic polymer matrices. *Macromolecules* **2012,** *45* (11), 4707-4715.
4. Rusli, R.; Shanmuganathan, K.; Rowan, S. J.; Weder, C.; Eichhorn, S. J., Stress-transfer in anisotropic and environmentally adaptive cellulose whisker nanocomposites. *Biomacromolecules* **2010,** *11* (3), 762-768.
5. Tian, M.; Zhen, X.; Wang, Z.; Zou, H.; Zhang, L.; Ning, N., Bioderived Rubber–Cellulose Nanocrystal Composites with Tunable Water-Responsive Adaptive Mechanical Behavior. *ACS Applied Materials & Interfaces* **2017,** *9* (7), 6482-6487.
6. Wu, Q.; Henriksson, M.; Liu, X.; Berglund, L. A., A high strength nanocomposite based on microcrystalline cellulose and polyurethane. *Biomacromolecules* **2007,** *8* (12), 3687-3692.
7. Tian, M.; Zhen, X.; Wang, Z.; Zou, H.; Zhang, L.; Ning, N., Bioderived Rubber-Cellulose Nanocrystal Composites with Tunable Water-Responsive Adaptive Mechanical Behavior. *ACS Appl Mater Interfaces* **2017,** *9* (7), 6482-6487.
8. Annamalai, P. K.; Dagnon, K. L.; Monemian, S.; Foster, E. J.; Rowan, S. J.; Weder, C., Water-responsive mechanically adaptive nanocomposites based on styrene-butadiene rubber and cellulose nanocrystals--processing matters. *ACS Appl Mater Interfaces* **2014,** *6* (2), 967-76.
9. Capadona, J. R.; Shanmuganathan, K.; Tyler, D. J.; Rowan, S. J.; Weder, C., Stimuli-responsive polymer nanocomposites inspired by the sea cucumber dermis. *Science* **2008,** *319* (5868), 1370-4.
10. Shanmuganathan, K.; Capadona, J. R.; Rowan, S. J.; Weder, C., Stimuli-responsive mechanically adaptive polymer nanocomposites. *ACS Appl Mater Interfaces* **2010,** *2* (1), 165-74.
11. Meesorn, W.; Shirole, A.; Vanhecke, D.; de Espinosa, L. M.; Weder, C., A Simple and Versatile Strategy To Improve the Mechanical Properties of Polymer Nanocomposites with Cellulose Nanocrystals. *Macromolecules* **2017,** *50* (6), 2364-2374.
12. Favier, V.; Cavaille, J. Y.; Canova, G. R.; Shrivastava, S. C., Mechanical percolation in cellulose whisker nanocomposites. *Polymer Engineering & Science* **1997,** *37* (10), 1732-1739.
13. Fallon, J. J.; Kolb, B. Q.; Herwig, C. J.; Foster, E. J.; Bortner, M. J., Mechanically adaptive thermoplastic polyurethane/cellulose nanocrystal composites: Process-driven structure–property relationships. *Journal of Applied Polymer Science* **2018,** *0* (0), 46992.
14. Martínez-Sanz, M.; Lopez-Rubio, A.; Lagaron, J. M., Optimization of the Dispersion of Unmodified Bacterial Cellulose Nanowhiskers into Polylactide via Melt Compounding to Significantly Enhance Barrier and Mechanical Properties. *Biomacromolecules* **2012,** *13* (11), 3887-3899.
15. Auad, M. L.; Contos, V. S.; Nutt, S.; Aranguren, M. I.; Marcovich, N. E., Characterization of nanocellulose- reinforced shape memory polyurethanes. *Polymer International* **2008,** *57* (4), 651-659.
16. Urbina, L.; Alonso-Varona, A.; Saralegi, A.; Palomares, T.; Eceiza, A.; Corcuera, M. A.; Retegi, A., Hybrid and biocompatible cellulose/polyurethane nanocomposites with water-activated shape memory properties. *Carbohydr Polym* **2019,** *216*, 86-96.

17. Mendez, J.; Annamalai, P. K.; Eichhorn, S. J.; Rusli, R.; Rowan, S. J.; Foster, E. J.; Weder, C., Bioinspired Mechanically Adaptive Polymer Nanocomposites with Water-Activated Shape-Memory Effect. *Macromolecules* **2011,** *44* (17), 6827-6835.
18. Fallon, J. J.; Kolb, B. Q.; Herwig, C. J.; Foster, E. J.; Bortner, M. J., Mechanically adaptive thermoplastic polyurethane/cellulose nanocrystal composites: Process-driven structure-property relationships. *Journal of Applied Polymer Science* **2019,** *136* (4).
19. Nicharat, A.; Shirole, A.; Foster, E. J.; Weder, C., Thermally activated shape memory behavior of melt-mixed polyurethane/cellulose nanocrystal composites. *Journal of Applied Polymer Science* **2017,** *134* (27).
20. Halpin, J. C.; Kardos, J. L., Moduli of Crystalline Polymers Employing Composite Theory. *Journal of Applied Physics* **1972,** *43* (5), 2235-2241.
21. Ma, H.; Burger, C.; Hsiao, B. S.; Chu, B., Ultrafine Polysaccharide Nanofibrous Membranes for Water Purification. *Biomacromolecules* **2011,** *12* (4), 970-976.
22. Smith, E. D.; Hendren, K. D.; Haag, J. V.; Foster, E. J.; Martin, S. M., Functionalized Cellulose Nanocrystal Nanocomposite Membranes with Controlled Interfacial Transport for Improved Reverse Osmosis Performance. *Nanomaterials* **2019,** *9* (1), 125.
23. Mathew, A. P.; Gong, G.; Bjorngrim, N.; Wixe, D.; Oksman, K., Moisture absorption behavior and its impact on the mechanical properties of cellulose whiskers-based polyvinylacetate nanocomposites. *Polymer Engineering & Science* **2011,** *51* (11), 2136-2142.
24. Reid, M. S.; Kedzior, S. A.; Villalobos, M.; Cranston, E. D., Effect of Ionic Strength and Surface Charge Density on the Kinetics of Cellulose Nanocrystal Thin Film Swelling. *Langmuir* **2017,** *33* (30), 7403-7411.
25. Sutliff, B. P.; Das, A.; Youngblood, J.; Bortner, M. J., High shear capillary rheometry of cellulose nanocrystals for industrially relevant processing. *Carbohydr Polym* **2020,** *231*, 115735.
26. Foster, E. J.; Moon, R. J.; Agarwal, U. P.; Bortner, M. J.; Bras, J.; Camarero-Espinosa, S.; Chan, K. J.; Clift, M. J. D.; Cranston, E. D.; Eichhorn, S. J.; Fox, D. M.; Hamad, W. Y.; Heux, L.; Jean, B.; Korey, M.; Nieh, W.; Ong, K. J.; Reid, M. S.; Renneckar, S.; Roberts, R.; Shatkin, J. A.; Simonsen, J.; Stinson-Bagby, K.; Wanasekara, N.; Youngblood, J., Current characterization methods for cellulose nanomaterials. *Chemical Society Reviews* **2018,** *47* (8), 2609-2679.
27. Sun, Q.; Guo, Y., Vibrational sum frequency generation spectroscopy of the air/water interface. *Journal of Molecular Liquids* **2016,** *213*, 28-32.
28. Takayanagi, M.; Uemura, S.; Minami, S., Application of equivalent model method to dynamic rheo-optical properties of crystalline polymer. *Journal of Polymer Science Part C: Polymer Symposia* **1964,** *5* (1), 113-122.
29. Ouali, N.; Cavaillé, J.; Perez, J., Elastic, viscoelastic and plastic behavior of multiphase polymer blends. *Plastics, Rubber and Composites Processing Applications* **1991**, 55-60.
30. Habibi, Y.; Lucia, L. A.; Rojas, O. J., Cellulose nanocrystals: chemistry, self-assembly, and applications. *Chem Rev* **2010,** *110* (6), 3479-500.
31. Jonoobi, M.; Oladi, R.; Davoudpour, Y.; Oksman, K.; Dufresne, A.; Hamzeh, Y.; Davoodi, R., Different preparation methods and properties of nanostructured cellulose from various natural resources and residues: a review. *Cellulose* **2015,** *22* (2), 935-969.

32. Beck-Candanedo, S.; Roman, M.; Gray, D. G., Effect of reaction conditions on the properties and behavior of wood cellulose nanocrystal suspensions. *Biomacromolecules* **2005,** *6*, 1048-1054.
33. Favier, V.; Chanzy, H.; Cavaille, J. Y., Polymer Nanocomposites Reinforced by Cellulose Whiskers. *Macromolecules* **1995,** *28*, 6365-6367.
34. Favier, V.; Canova, G. R.; Cavaille, J. Y.; Chanzy, H.; Dufresne, A.; Gauthier, C., Nanocomposite Materials from Latex and Cellulose Whiskers. *Polymers for Advanced Technologies* **1995,** *6*, 351-355.
35. Foster, E. J.; Moon, R. J.; Agarwal, U.; Bortner, M. J.; Bras, J.; Camarero-Espinosa, S.; Chan, K. J.; Clift, M. J. D.; Cranston, E. D.; Eichorn, S.; Fox, D.; Hamad, W.; Heux, L.; Jean, B.; Korey, M.; Nieh, W.; Ong, K. J.; Reid, M. S.; Renneckar, S.; Roberts, R.; Shatkin, J. A.; Simonsen, J.; Stinson-Bagby, K.; Wanasekara, N.; Youngblood, J., Current characterization methods for cellulose nanomaterials. *Chemical Society Reviews* **2018,** *47*, 2609-2679.
36. Hood, M. A. Correlating the Structure and Properties of Highly Plastic Segmented Polyurethane nanocomposites. Drexel University, 2012.
37. Follain, N.; Belbekhouche, S.; Bras, J.; Siqueira, G.; Marais, S.; Dufresne, A., Water transport properties of bio-nanocomposites reinforced by Luffa cylindrica cellulose nanocrystals. *Journal of Membrane Science* **2013,** *427*, 218-229.
38. Carter, H. G.; Kibler, K. G., Langmuir-Type Model for Anomalous Moisture Diffusion In Composite Resins. *Journal of Composite Materials* **2016,** *12* (2), 118-131.
39. Brannon-Peppas, L.; Peppas, N. A., Equilibrium swelling behavior of pH-sensitive hydrogels. *Chemical Engineering Science* **1991,** *46* (3), 715-722.
40. Edwards, D. A., Non-fickian diffusion in thin polymer films. *Journal of Polymer Science Part B: Polymer Physics* **1996,** *34* (5), 981-997.
41. Amsden, B., Solute Diffusion within Hydrogels. Mechanisms and Models. *Macromolecules* **1998,** *31* (23), 8382-8395.
42. De Kee, D.; Liu, Q.; Hinestroza, J., Viscoelastic (Non-Fickian) Diffusion. *The Canadian Journal of Chemical Engineering* **2008,** *83* (6), 913-929.
43. Vrentas, J. S.; Duda, J. L., Diffusion in polymer–solvent systems. II. A predictive theory for the dependence of diffusion coefficients on temperature, concentration, and molecular weight. *Journal of Polymer Science: Polymer Physics Edition* **1977,** *15* (3), 417-439.
44. Vrentas, J. S.; Duda, J. L., Diffusion in polymer—solvent systems. I. Reexamination of the free-volume theory. *Journal of Polymer Science: Polymer Physics Edition* **1977,** *15* (3), 403-416.
45. Baij, L.; Hermans, J. J.; Keune, K.; Iedema, P. D., Time-Dependent ATR-FTIR Spectroscopic Studies on Solvent Diffusion and Film Swelling in Oil Paint Model Systems. *Macromolecules* **2018,** *51* (18), 7134-7144.
46. De Marco, L.; Carpenter, W.; Liu, H.; Biswas, R.; Bowman, J. M.; Tokmakoff, A., Differences in the Vibrational Dynamics of H(2)O and D(2)O: Observation of Symmetric and Antisymmetric Stretching Vibrations in Heavy Water. *J Phys Chem Lett* **2016,** *7* (10), 1769-74.
47. Vincent, M. F.; Kazarian, S. G.; Eckert, C. A., "Tunable" diffusion of D2O in CO2-swollen poly(methyl methacrylate) films. *AIChE Journal* **1997,** *43* (7), 1838-1848.
48. Kazarian, S. G.; Chan, K. L., ATR-FTIR spectroscopic imaging: recent advances and applications to biological systems. *Analyst* **2013,** *138* (7), 1940-51.

49. Breen, A. F.; Breen, C.; Clegg, F.; Döppers, L.-M.; Khairuddin; Labet, M.; Sammon, C.; Yarwood, J., FTIR-ATR studies of the sorption and diffusion of acetone:water mixtures in poly(vinyl alcohol)-clay nanocomposites. *Polymer* **2012,** *53* (20), 4420-4428.
50. Max, J. J.; Chapados, C., Isotope effects in liquid water by infrared spectroscopy. III. H2O and D2O spectra from 6000 to 0 cm(-1). *J Chem Phys* **2009,** *131* (18), 184505.

4.5 Supporting Information

4.5.1 Percolation Model

The percolation model shown in Eq. (S15) was fit to the experimental data using a sum of squares residual method in which the following parameters in Table S4-1 were used. The percolation model utilized the rigid phase storage modulus (7.4 GPa) as a fitting parameter which correlates well with previously reported rigid phase storage modulus of CNC-TPU composites (6.41 GPa)[1]

$$E_C = \frac{(1 - 2\psi + \psi v_R)E'_S E'_R + (1 - v_R)\psi {E'_R}^2}{(1 - v_R)E'_R + (v_R - \psi)E'_S} \tag{S15}$$

, where E_C is the elastic tensile modulus, ψ is the percolation fraction of the filler, v_R is the volume fraction of filler Equation (16), E'_S is the soft phase elastic tensile modulus and E'_R is the fillers elastic tensile modulus.

$$v_R = \frac{\frac{x}{\rho_{CNC}}}{\frac{x}{\rho_{CNC}} + \frac{1 - x}{\rho_{TPU}}} \tag{S16}$$

, where x is the mass fraction of CNCs as prepared during solution casting of CNC-TPU films, and ρ_{CNC} is the density of bulk crystalline cellulose, 1.52 g ml^{-1}, and ρ_{TPU} is the density of TPU measured as 1.07 g ml^{-1}. The fraction of filler which is acting as part of the percolating network can be estimated using Equation (S17)

$$\psi = v_R \left(\frac{v_R - v_{RC}}{1 - v_{RC}}\right)^b \tag{S17}$$

, where v_{RC} is the percolation threshold, and b is the critical percolation exponent which has been shown to equal 0.4 for 3D networks.[2, 3]

Table S4-1: Percolation Model Parameters

Parameter	Variable	Value	Units
Rigid Phase Storage Modulus	E'_R	7.4	GPa
Soft Phase Storage Modulus	E'_S	8.9	MPa
Filler Aspect Ratio	A_r	56.6	

4.5.2 Halpin-Kardos Model

The Halpin Kardos model was correlated to the wet state mechanical properties, since it was developed for reinforced networks that lack filler-filler interactions. The parameters used for this study are shown in Table S4-2 and details for mathematical operations required to calculate this value can be found elsewhere.[4] The correlation between the calculated values and experimental data shown in Figure 4-1a suggest that indeed the CNC network has decoupled and weakened to a state which can be described closely by models which do not account for these interactions, which is consistent with previously published results.[5]

Table S4-2: Halpin-Kardos Model Parameters

Parameter	Variable	Value	Units
Matrix Modulus	E_m	8.9	MPa
Longitudinal Filler Modulus	E_{Lf}	105	GPa
Transverse Filler Modulus	E_{Tf}	50	MPa
Filler Shear Modulus	G'_f	50	GPa

Matrix Shear Modulus	G'_m	2.1	MPa
Filler Length	L	158.5	nm
Filler Width	W	2.8	nm

4.5.3 Hindered Diffusion Parameters

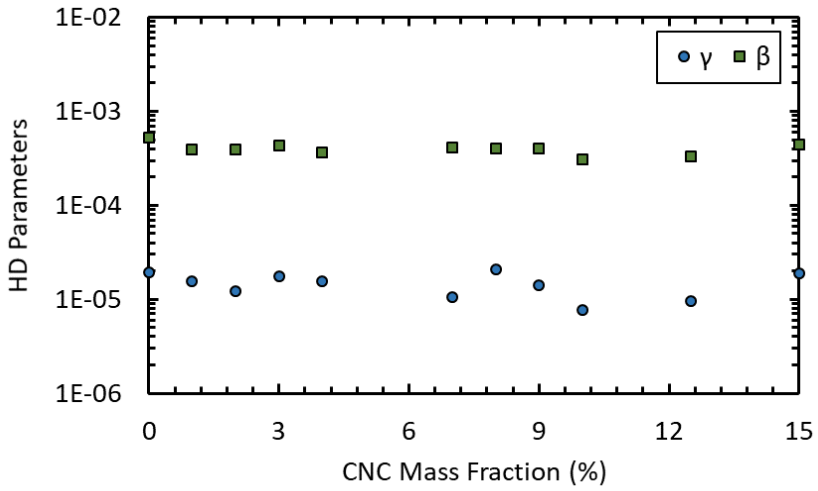

Figure S4-7. Fit parameters for the hindered diffusion model applied to TGA-SA data representing the probability of mobile water becoming bound, γ, and the probability of bound water becoming mobile, β.

4.5.4 FTIR-ATR of CNC-TPU as a function of D_2O diffusion

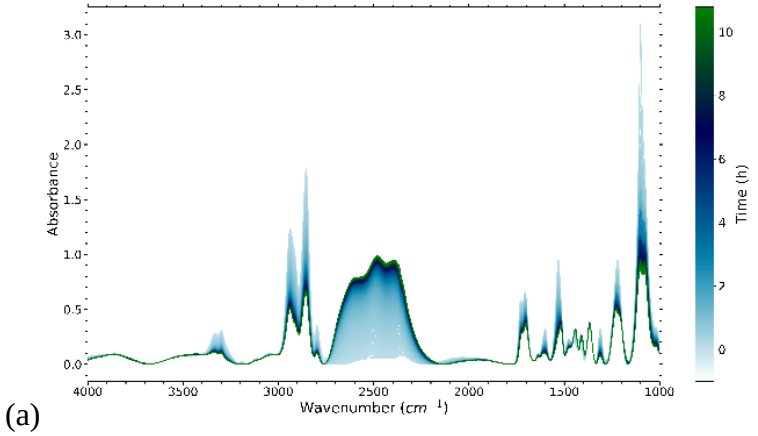

(a)

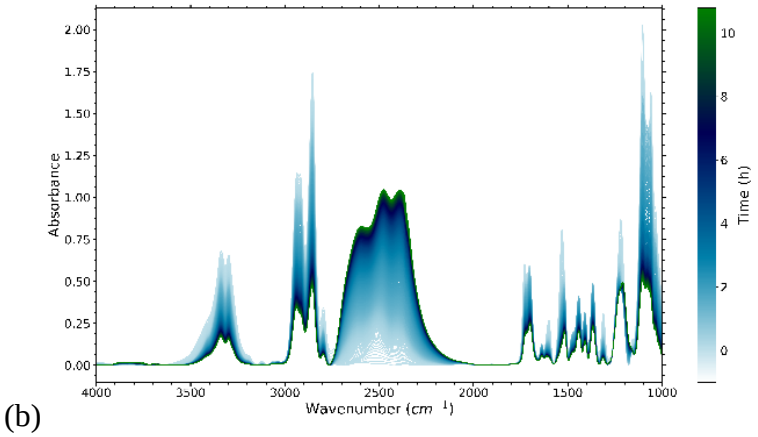

(b)

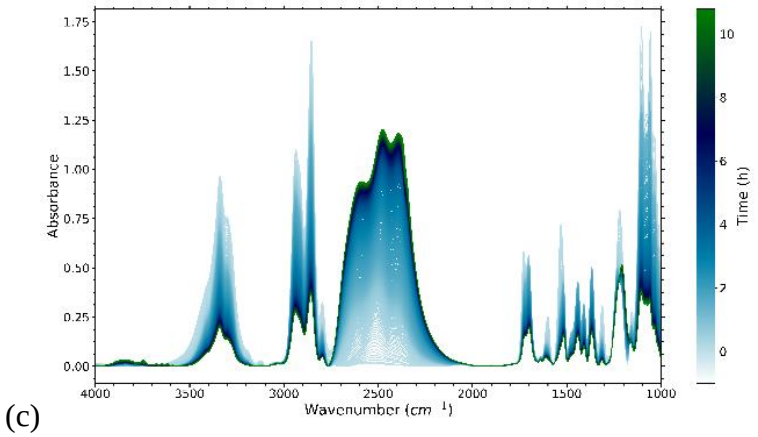

(c)

Figure S4-8. Typical FTIR-ATR spectra of (a) 1, (b) 8, and (c) 15 wt % CNC-TPU films exposed to one sided diffusion of D2O as a function time.

4.5.5 D_2O FTIR-ATR

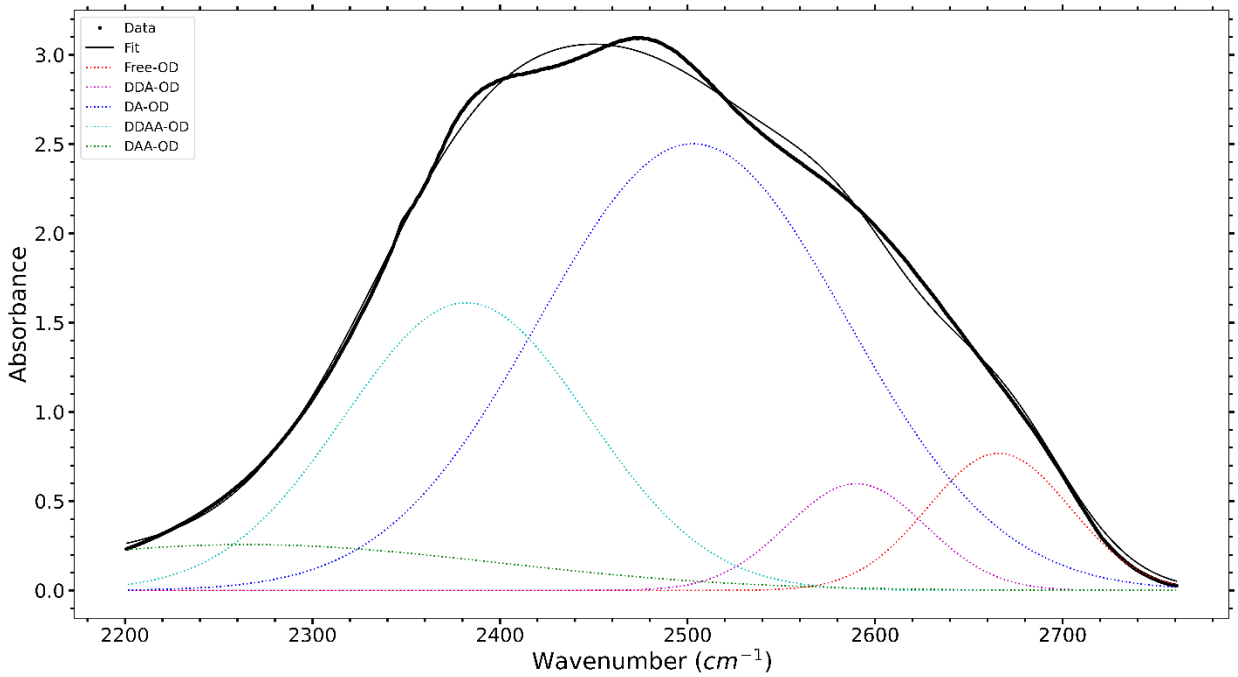

Figure S4-9. Deconvolution of a FTIR-ATR spectra of D2O showing the hydrogen bonding modes in the absence of CNC-TPU.

4.5.6 Diffusion-modified Percolation model parameters

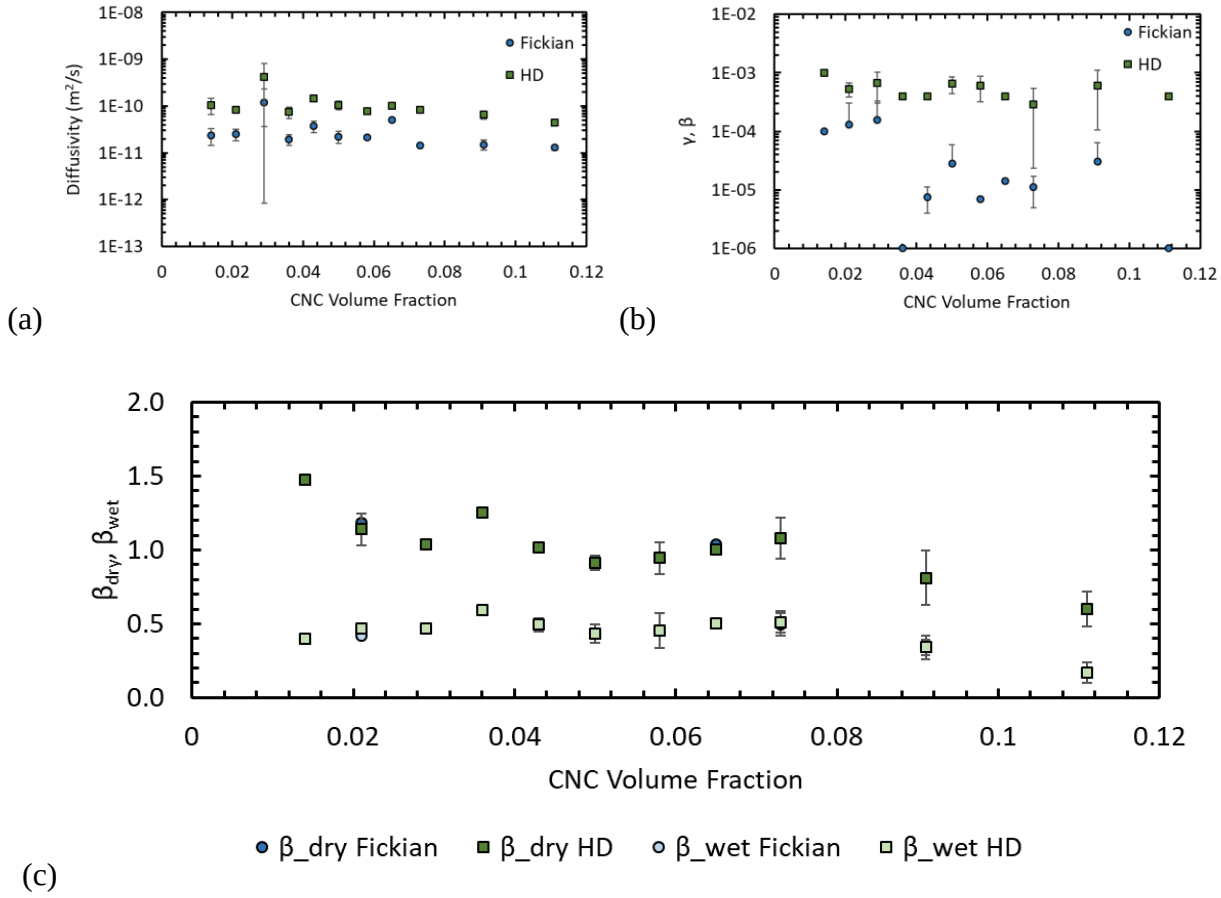

Figure S4-10. Percolation model parameters for (a) Fickian and (a, b) hindered diffusion models and dry and wet state beta parameters for diffusion-modified percolation models implemented with Fickian and hindered diffusion mass uptake profiles.

References

1. Meesorn, W.; Shirole, A.; Vanhecke, D.; de Espinosa, L. M.; Weder, C., A Simple and Versatile Strategy To Improve the Mechanical Properties of Polymer Nanocomposites with Cellulose Nanocrystals. *Macromolecules* **2017,** *50* (6), 2364-2374.
2. Stauffer, D. F.; Garton, E. O.; Steinhorst, R. K., A Comparison of Principal Components from Real and Random Data. *Ecology* **1985,** *66* (6), 1693-1698.
3. De Gennes, P.-G., *Scaling concepts in polymer physics*. Cornell university press: 1979.
4. Fallon, J. J.; Kolb, B. Q.; Herwig, C. J.; Foster, E. J.; Bortner, M. J., Mechanically adaptive thermoplastic polyurethane/cellulose nanocrystal composites: Process-driven structure–property relationships. *Journal of Applied Polymer Science* **2019,** *136* (4), 46992.
5. Annamalai, P. K.; Dagnon, K. L.; Monemian, S.; Foster, E. J.; Rowan, S. J.; Weder, C., Water-Responsive Mechanically Adaptive Nanocomposites Based on Styrene–Butadiene Rubber and Cellulose Nanocrystals Processing Matters. *ACS Applied Materials & Interfaces* **2014,** *6* (2), 967-976.

Chapter 5 - Multiscale reinforcement of cellulose nanofibers with cellulose nanocrystals

Cailean Q. Pritchard[1, 2], George Funk[2], James Owens[1, 2], Samantha Stutz[1, 2], Janak Sapkota[4], E. Johan Foster[5], Michael J. Bortner[1, 2, *]

[1]Department of Chemical Engineering, [2]Macromolecules Innovation Institute, Virginia Tech,
[4]UPM Biofore, Helsinki, Finland
[5]Department of Chemical and Biological Engineering, The University of British Columbia, Vancouver, Canada

*Corresponding author

This chapter is presented in the format of a manuscript that is in preparation for submission to ACS Carbohydrate Polymers.

The following contributions were made by other authors: Methodology for film casting was developed by Samantha Stutz and James Owens. James Owens also performed tensile testing on several film compositions. George Funk assisted in conducting atomic force microscopy, thermogravimetric analysis, and polarized light microscopy measurements. Dissipative particle dynamics simulations were developed and analyzed by Janak Sapkota.

The following people contributed to the writing of this chapter: Cailean Q. Pritchard (Original Draft), Janak Sapkota (Simulation methods, Review, and Editing), E. Johan Foster (Review and Editing), and Michael J. Bortner (Review and Editing)

5.1 Abstract

A novel nanocomposite comprised of cellulose nanocrystals (CNCs) and 2,2,6,6-tetramethylpiperidine 1-oxyl (TEMPO) oxidized cellulose nanofibers (TOCNFs) was prepared through solution casting to evaluate potential improvements of the mechanical performance compared to individual reinforcements alone. Such materials can be implemented as mechanical reinforcements in polymer composites, especially when less weight is desired. Dissipative particle dynamics (DPD) simulations, in combination with polarized light microscopy and atomic force microscopy, were analyzed to evaluate the morphology of these combined cellulose nanomaterial (CNM) films. Our results indicate that TOCNFs provide enhanced translational mobility to CNCs which become incorporated near the crystalline domains of TOCNFs. This mobility enables CNCs to increase the rigidity of the network without sacrificing elongation and toughness. The combination of these materials provides improved ultimate tensile strength and elongation without sacrificing the Young's modulus. Therefore, a combination of these materials can provide a unique reinforcing agent for polymer nanocomposites.

5.2 Introduction

Cellulose nanomaterials (CNMs) have been widely used as reinforcements in a variety of polymeric systems. Their usage as significant mechanical reinforcements are complimented by their environmentally friendly sourcing, rooting from naturally occurring cellulosic materials such as tunicates, craft softwood pulp, as well as several fruits. The renewable precursors to cellulose nanomaterials can be converted to cellulose nanocrystals (CNCs) through strong acid hydrolysis, or cellulose nanofibrils (CNFs) through high shear mechanical separation. Each of these nanocellulosics have been incorporated into polymers resulting in varying degrees of reinforcement as well as compromises.

CNCs have a single crystal Young's modulus of 116-167 GPa,[1, 2] which leads them to produce films that are brittle and more susceptible to changes in the mechanical performance of nanocomposites when exposed to water through the fragmentation of the inter CNC hydrogen bonding network.[3] In practical applications, neat films of CNCs do not reach their theoretical maximum stiffness due to inefficient stress transfer between particles at CNC-CNC interfaces.[4-6]. Neat CNC films are thus reported with moduli of approximately 6 GPa for wood CNCs, 5-10 GPa for tunicate CNCs and moduli up to 35 GPa for CNCs derived from bacterial cellulose.[7] In comparison, neat films of CNFs and 2,2,6,6- tetramethylpiperidine 1-oxyl (TEMPO) oxidized CNFs (TOCNFs) have a Young's modulus of 6-7 GPa[8] and 11-12 GPa[9], respectively and are able to better incorporate themselves into many polymer networks by providing reinforcement through TOCNF-matrix interactions which can dissipate tensile energy through cooperative motion within the matrix.[10] However, the lower Young's modulus leads to reduced mechanical enhancements.

The combination of CNCs and TOCNFs may yield a superior reinforcing agent that increases tensile strength and elongation, compared to CNCs alone, while not compromising on stiffness. Additionally, introducing TOCNFs will lower the overall density of the reinforcements thereby providing an improved potential as a lightweighting filler combination for polymer composites.[11, 12] We present the first combinations of CNCs and TOCNFs in standalone films and characterize their morphology and mechanical performance at various compositional ratios. Further, we discuss their potential use as a combination reinforcement in polymer composites. We utilized TOCNFs to enhance the compatibility of CNCs and CNFs in suspension, as TOCNFs have similar electrostatic interactions to CNCs,[8] and prevent localized agglomeration of either species. We utilize slow evaporative casting to facilitate the development free-standing CNC-TOCNF composite films where the electrostatic interactions between particles maintain proper dispersion

of each component as water is removed and ultimately results in enhanced film uniformity. Ultimately, CNCs were able to successfully incorporate with TOCNFs resulting in superior mechanical performance.

5.3 Materials and Methods

5.3.1 Cellulose Nanomaterials

CNCs were obtained from the forest products lab at the University of Maine as a 10.3 wt % slurry. CNCs were composed of 1.1 wt % Sulfur on a dry sodium form basis. Freeze-dried TOCNFs were also obtained from forest products lab at the University of Maine (properties). TOCNFs were re-dispersed in deionized (DI) H_2O, stirred at 300 rpm for 3 h, and then bath sonicated (Branson CPX5800H Ultrasonic Cleaner) for 1 h prior to CNC-TOCNF suspension preparation.

5.3.2 CNC-TOCNF Film Preparation

Dilute suspensions, containing 0.5 wt % of cellulose nanomaterials in DI H_2O, were prepared while adjusting the dry basis ratios of CNCs and TOCNFs for each suspension. Suspensions were stirred at 300 rpm for 30 min and subsequently bath sonicated for 30 min to ensure proper nanoparticle dispersion. The suspensions were poured into 15 cm clear glass petri dishes that were cleaned with a 1 wt % Alconox solution and rinsed with DI H_2O prior to casting, for a total volume of 180 ml. Notably, low-Fe glass petri dishes were also implemented, but resulted in very strong adhesion between the cellulose nanomaterials and glass which rendered films inaccessible for mechanical characterization. Samples were placed in a ThermoScientific Isotemp oven at 50°C for 36 h or until the suspension transitioned into a gel-like state. A convection oven was also studied for solvent casting, however, the forced airflow resulted in increased film wrinkling and poor reproducibility. After gelation, the samples were covered with

aluminum foil punctured with 9 symmetrically placed 5 mm pin holes and the temperature was dropped to 40°C until the drying was complete, typically 1 week. This second stage was performed to further slow the evaporation process, thereby allowing the CNCs and TOCNFs to assemble in a thermodynamically favorable manner. Films were removed from the oven and placed in a desiccator until characterized.

5.3.3 Polarized Light Microscopy

Cast films were observed between crossed polarizers with an OMAX 1708035 light microscope fitted with a polarizer, analyzer, and OMAX A35180U3 18 MP camera. The camera was controlled via AmScope software (v 3.7) with a brightness setting target of 40. Images were captured under 4x optical zoom in the center, annulus, and edge regions of each film and with the polarizer angle set to 0° and 90°.

5.3.4 Atomic Force Microscopy

5.3.4.1 Sample Preparation

CNCs were measured for dimensional analysis via AFM height profiles following the CAN/CSA-Z5100-17 Cellulose nanomaterials – Test methods for characterization.[13] Briefly, 9.9 mm PELCO Mica discs (Ted Pella Inc., #50) were glued to a glass slide with CubeStick (3D Systems Corp., PN # 390066-00). The mica discs were then immersed in 0.01 wt % poly(diallydimethylammonium chloride) (Aldrich, Lot# MKBW8603V, Mw < 100,000 g mol^{-1}) for 30 min, rinsed with DI H_2O five times and then dried in a N_2 stream. An aliquot (100 µL) of 0.1 wt % CNC suspension in DI H_2O was spin coated on the mica disc at 2000 rpm for 30 s. Prepared slides were immersed in DI H_2O to remove any non-adhered material and blown dry with N_2. CNC-TOCNF films were prepared for morphological analysis by adhering flat rectangular sections (1 cm x 3 cm) to glass slides with Elmer's rubber cement.

5.3.4.2 AFM Imaging Methods

AFM height profiles were characterized with an Asylum Research MFP-3D AFM and accompanying MFP-3D software. Olympus OMCL-AC200TS-R3 microcantilevers with a resonance frequency of 150 ± 100 kHz, nominal tip radius of 7 nm and a nominal spring constant of 9 N m^{-1} were used to evaluate the surface profile of CNM films. The typical response time for the cantilevers, measured by auto tuning and calculated from Equation 1, was 0.68 kHz with a Q factor of 314 ± 11 resulting in resonant frequencies of 146 ± 5 kHz.

$$\tau = \frac{Q}{\pi f_R} \tag{1}$$

Topographical and dimensional measurements, 1 µm x 1 µm, were collected using the alternating contact in air mode with 512 scan points and scan lines, corresponding to 2 nm $pixel^{-1}$ resolution, with a typical amplitude set point of 800 mV. Typically, the CNCs used in this study were 123 nm in length and 5 nm in height.

5.3.5 Instron Tensile Testing

Flat samples of CNC-TOCNF films were cut using two parallel razor blades separated with a 6 mm spacing block in to rectangular sheets derived from regions of the parent film (center, mid-point, edge). Sample dimensions were 6 mm x 5 mm x 30 µm (width, height measured with Pittsburgh calipers $\pm$ 5 µm, and thickness measured with a Mitutoyo micrometer $\pm$ 0.5 µm). Tensile tests were carried out using custom film clamps (supporting information) secured with a torque of 0.45 N m on each bolt. Films were stretched in tension at 0.5 mm min^{-1} until failure. The Young's modulus, ultimate tensile strength, and elongation at break were characterized according to ASTM E111-97.[14]

5.3.6 X-ray Diffraction

The crystalline content of CNC-TOCNF composites was evaluated from X-ray diffraction (Bruker D2 Phaser) operating at 30 kV and 10 mA with a Cu Kα radiation source, λ = 0.15432

nm. Films were placed on a Bruker AXS single Si crystal zero background specimen holder (C79298-A3244-B249) coated with Kapton tape. At least three replicates of each composition were collected from 5-60° with a scan increment of 0.1°, time step of 1 s, and a constant 1 rpm stage rotation. The scan was subsequently analyzed with Rietveld refinement using Profex[15] and following as specified in the CSA 2017 standard.[13]

5.3.7 Thermogravimetric Analysis

CNC-TOCNF films, approximately 5 mg, were heated on platinum pans from 30 to 500°C at 10°C min^{-1} in N_2 on a TA Instruments TGA5500 to characterize the thermal degradation behavior.

5.3.8 Dissipative Particle Dynamics Simulations

5.3.8.1 Simulation methods

CNC, TOCNF, and water molecules were simulated with coarse-graining and represented with dissipative particle dynamic (DPD) beads compromised of glucose units. CNCs and TOCNFs were assembled from 10 and 37 beads, respectively, to match our experimentally observed particle aspect ratios. The mechanical behavior of the beads was controlled through setting the harmonic potential between consecutive bonds *i* and *j* and with an angle, θ_{ij}, proportional to the Young's modulus of an individual CNC particle, ~160 GPa, or TOCNF fiber, ~80 GPa. The harmonic potential is given by Equation (18)

$$U_{angle}(\theta_{ij}) = k_\theta(\theta_{ij} - \theta_0)^2 \quad (18)$$

where, the harmonic constant, k_θ, was set to 100 and 50 $k_B T\,rad^{-2}$ for CNCs and TOCNFs respectively, and the equilibrium angle, θ_0 is 180°. Simulations were performed with the NVT ensemble within a cube side length of 26 nm with periodic boundary conditions on all sides. Randomly dispersed water, CNCs, and TOCNFs provided the initial configuration of the system which was followed by an equilibration period of 2 x 10^6 steps and simulation for another 2 x 10^6

steps with a time step of 37 fs. Additional details of the simulation are provided in the supporting information.

5.3.8.2 Dispersion Index

The dispersion index was evaluated through a Monte Carlo approach as a ratio of the simulated particle dispersion to that of an ideal uniformly dispersed system. Here, 10^5 points were randomly placed in the simulation and were counted if they were inside spheres representing the repulsive barrier of each nanoparticle. The number of counts was divided by the number of points found inside non-overlapping spheres of a uniformly dispersed system. Therefore, a larger dispersion index, maximum value of 1 for an ideally-dispersed system, implies increased dispersion quality of the nanoparticles. This procedure was repeated 10 times and the average is reported as the dispersion index.

5.4 Results and Discussion

The mechanical performance of CNC-TOCNF films was characterized though Instron mechanical testing, Figure 5-1, at a rate of 0.5 mm min^{-1}. The film casting technique implemented here aided the characterization of these materials as the glass petri dishes balanced the substrate adhesion of CNMs required to produce a complete film with the ability to easily separate the material without breakage. Additionally, custom film clamps, Figure S5-8, enabled high contact area for adequate grip while maintaining a controlled gripping force, required to minimize slippage during testing yet without crushing the film between the grips. At low CNC concentrations, adding CNCs increased the ultimate tensile strength, Figure 5-1b and elongation at break, Figure 5-1c where a maximum was achieved at approximately 10 wt % CNCs. Above this concentration, the ultimate tensile strength and elongation at break decreased, reflecting a reduction in toughness as the film crystallinity increases. The Young's modulus, Figure 5-1a, increased slightly with a 5 wt % addition of CNCs, but decreased upon further increasing the CNC mass fraction to 10 wt % and

beyond. Ultimately, the fraction of CNCs did not have a substantial impact on the composite film modulus despite having a lower modulus than neat TOCNF films, Figure 5-1a. The composite film modulus could be improved by using CNCs with a greater aspect ratio such as those sourced from tunicates or bacteria.[4] However, the ability of CNCs to mutually incorporate within the TOCNF network is a notable enhancement to the strength and elongation of these materials. Further, these interactions facilitate progress towards achieving the properties respective to individual CNMs.[2]

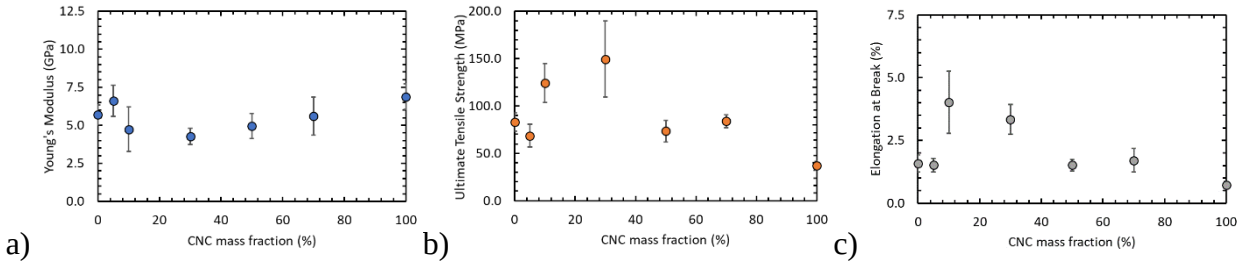

a) b) c)

Figure 5-1. Mechanical performance of CNC-TOCNF films as a function of CNC concentration. a) Young's modulus, b) ultimate tensile strength, and c) elongation at break.

As the density of fillers for nanocomposites is critical to their lightweighting performance, the density and porosity, Equation (19), of CNC-TOCNF films was characterized as a function of CNC concentration, Figure 5-2.

$$Porosity = \left(1 - \frac{\rho_{film}}{\rho_{cellulose}}\right) * 100\ \% \tag{19}$$

Where ρ_{film} is the density of CNM films and $\rho_{cellulose}$ is the ideal density of crystalline cellulose (1.5 g ml^{-1}).[9] CNM film density was calculated by measuring the mass and dimensions of 6 mm x 6 mm sections of thin films. While the density and porosity did not significantly change with increasing CNC concentration, the relatively low film density, 1.2 g ml^{-1} provides for significant lightweighting potential for these materials. Additionally, the high porosity of these films indicates that the slow solution casting method maintained the network developed at

high CNM concentrations.[7, 9] Further, the porosity is maintained across CNC compositions indicating the solution casting technique facilitates thermodynamically favorable interactions of CNCs and TOCNFs as opposed to kinetically restricted processing methods such as vacuum filtration and hot pressing.[9]

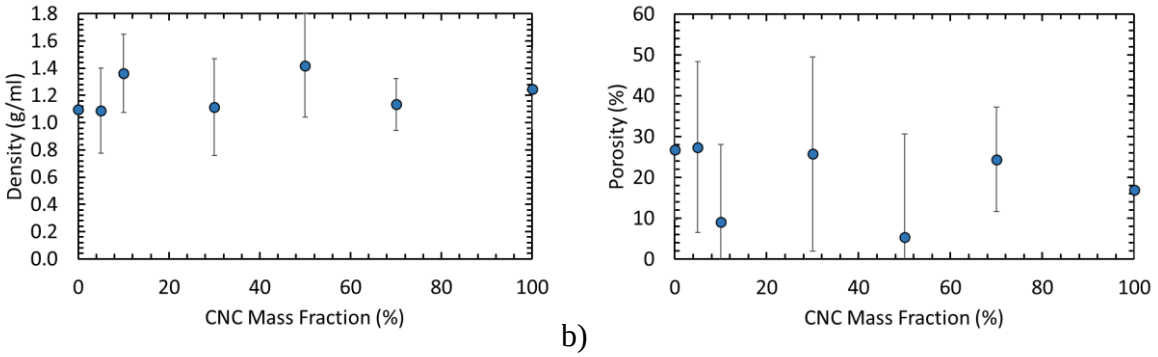

a) b)

Figure 5-2. Density and Porosity of CNC-TOCNF films as a function of CNC composition.

Interestingly, room temperature evaluation of CNMs mechanical properties is well below the theoretical glass transition temperature for cellulose, 220°C.[16] However, analysis of the mechanical performance in the rubbery state for cellulose-based materials is inaccessible due to the onset of thermal degradation also occurring at 220°C.[16] Therefore, the glassy state reinforcement of the ultimate tensile strength and elongation in CNC-TOCNF composite films with low CNC mass fraction may be provided through hydrogen bonding interactions which stiffen the TOCNF network, but do not hinder its motion. Further, CNCs are also able to translate along the axial direction of other hydrogen bonded CNCs or TOCNFs leading to enhanced toughness through extending the translational mobility of CNCs similar to the behavior reported for wood-based CNCs combined with tunicate-sourced CNCs.[4]

Crystallinity is well known to impact the mechanical performance of polymers and polymer composites.[17] Thus, the crystallinity was evaluated from x-ray diffraction profiles using Rietveld refinement to evaluate its correlation to the mechanical properties of CNM films.[15]

Crystallinity was found to increase with CNC mass fraction as expected when incorporating more highly crystalline material, Figure 5-3. Notably, the crystalline content of CNCs alone was only 90 %, suggesting there remains an amorphous component that can be attributed to short oligosaccharides on the surface on the crystalline particles which were unreacted during hydrolysis.[18] The TOCNFs remain highly crystalline, 70 %, in agreement with literature reports.[19] The composite crystallinity was found to be slightly greater than the expected crystallinity from a rule of mixtures analysis, Equation (20).

$$CI_{mix} = x_{CNC} CI_{CNC} + (1 - x_{CNC}) CI_{TOCNF} \quad (20)$$

A direct relationship between crystallinity and the mechanical properties in Figure 5-1 was not observed. While the modulus of individual CNM particles is expected to increase with crystallinity, the bulk film properties are primarily influenced by the weakest interactions in the film.[5] In this case, the crystallinity does not directly impact the interparticle bonding and stress transfer required to improve the mechanical performance. Nevertheless, optical and morphological changes within these films are expected as CNC concentration and crystallinity is increased.

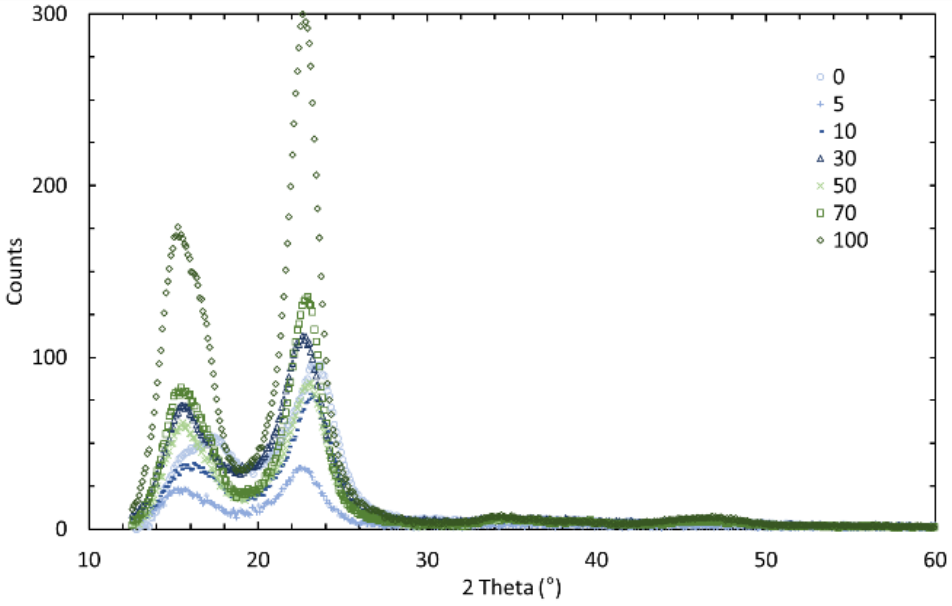

a)

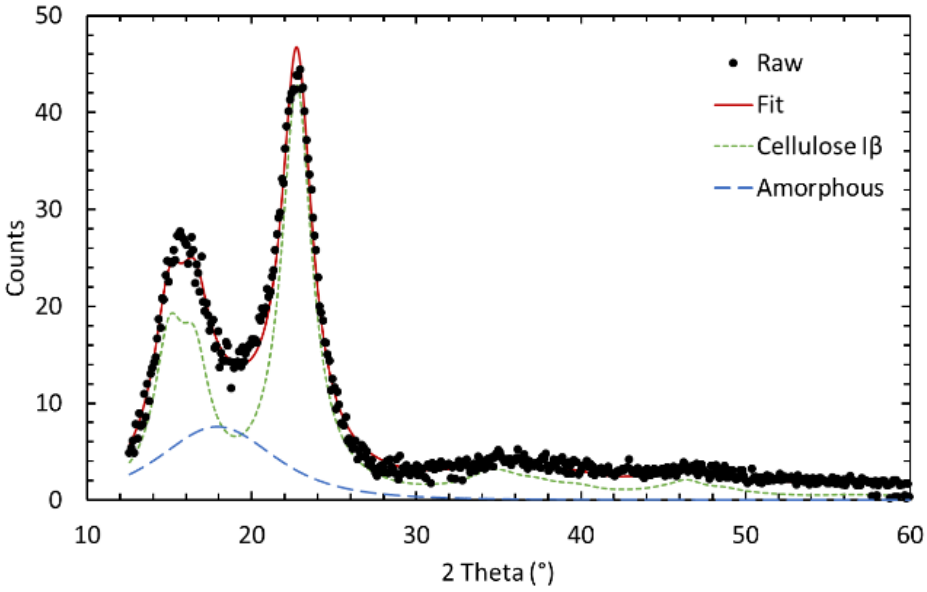

b)

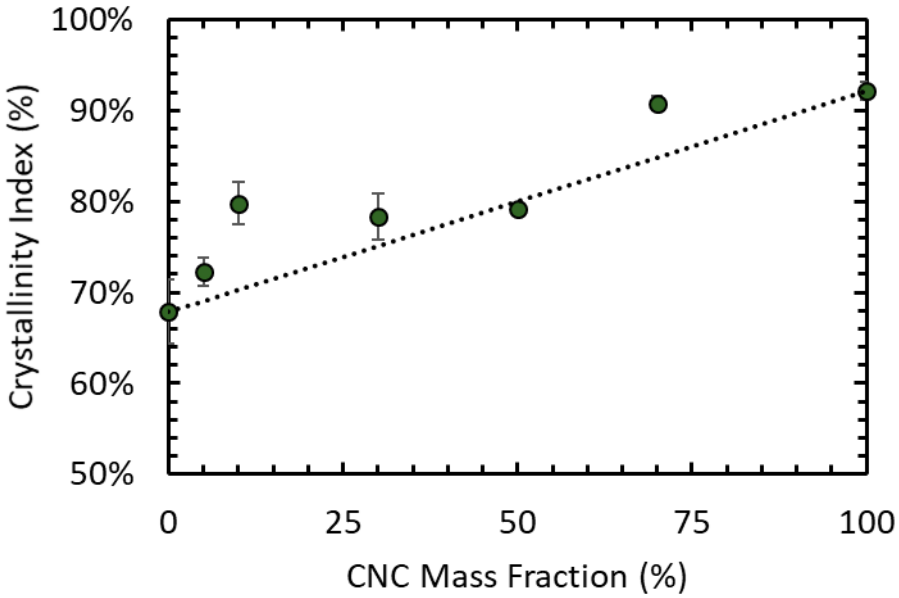

c)

Figure 5-3. a) XRD of CNC-TOCNF films as a function of CNC concentration. b) Fit of crystalline peaks from Rietveld refinement and c) calculated crystallinity index.

The morphology of CNM films after solution casting was investigated through polarized light microscopy (PLM) which is typically used to measure birefringence in CNCs suspensions

and films as well as liquid crystalline properties such as the chiral nematic pitch.[20, 21] Here we use crystalline cellulose birefringence to optically characterize crystalline and amorphous regions of each film. This enables the qualification of CNCs dispersions throughout the TOCNF network. Figure 5-4 illustrates the PLM response of CNM films as a function of composition and location within the cast film. The center, annular region, and edge of the films were analyzed to capture any effects of drying on the film morphology. Figure 5-4 (Edge) depicts a location-dependent response resulting from localized orientation of CNCs near the edge of the film. The center shows a bright textured surface throughout the image which indicates CNCs are randomly oriented resulting in a homogeneous passage of light through the film. Moving away from the center of the film, a ribbon like texture develops turning into segmented bands at the edge. These domains highlight a greater degree of anisotropy with respect to CNC orientation, quantified through the birefringence orientation index (BOI), Table 5-1.[22] Visualization of the orientation of crystalline cellulose, Figure S5-9, follows from the computation of the BOI. While orientation was found to slightly increase with CNC concentration and radial position, in general all samples maintained very low orientation as expected from the slow evaporation of these suspensions. This evaporation process allows CNCs and TOCNFs to thermodynamically equilibrate into their preferred orientation while drying. CNCs were found to develop chiral nematic films, attributed to their iridescence, which is characterized as a slight increase in BOI. However, As the chiral nematic state results in a helicoidal twist in liquid crystalline planes[21], the overall orientation of the film remains low.

Table 5-1. BOI as a function of film location and CNC mass fraction

CNC Mass Fraction (%)	**BOI**		
	Center	Annulus	Edge
0	0.001	0.000	0.015
5	0.039	0.039	0.009

10	0.065	0.051	0.078
30	0.038	0.001	0.089
50	0.000	0.079	0.001
70	0.102	0.036	0.001
100	0.046	0.063	0.201

In 70 wt % CNC films, the center location remains highly isotropic with decreasing isotropy near the edge. A transition was observed in 50 wt % CNC films where the center was highly amorphous while higher crystallinity was seen near the edge of the film. As the CNC composition was decreased to 30 wt %, the crystalline portions of CNC films had greatly improved distribution. Notably the birefringent domains were concentrated near defects in the films such as small air pockets formed during the casting process. Small concentrations, 5 and 10 wt %, of CNCs in films resulted in a noticeable increase in birefringent character with evenly distributed crystalline domains in the annular region. Finally, TOCNF films maintained excellent consistency in the distribution of its crystalline domains with respect to film location. These results indicate CNCs incorporate alongside the crystalline portions of the TOCNFs. This is in agreement with our analysis of the crystallinity index, Figure 5-3, where CNCs incorporating in the TOCNF network is represented by an increase in crystallinity index.

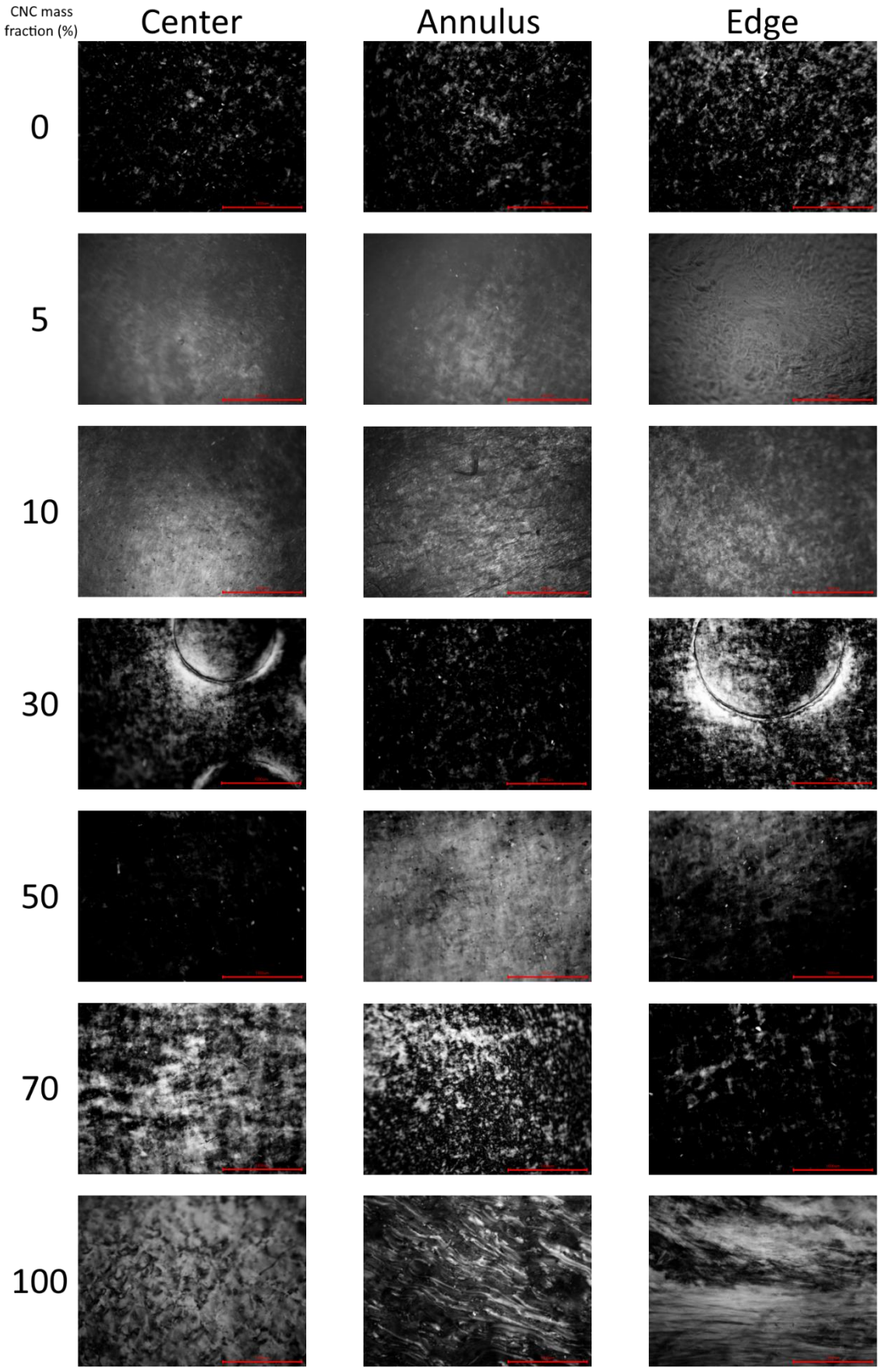
CNC mass fraction (%)
Center
Annulus
Edge
0
5
10
30
50
70
100

Figure 5-4. Crossed-polarized images of CNC-TOCNF films at different locations in the films progressing radially outward from the center. Scale bars are 1 mm.

DPD simulations were conducted to further investigate the tendency of CNCs to align with the crystalline regions of TOCNFs. Randomly distributed mixtures of CNCs and TOCNFs were allowed to equilibrate in water and their assembly and distribution was tracked as a function of time, Figure 5-5a. Simulated TOCNFs developed a percolating network and CNCs formed clusters of aggregates. These clusters reduce in size as more TOCNFs are introduced and a gradual transition from unstructured aggregates to spindle-like rods and then again to a percolating network is observed. When CNCs are the minority suspended nanoparticulate species they align amongst the straighter regions of the fibrous TOCNF network. In this sense, CNCs are supporting the lower bulk density of TOCNFs, but still act to increase the local density of the network. This is quantified through a decrease in the dispersion index, Figure 5-5b, from more dispersed TOCNFs, 0.44, to agglomerated CNCs, 0.33.

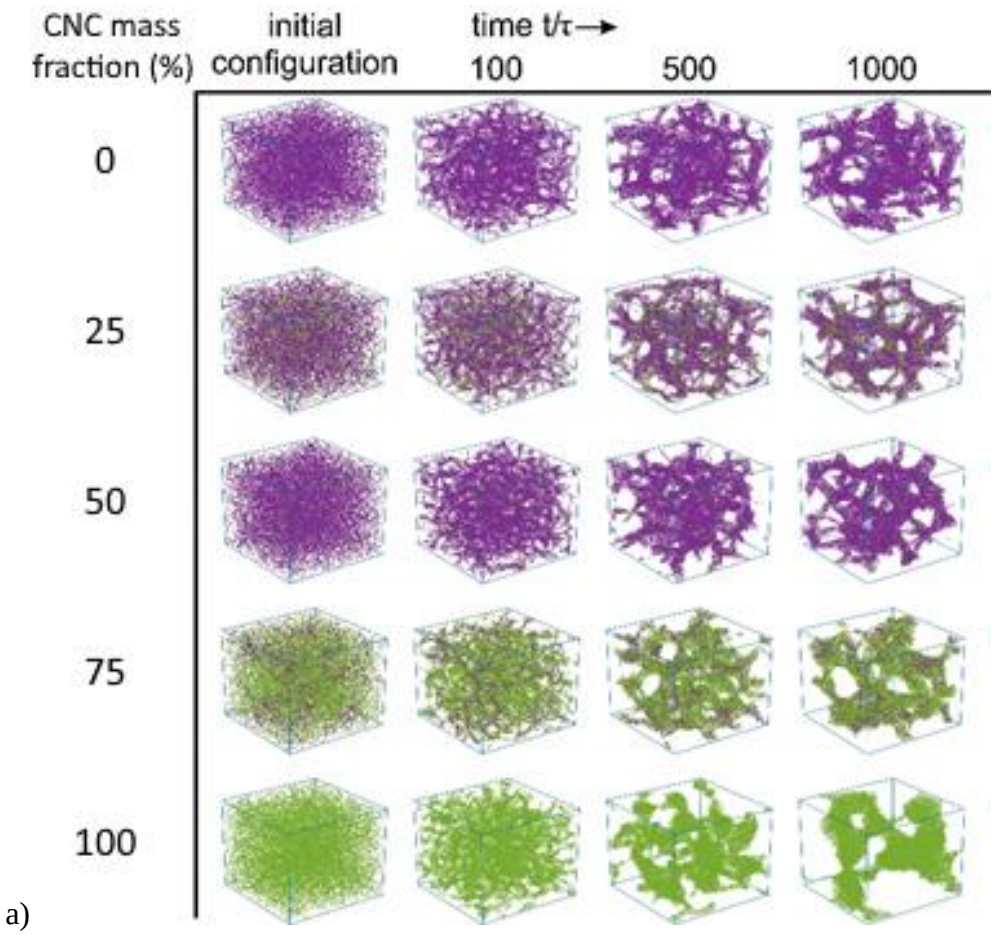

a)

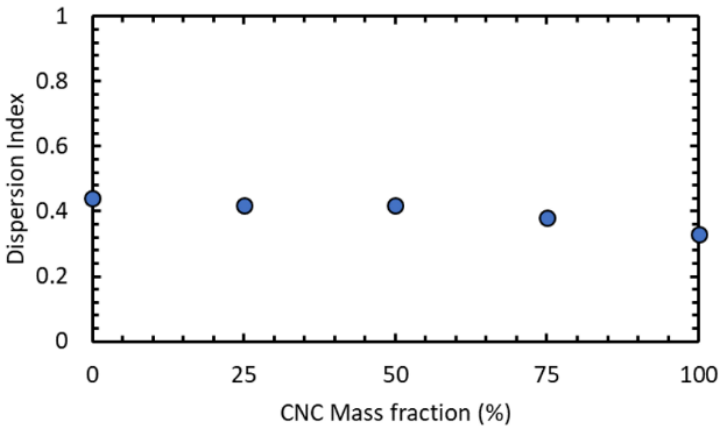

b)

Figure 5-5. a) Evolution of the morphology of CNC-TOCNF mixtures in water as a function of time. Note that water beads are not shown to preserve clarity. b) Dispersion index for equilibrated CNC-TOCNF suspensions as a function of CNC mass fraction. Standard deviation for the dispersion index was less than 0.05% for all compositions.

AFM was also used to investigate the morphology of CNC-TOCNF films, Figure 5-6. Here we see a distinct transition from a bundle of short rods in CNC films, Figure 5-6g, to a fibrous network of TOCNFs, Figure 5-6a, as predicted by the DPD simulations. As the TOCNF composition increases, CNCs are observed aligning in conjunction with the fibers of the TOCNF network. Films with low CNC loading, 5, 10, and 30 wt %, Figure 5-6b-c resemble a sparse network of TOCNFs interspersed with CNCs. At 10 wt % CNC, Figure 5-6c, large quantities of CNCs are observed supporting the TOCNF structure resulting in improved stress transfer and an enhanced ultimate tensile strength, Figure 5-1b. Upon increasing the CNC loading further, Figure 5-6d, the TOCNF network is robustly supported by CNCs throughout the majority of fibrils. This behavior was also observed in the DPD simulations, Figure 5-5a, at 25 wt %, confirming the experimentally observed CNC packing efficiency around the crystalline domains of TOCNFs. This preferred arrangement results in the increased tensile strength and elongation observed in Figure 5-1b, c. As the CNC concentration increases further, such that TOCNFs are no longer the majority species, Figure 5-6e-g, CNCs are more readily observed as bundles of rod like particles that are not supported by a fibrous network of TOCNFs. The CNC dominant morphology ultimately transfers stress between particles less efficiently resulting in reduced tensile strength and elongation at break, Figure 5-1b, c.

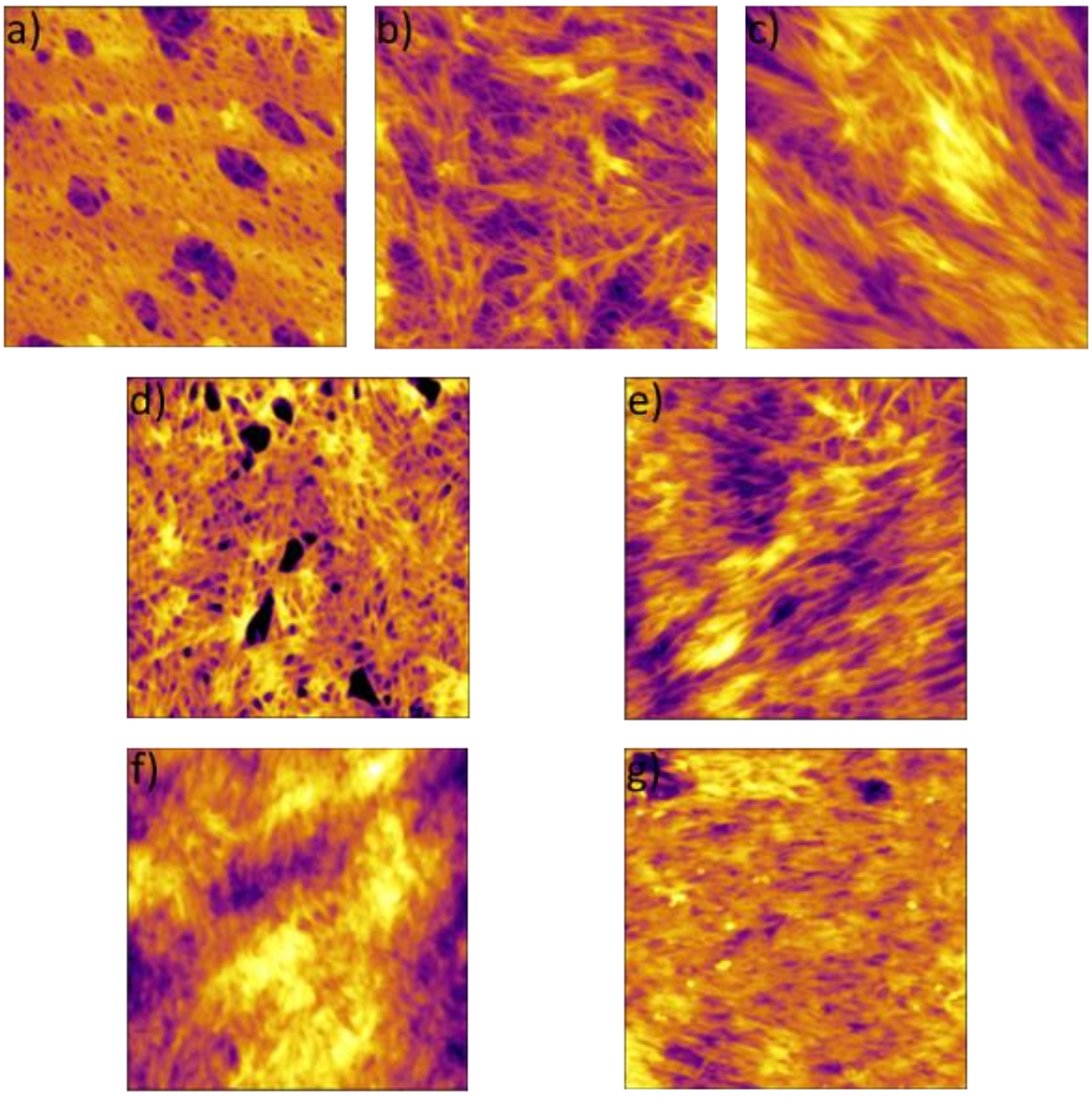

Figure 5-6. AFM height profiles, 1 µm x 1 µm, showing the change in morphology of CNC-TOCNF films as CNC mass fraction is increased. Lighter colors represent a greater elevation. a) 0, b) 5, c) 10, d) 30, e) 50¸ f) 70, and g) 100 wt % CNC

When considering their use in practical applications, CNM composites tend to be sensitive to elevated temperatures due to the thermal degradation of cellulose. Typically, this degradation can occur at lower temperatures than the matrix material.[16] Thus, the thermal degradation characteristics of CNC-TOCNF films were evaluated, Figure 5-7, for their future inclusion in

polymer matrices. As the CNC concentration is increased, two distinct degradation peaks can be identified in the derivative graphs, Figure S5-10, which shift to higher temperatures. The pure CNC films, however, show a large degradation peak at 230°C but a very small peak around 350°C. The first peak is expected to be associated with the breakup of crystalline cellulose via sulfate half ester, or carboxyl groups resulting from the acid hydrolysis method used during CNC production or TEMPO post-processing of TOCNFs.[8] The second peak is associated with chain scission of small oligosaccharides present in CNCs or the amorphous component of TOCNFs which maintains a greater free volume and is thus more susceptible to chemical attack.[18] Interestingly, the addition of CNCs broadens the degradation of TOCNFs, through a competition between the sulfate half ester and carboxyl groups.[23] This suggests the combination of these materials may serve to increase the thermal resistance of polymer composites using CNC-TOCNFs as reinforcing agents.

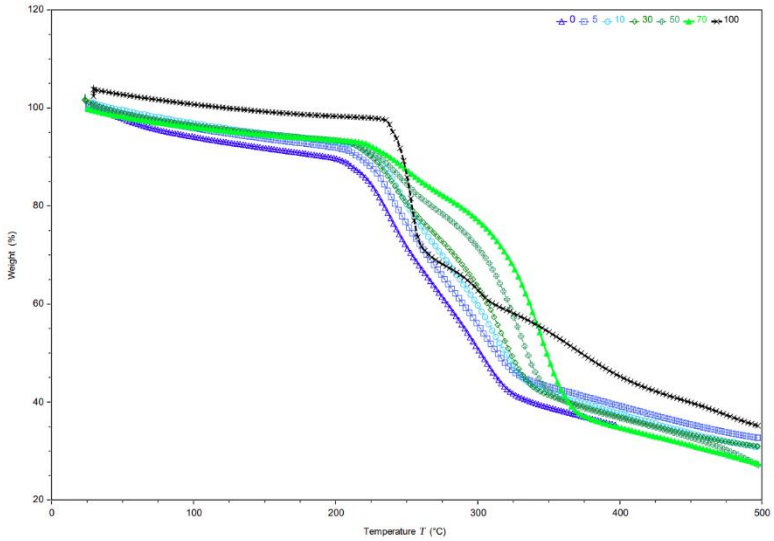

Figure 5-7. TGA of CNC-TOCNF films as a function CNC concentration in N2.

5.5 Conclusion

Mixtures of CNCs and TOCNFs were prepared and cast into thin films to investigate their properties and understand the cooperative effects of combined CNMs which exhibit vastly different morphologies. A morphological transition between a percolating fibrous network of

TOCNFs to clusters of short rods of CNCs was observed with increasing CNCs. The morphology of the mixture reflected the majority CNM population, however, the influence of the minority CNM species could be distinctly observed with as little as 30 wt %. DPD simulations and PLM revealed an inclination for CNCs to aggregate around the crystalline domains of TOCNFs through hydrogen bonding. The crystallite enhancement was confirmed through XRD analysis where the composite film crystallinity was greater than the crystallinity expected from a rule of mixtures analysis alone. TOCNFs also provided translational mobility to CNCs which could migrate along the TOCNF network while under an applied strain resulting in improved mechanical performance. The mechanical performance of CNC-TOCNF films was optimal with a low CNC mass fraction, 5-10 wt %, where the films exhibited an increased ultimate tensile strength and elongation. Finally, increased thermal stability was observed with increasing CNC content, yet the greatest stability did not coincide with the low CNC concentration as found in the mechanical response. These results highlight the potential for a novel mixture of CNCs and TOCNFs for potential use as mechanical reinforcements in polymer composites with improved mechanical and thermal performance compared to individual CNM reinforcements alone. Finally, an additional benefit arises from incorporating lower density TOCNFs, thereby reducing the overall density of the combined filler. Thus, density reductions of approximately 0.2 g ml^{-1} could be realized when combining CNMs in contrast to implementing CNC reinforcements alone.

References

1. Tashiro, K.; Kobayashi, M., Theoretical evaluation of three-dimensional elastic constants of native and regenerated celluloses: role of hydrogen bonds. *Polymer* **1991,** *32* (8), 1516-1526.
2. Eichhorn, S. J.; Davies, G. R., Modelling the crystalline deformation of native and regenerated cellulose. *Cellulose* **2006,** *13* (3), 291-307.
3. Mendez, J.; Annamalai, P. K.; Eichhorn, S. J.; Rusli, R.; Rowan, S. J.; Foster, E. J.; Weder, C., Bioinspired Mechanically Adaptive Polymer Nanocomposites with Water-Activated Shape-Memory Effect. *Macromolecules* **2011,** *44* (17), 6827-6835.

4. Natarajan, B.; Krishnamurthy, A.; Qin, X.; Emiroglu, C. D.; Forster, A.; Foster, E. J.; Weder, C.; Fox, D. M.; Keten, S.; Obrzut, J.; Gilman, J. W., Binary Cellulose Nanocrystal Blends for Bioinspired Damage Tolerant Photonic Films. *Advanced Functional Materials* **2018,** *28* (26).
5. Natarajan, B.; Lachman, N.; Lam, T.; Jacobs, D.; Long, C.; Zhao, M.; Wardle, B. L.; Sharma, R.; Liddle, J. A., The Evolution of Carbon Nanotube Network Structure in Unidirectional Nanocomposites Resolved by Quantitative Electron Tomography. *ACS Nano* **2015,** *9* (6), 6050-8.
6. Saito, T.; Kuramae, R.; Wohlert, J.; Berglund, L. A.; Isogai, A., An ultrastrong nanofibrillar biomaterial: the strength of single cellulose nanofibrils revealed via sonication-induced fragmentation. *Biomacromolecules* **2013,** *14* (1), 248-53.
7. Moon, R. J.; Martini, A.; Nairn, J.; Simonsen, J.; Youngblood, J., Cellulose nanomaterials review: structure, properties and nanocomposites. *Chem Soc Rev* **2011,** *40* (7), 3941-94.
8. Isogai, A.; Saito, T.; Fukuzumi, H., TEMPO-oxidized cellulose nanofibers. *Nanoscale* **2011,** *3* (1), 71-85.
9. Qing, Y.; Sabo, R.; Zhu, J. Y.; Agarwal, U.; Cai, Z.; Wu, Y., A comparative study of cellulose nanofibrils disintegrated via multiple processing approaches. *Carbohydr Polym* **2013,** *97* (1), 226-34.
10. Xu, X.; Liu, F.; Jiang, L.; Zhu, J. Y.; Haagenson, D.; Wiesenborn, D. P., Cellulose nanocrystals vs. cellulose nanofibrils: a comparative study on their microstructures and effects as polymer reinforcing agents. *ACS Appl Mater Interfaces* **2013,** *5* (8), 2999-3009.
11. Alexander B. Reising, R. J. M., Jeffrey P. Youngblood, Effect of Particle Alignment on Mechanical Properties of Neat Cellulose Nanocrystal Films. *Journal of Science & Technology for Forest Products and Processes* **2012,** *2* (6), 32-41.
12. Henriksson, M.; Berglund, L. A.; Isaksson, P.; Lindstrom, T.; Nishino, T., Cellulose nanopaper structures of high toughness. *Biomacromolecules* **2008,** *9* (6), 1579-85.
13. Z5100-17 Cellulosic nanomaterials — Test methods for characterization. In *Atomic Force Microscopy*, CSA Group: Ontario, Canada, 2017; pp 43-46.
14. ASTM, Standard Test Method for Young's Modulus, Tangent Modulus, and Chord Modulus. In *E 111 – 97*, 1997.
15. Doebelin, N.; Kleeberg, R., Profex: a graphical user interface for the Rietveld refinement program BGMN. *J Appl Crystallogr* **2015,** *48* (Pt 5), 1573-1580.
16. Szcześniak, L.; Rachocki, A.; Tritt-Goc, J., Glass transition temperature and thermal decomposition of cellulose powder. *Cellulose* **2007,** *15* (3), 445-451.
17. Batista, N. L.; Olivier, P.; Bernhart, G.; Rezende, M. C.; Botelho, E. C., Correlation between degree of crystallinity, morphology and mechanical properties of PPS/carbon fiber laminates. *Materials Research* **2016,** *19* (1), 195-201.
18. Bouchard, J.; Méthot, M.; Fraschini, C.; Beck, S., Effect of oligosaccharide deposition on the surface of cellulose nanocrystals as a function of acid hydrolysis temperature. *Cellulose* **2016,** *23* (6), 3555-3567.
19. Qua, E. H.; Hornsby, P. R.; Sharma, H. S. S.; Lyons, G., Preparation and characterisation of cellulose nanofibres. *Journal of Materials Science* **2011,** *46* (18), 6029-6045.
20. Gray, D., Recent Advances in Chiral Nematic Structure and Iridescent Color of Cellulose Nanocrystal Films. *Nanomaterials* **2016,** *6*, 213.

21. Gray, D. G.; Mu, X., Chiral Nematic Structure of Cellulose Nanocrystal Suspensions and Films; Polarized Light and Atomic Force Microscopy. *Materials (Basel)* **2015,** *8* (11), 7873-7888.
22. Ghasemi, S.; Rahimzadeh-Bajgiran, P.; Tajvidi, M.; Shaler, S. M., Birefringence-based orientation mapping of cellulose nanofibrils in thin films. *Cellulose* **2019,** *27* (2), 677-692.
23. Kargarzadeh, H.; Ahmad, I.; Abdullah, I.; Dufresne, A.; Zainudin, S. Y.; Sheltami, R. M., Effects of hydrolysis conditions on the morphology, crystallinity, and thermal stability of cellulose nanocrystals extracted from kenaf bast fibers. *Cellulose* **2012,** *19* (3), 855-866.

5.6 Supporting Information

5.6.1 Instron Tensile Testing

Custom film clamps, Figure S5-8a, enabled high contact area for adequate grip while maintaining a controlled gripping force. A torque wrench was used to tighten the four screws on each clamp in a star pattern to a torque of 10 N m^{-1} to ensure even clamping pressure. This gripping method enabled testing of CNC films by preventing brittle failure during sample loading and minimizing slippage during testing.

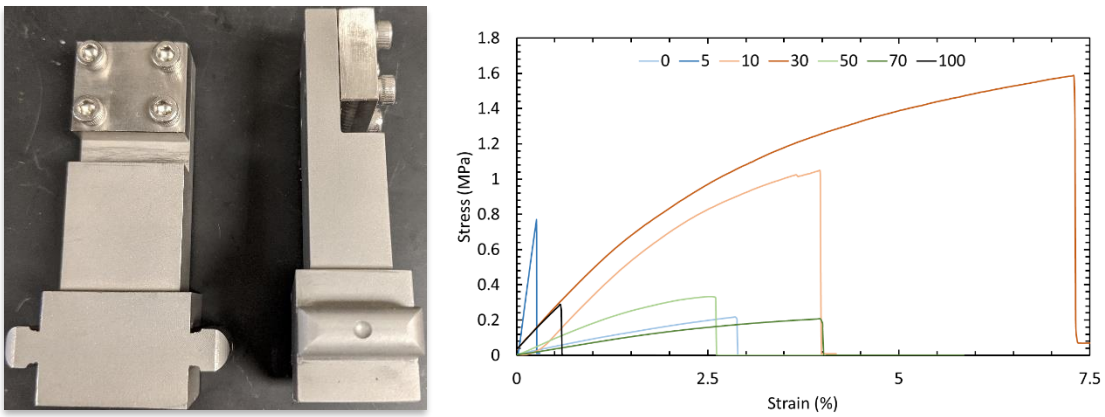

Figure S5-8. a) Custom film clamps used for Instron testing of CNC-TOCNF films and b) typical tensile curves for CNC-TOCNF films with CNC mass fraction ranging from 0 – 100 wt %.

5.6.2 Birefringent Orientation Index

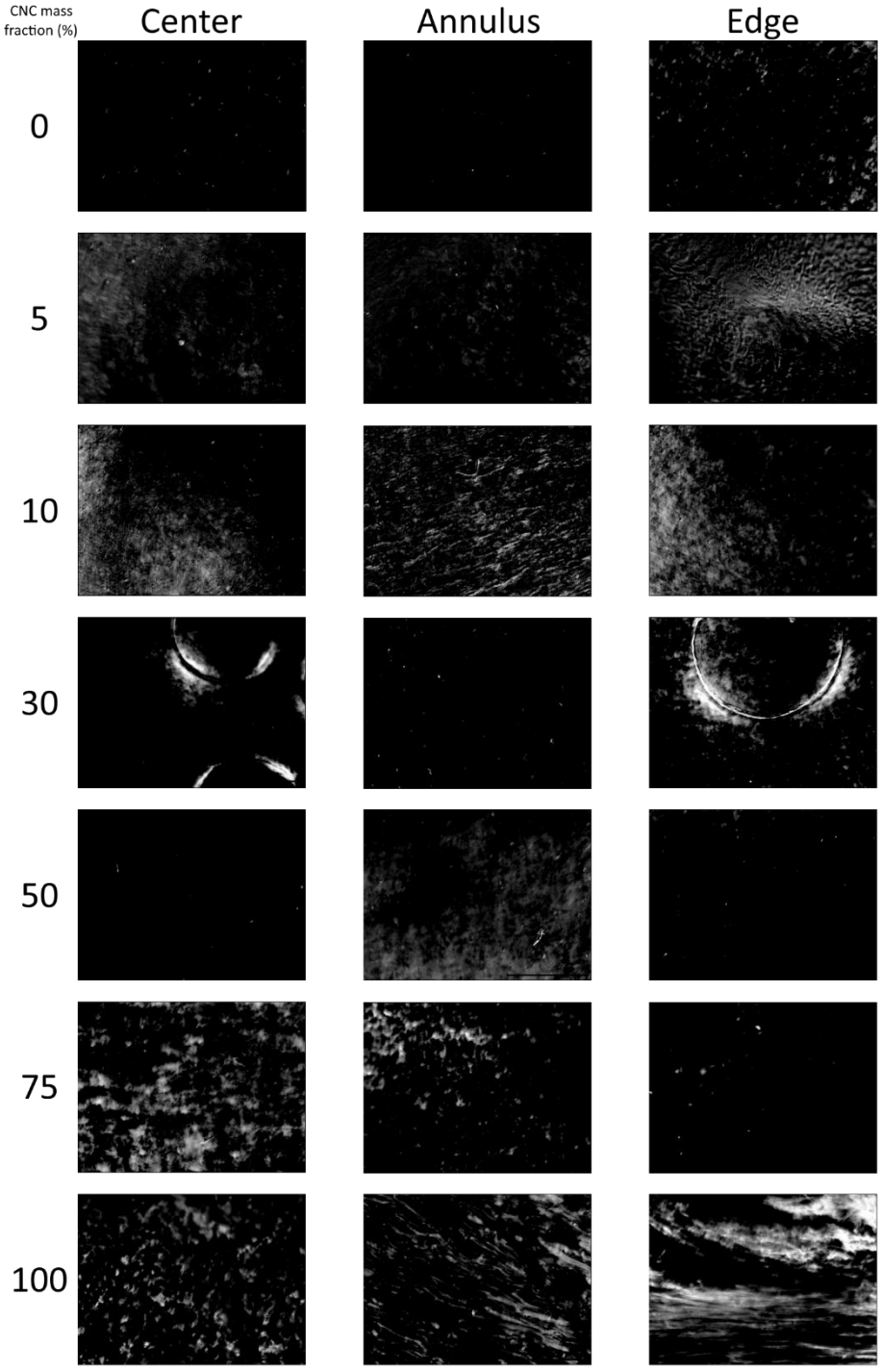

Figure S5-9. Difference images for calculation of the birefringent orientation index

5.6.3 Derivative Thermogravimetric Analysis (DTGA)

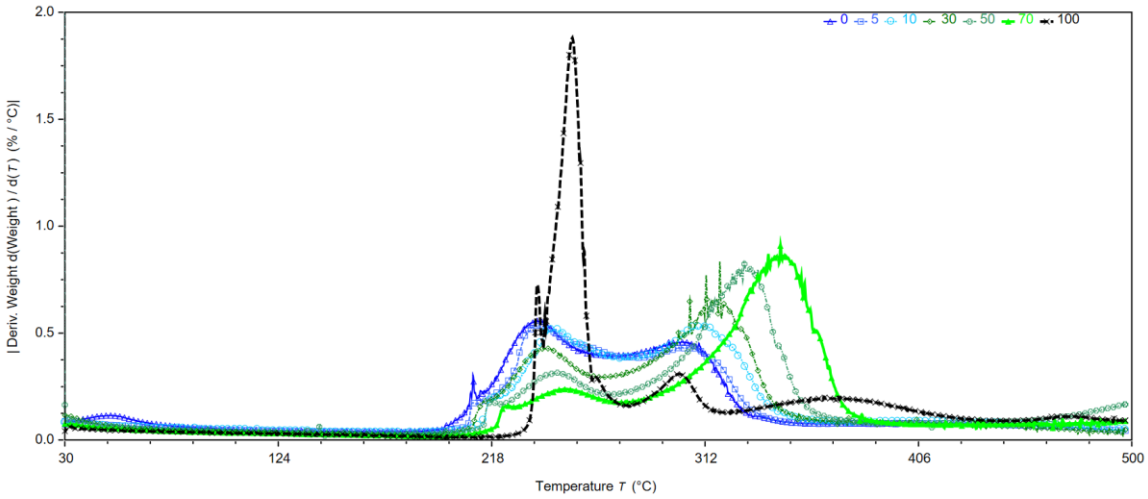

Figure S5-10. DTGA curves showing two degradation modes in CNC-TOCNF films.

5.6.4 DPD Simulations

Table S5-2. Evolution of the dispersion index with time.

CNC mass fraction (%)	Initial configuration	Time (t/τ)		
	0	**100**	**500**	**1000**
0	0.98	0.76	0.51	0.44
25	0.98	0.76	0.50	0.42
50	0.98	0.76	0.50	0.42
75	0.98	0.74	0.45	0.38
100	0.99	0.73	0.42	0.33

*standard deviation was less than 0.05% for each values listed in table.

Chapter 6 - Conclusions and Recommendations for Future Work

6.1 Conclusions

1. Interactions between CNCs in evaporating suspensions are tied to unsteady state mass, momentum, and thermal transport. Specifically, these transport phenomena govern the local particle concentration which influences the degree to which CNCs interact with one another prior to deposition and in turn directly impacts the final orientation. CNC interactions were characterized via polarized light microscopy (PLM) and atomic force microscopy (AFM) which revealed multiple modes of alignment in drying droplets. These results were supported by computational analysis of the rotational Péclet number which ruled out hydrodynamic shear-induced orientation effects. Ordered domains were observed near the receding contact line as evaporation progressed. These ordered domains were observed above a critical local particle concentration such that the size of these domains was detectable via optical microscopy. Further, the local particle concentration was found to control the orientation of deposited CNCs. At high particle concentrations confinement amidst the droplet's contact line, particularly at the beginning of evaporation, led to the development of tangentially oriented CNCs. However, as the local particle concentration decreased below a threshold, particle interactions no longer supported the rotation of CNCs amidst the boundary, instead radial orientation was produced. Thus, the dynamic changes in particle orientation within the droplet are highly dependent on interfacial surface tension and cooperative interactions, or the lack there of, between CNCs.
2. CNCs have also been used to impart water-responsive mechanical adaptivity in polymer nanocomposites. CNCs above a critical percolation concentration develop a hydrogen

bonding network which greatly enhances the stiffness of the matrix. As water is absorbed into these materials, a competition for these hydrogen bonding sites is developed and the network is disrupted resulting in softening of the composite material. Investigation of the relationship between water diffusion and the mechanical softening response revealed the critical role of interactions between CNCs on the overall mechanical performance of these materials. CNCs were found to increase the hydrophilicity of the composite thereby increasing water uptake. Critically, the increased water uptake leads to greater swelling of the bulk composite which must be accounted for in future diffusion analyses. A modification to the percolation model, which has been widely used to predict the dry state storage modulus as a function of filler concentration, was developed to extend the analysis to the wet state. It was then possible to develop a direct relationship between the degree of inter-CNCs interactions and the modulus as a function of time by connecting the mass transport of solvent molecules.

3. The interactions of CNCs with other CNMs were studied for their potential as reinforcing fillers in nanocomposite materials. A combination of 5-10 wt % CNCs and TEMPO oxidized cellulose nanofibers (TOCNFs) was found to have improved tensile strength and elongation characteristics. These enhancements were facilitated by the incorporation of CNCs along the crystalline domains of TOCNFs as confirmed by x-ray diffraction and validated with PLM and AFM. These interactions further provided for an increased translational mobility of CNCs thus leading the observed mechanical enhancements. These results emphasize the potential of combined CNMs to serve as combination fillers with improved reinforcing behavior in polymer nanocomposites.

6.2 Scientific Contributions

1. Discovery of multiple orientation modes of rod-shaped nanoparticles developed through a dynamic evaporation process. The first report of radial alignment of CNCs in self-assembled systems
2. Development of a time-resolved polarized light microscopy technique to characterize the evolution of particle orientation in birefringent materials
3. Quantified the dependence of water diffusion on CNC concentration in CNC-TPU nanocomposites and its connection to the softening these materials experience upon water uptake
4. Demonstrated bulk composite swelling accounts for the apparent decrease in diffusivity in CNC-TPU nanocomposites as CNC concentration is increased
5. Developed a mathematical correlation between the hydrogen bonding state of CNCs in nanocomposites above the critical percolation concentration and the diffusive mass transport of water into these materials as a function of CNC concentration
6. Proposed a model to fully predict the time-dependent mechanical response of CNC-TPU nanocomposites as a function of CNC concentration and water saturation
7. Developed a combination of CNMs which can be used as a nanocomposite filler and provides extended elongation and tensile strength over the individual CNMs components alone

6.3 Recommendations for Future Work

1. Fluid transport simulations of CNC suspensions involve rheological properties which are difficult to describe with conventional approaches, especially in the limit of high CNC concentration. Development of a reliable concentration-dependent rheological model applicable to nanoscale rod-shaped particulate suspensions would facilitate our understanding of CNC suspensions and aid in the promote the utility of these materials in a variety of applications. The groundwork for a Landau-de Gennes orientation model is presented in Appendix A to facilitate the development of this work.

2. Measurements of Frank's elastic constants for liquid crystalline materials, required for Equations (A5)-(A9) , would aid in validating newly developed rheological models for highly concentrated CNC suspensions. Specifically, measurements of these constants would reduce the number of adjustable parameters required to implement the Landau-de Gennes orientation model and increase the predictive potential for these simulation approaches.

3. Simulations involving the proposed rheological model would greatly improve our understanding of the relationships between the interactions of CNCs and macroscale fluid properties. Thus, bridging the experimental gap between simulations on multiple length scales would enable study of colloidal suspensions generally. Further, these studies will extend our understanding of concentrated suspensions, particularly for anisotropic materials, which are currently applicable to hard spheres. For example, simulating CNC orientation developed in evaporating droplets from Chapter 3 would enable extended analysis of the fundamental relationships driving the observed preferential orientation of CNCs. Further, these simulations may improve our understanding and control of

orientation of rod like particles in heavily dynamic systems with local concentration changes.

4. Statistical analysis of the conclusions from Chapters 4 and 5 would greatly enhance the contributions presented herein. To that end, representations of statistical differences in mechanical and diffusive properties that were observed as a function of CNC composition would support the analysis of this research. Further, sensitivity analysis of the parameters pertaining modeling predictions of mechanical behavior will strengthen the utility of the newly developed modeling approach.

5. The empirically determined parameters, β_{dry} and β_{wet}, implemented in the diffusion-modified percolation model are expected to have a fundamental basis. We found justification for this attribution through analysis of time-dependent ATR-FTIR spectra during D_2O absorption. Ultimately, this method was unable to fully discern hydrogen bonds associated with CNCs from those of TPU or D_2O. Therefore, a new approach, such as ^1H NMR, that quantifies the hydrogen bonding between CNCs would be expected to produce fundamental parameters that can be used with this modeling approach which could be extended to other CNC composite systems.

6. The reinforcement provided by CNCs when implemented in polymer nanocomposites is highly dependent on their orientation throughout the matrix. Extending the analysis of the diffusion-softening relationship in CNC-polymer nanocomposites to highly oriented systems would be relevant to typical processing methods for many nanocomposite materials which exploit the anisotropic properties of CNCs. CNC-TPU composites with a uniaxial orientation can be prepared through extrusion-based processing techniques. The

softening dynamics of these oriented films can then be compared to the isotropic orientation produced by solution casting in this work.

7. Similarly, the aspect ratio of CNCs is known to vary based on the cellulose source and processing conditions. High aspect ratio CNCs, such as those sourced from tunicates, may have the ability impart greater dry storage modulus enhancements than wood-based CNCs. Characterization of the diffusion-softening response as a function of CNC aspect ratio, and its influence on the percolation concentration would therefore be of interest for the community seeking to develop tailored materials for a variety of applications.
8. The solution casting method employed to fabricate CNC-TPU films is highly moisture sensitive and scales poorly for mass production. It may be possible to take advantage of this water sensitivity by using water as an anti-solvent to induce rapid precipitation of the CNC-TPU-DMF mixture. The solid phase can be easily extracted and melt pressed to generate CNC-TPU films of desired shape and thickness. Care should be taken to stay within the thermal processing window of CNCs to avoid CNC degradation. Characterization of the diffusion-softening response in rapidly processed CNC-TPU nanocomposites would validate the new processing methods ability to maintain the adequate dispersion of CNCs to attain percolation.
9. The diffusion softening mechanism of CNC-TPU nanocomposites was studied for a single TPU structure. Varying the ratio of TPU hard and soft segments may directly impact the ability of CNCs to incorporate within the matrix. Thus, a study to connect the morphology of these materials to their mechanical adaptivity would be beneficial to the development of versatile CNC-TPU nanocomposites for various applications.

10. Maintaining adequate dispersion during processing of CNCs is an ongoing pursuit within the field. Further, characterization of the dispersion of CNCs in polymer nanocomposites remains highly challenging. Many optical techniques lack the required resolution to characterize CNCs and scanning electron microscopy also lacks the contrast required to distinguish between CNCs and matrix. Atomic force microscopy (AFM) may provide some identification of the dispersion of CNCs through phase analysis comparing the stiffness difference between CNCs and the matrix, however, as the surface analysis technique falls short of fully characterizing the material dispersion. It may be possible to combine AFM with thermogravimetric analysis (TGA) of CNCs within an appropriately chosen polymer with a low degradation temperature. TGA could thus be used to verify the 2D surface dispersion of AFM and approximate a 3D dispersion index.
11. The combined CNC and TOCNF system has yet to be characterized as a nanocomposite filler. Incorporating these materials into well characterized systems of individual nanomaterials such as polyvinyl acetate and polyurethanes would validate the cooperation between CNCs and TOCNFs to provide better filler materials.

Chapter 7 - Publications

7.1 Peer Reviewed Articles

1. **Cailean Q. Pritchard**, Fernando Navaro, Maren Roman, Michael J. Bortner. Multi-axis alignment of Rod-like cellulose nanocrystals in drying droplets. J. Colloid Interf. Sci. 2021, 603, 450-458. https://doi.org/10.1016/j.jcis.2021.06.069

2. **Cailean Q. Pritchard** and Cameron T. Armstrong et al. Continuous flow synthesis of a pharmaceutical intermediate: a computational fluid dynamics approach. React. Chem. Eng. 2019, 4, 634-642. https://doi.org/10.1039/C8RE00252E

7.2 Articles in Preparation for Peer Review

1. **Cailean Q. Pritchard** and Jacob J. Fallon, et al. Diffusion-softening of Cellulose Nanocrystal and Thermoplastic Polyurethane Composites. *In Preparation for submission to ACS Applied Materials and Interfaces*

2. **Cailean Q. Pritchard** et al. Multiscale-reinforcement of cellulose nanofibrils with cellulose nanocrystals. *In Preparation for Submission to Carbohydrate Polymers*

3. Andrew Nowak, Adam Gross, Kevin Drummey, Ashley Nelson, Alexis Hocken, **Cailean Q. Pritchard**, Russell Mott, Jason Graetz. Mechanically tough, visually and infrared transparent poly(oxalamide) films. *In Preparation*

7.3 Conference Proceedings

1. **Cailean Q. Pritchard**, Fernando Navarro, Maren Roman, Michael J. Bortner. Multi-axis alignment of Rod-like cellulose nanocrystals in drying droplets, Department of Chemical Engineering Seminar Series, Virginia Tech, Blacksburg, VA, May 2021

2. **Cailean Q. Pritchard**, Jacob Fallon, Michael J. Bortner. Diffusion-Softening of a Mechanically Adaptive Cellulose Nanocrystal Polyurethane Composite, 2019 AIChE Annual Meeting, Orlando, FL, October 2019

3. **Cailean Q. Pritchard**, Jacob Fallon, Michael J. Bortner. Diffusion-Softening of a Mechanically Adaptive Cellulose Nanocrystal Polyurethane Composite, 11th Annual ChEGSA Research Symposium, Blacksburg, VA, April 2019

4. **Cailean Q. Pritchard**, Fernando Navarro, Maren Roman, Michael J. Bortner. Development of nanoparticle alignment regimes in drying cellulose nanocrystal droplet suspensions for additive manufacturing, 2018 AIChE Annual Meeting, Pittsburgh, PA, October 2018

5. **Cailean Q. Pritchard**, Fernando Navarro, Maren Roman, Michael J. Bortner. Development of nanoparticle alignment regimes in drying cellulose nanocrystal droplet suspensions for additive manufacturing, 10th Annual ChEGSA Research Symposium, Blacksburg, VA, April 2018

6. **Cailean Q. Pritchard**, Fernando Navarro, Maren Roman, Michael J. Bortner. Development of nanoparticle alignment regimes in drying cellulose nanocrystal droplet suspensions for additive manufacturing, MII Technical Conference and Review, Blacksburg VA, April 2018, Poster Presentation

7. **Cailean Q. Pritchard**, Fernando Navarro, Maren Roman, Michael J. Bortner. Development of nanoparticle alignment regimes in drying cellulose nanocrystal droplet suspensions for additive manufacturing, 255th ACS National Meeting, New Orleans, LA, March 2018, Poster Presentation.

8. **Cailean Q. Pritchard**, Fernando Navarro, Maren Roman, Michael J. Bortner. Development of nanoparticle alignment regimes in drying cellulose nanocrystal droplet suspensions for additive manufacturing, 255th ACS National Meeting, New Orleans, LA, March 2018

9. **Cailean Q. Pritchard**, Fernando Navarro, Maren Roman, Michael J. Bortner. Driving forces for cellulose nanocrystal alignment in drying droplets: Center vs edge, 2017 Southeast Polymer Forum, Blacksburg, VA, June 2017, Poster Presentation.

10. **Cailean Q. Pritchard**, Fernando Navarro, Maren Roman, Michael J. Bortner. Driving forces for cellulose nanocrystal alignment in drying droplets: Center vs edge, 9th Annual ChEGSA Research Symposium, Blacksburg, VA, April 2017

11. Fernando Navarro, **Cailean Q. Pritchard**, Michael J. Bortner, Maren Roman. Driving forces for cellulose nanocrystal alignment in drying droplets: Center vs edge, American Chemical Society, San Francisco, CA, April 2017

Appendix A

This section lays the groundwork for the development of a concentration-dependent rheological model applicable to concentrated suspensions of anisotropic materials.

A1 Modeling of Liquid Crystalline materials

Liquid crystalline (LC) materials maintain complex interactions largely dependent on their structure. In dynamic systems such as an evaporating suspension of CNCs, the organization of particles will vary in time alongside fluid dynamic interactions and mass transport. Thus, developing an accurate understanding of the particle orientation state, particularly as a function of time, is required to model the phenomenon with precision. This can be established through implementation of Landau de Gennes (LdG) theory which tracks the dynamic orientation state through the order parameter tensor, $\underline{\underline{\boldsymbol{Q}}}$. Recently, Noorozi, Grecov, and Shafei-Sabet developed a technique to evaluate the necessary parameters required by LdG theory from the well-established Leslie-Ericksen theory for LCs where the time scale for flow is much less than that of orientation on the rheological properties of the system.[1] This research plan follows Noorozi's guidance to develop a concentration and shear rate-dependent constitutive relationship for CNCs in suspension to guide our analysis of EISA in sessile droplets.

A2 Landau-de Gennes Theory

The LdG theory aids in bridging the length scale gap between micro and macroscopic interactions such that macroscopic simulations can predict behavior which is innately dependent on local interactions. These microscopic effects are captured through their influence on the orientation state via the order parameter, $\underline{\underline{\boldsymbol{Q}}}$, given by Equation (A1)

$$\underline{\underline{\boldsymbol{Q}}} = S\left(\underline{\boldsymbol{nn}} - \frac{1}{3}\underline{\underline{\boldsymbol{\delta}}}\right) + \frac{1}{3}P\left(\underline{\boldsymbol{mm}} - \underline{\boldsymbol{ll}}\right) \tag{A1}$$

Where $\underline{\underline{\boldsymbol{\delta}}}$, is the identity tensor, S is the scalar order parameter given by Equation (A2), and P is given by Equation (A3)

$$S = \frac{3}{2}\mu_n \tag{A2}$$

$$P = 3\left(\mu_n + \frac{1}{2}\right) \tag{A3}$$

Where μ_n, μ_m, and μ_l are the eigenvalues of $\underline{\underline{\boldsymbol{Q}}}$ in descending order of magnitude and correspond to the eigenvectors $\boldsymbol{n}$, $\boldsymbol{m}$, and $\boldsymbol{l}$, resepectively. Additionally, the underbar represents vector quantities, the double underbar represents a tensorial quantity, and all other variables are scalars. Lastly, the accent, $\tilde{x}$, represents dimensionless quantities.

Of paramount interest to LdG theory, the evolution equation defines the time-dependent behavior of LC orientation and is given by Equation (A4).[1-3]

$$\underline{\underline{\widehat{\boldsymbol{Q}}}} = \underline{\underline{\boldsymbol{F}}}\left(\underline{\boldsymbol{\nabla v}}, \underline{\underline{\boldsymbol{Q}}}\right) + \underline{\underline{\boldsymbol{H}^{sr}}}\left(\overline{D_r}, \underline{\underline{\boldsymbol{Q}}}\right) + \underline{\underline{\boldsymbol{H}^{lr}}}\left(\overline{D_r}, \underline{\boldsymbol{\nabla}}\underline{\underline{\boldsymbol{Q}}}\right) + \underline{\underline{\boldsymbol{\mathcal{P}}}}\left(\underline{\boldsymbol{\nabla}}\underline{\underline{\boldsymbol{Q}}}\right) \tag{A4}$$

The four components to the evolution equations describe, in order, the contribution of flow, $\underline{\underline{\boldsymbol{F}}}$, short-range elasticity, $\underline{\underline{\boldsymbol{H}^{sr}}}$, long-range elasticity, $\underline{\underline{\boldsymbol{H}^{lr}}}$, and chiral interaction, $\underline{\underline{\boldsymbol{\mathcal{P}}}}$. These contributions are expressed in Equations (A5)-(A9) and a table of parameters, Table A-1, is provided to provide clarification.[1, 3, 4]

$$\underline{\underline{\widehat{\boldsymbol{Q}}}} = \frac{\partial \underline{\underline{\boldsymbol{Q}}}}{\partial t} + \left(\underline{\tilde{\boldsymbol{v}}} \cdot \underline{\boldsymbol{\nabla}}\right)\underline{\underline{\mathbf{Q}}} - \underline{\underline{\widetilde{\boldsymbol{W}}}} \cdot \underline{\underline{\boldsymbol{Q}}} + \underline{\underline{\boldsymbol{Q}}} \cdot \underline{\underline{\widetilde{\boldsymbol{W}}}} \tag{A5}$$

$$\underline{\underline{\boldsymbol{F}}} = \frac{2}{3}\beta\underline{\underline{\widetilde{\boldsymbol{A}}}} + \beta\left[\underline{\underline{\widetilde{\boldsymbol{A}}}}\cdot\underline{\underline{\boldsymbol{Q}}} + \underline{\underline{\boldsymbol{Q}}}\cdot\underline{\underline{\widetilde{\boldsymbol{A}}}} - \frac{2}{3}\left(\underline{\underline{\widetilde{\boldsymbol{A}}}}:\underline{\underline{\boldsymbol{Q}}}\right)\underline{\underline{\boldsymbol{\delta}}}\right]$$
$$-\frac{1}{2}\beta\left\{\left(\underline{\underline{\widetilde{\boldsymbol{A}}}}:\underline{\underline{\boldsymbol{Q}}}\right)\underline{\underline{\boldsymbol{Q}}} + \underline{\underline{\widetilde{\boldsymbol{A}}}}\cdot\underline{\underline{\boldsymbol{Q}}}\cdot\underline{\underline{\boldsymbol{Q}}} + \underline{\underline{\boldsymbol{Q}}}\cdot\underline{\underline{\widetilde{\boldsymbol{A}}}}\cdot\underline{\underline{\boldsymbol{Q}}} + \underline{\underline{\boldsymbol{Q}}}\cdot\underline{\underline{\boldsymbol{Q}}}\cdot\underline{\underline{\widetilde{\boldsymbol{A}}}}\right. \quad \text{(A6)}$$
$$\left.-\left[\left(\underline{\underline{\boldsymbol{Q}}}\cdot\underline{\underline{\boldsymbol{Q}}}\right):\underline{\underline{\widetilde{\boldsymbol{A}}}}\right]\underline{\underline{\boldsymbol{\delta}}}\right\}$$

$$\underline{\underline{\boldsymbol{H}}}^{sr} = \frac{1}{De}\left[\left(\frac{U}{3}-1\right)\underline{\underline{\boldsymbol{Q}}} + U\underline{\underline{\boldsymbol{Q}}}\cdot\underline{\underline{\boldsymbol{Q}}} - U\left(\underline{\underline{\boldsymbol{Q}}}:\underline{\underline{\boldsymbol{Q}}}\right)\cdot\left(\underline{\underline{\boldsymbol{Q}}} + \frac{1}{3}\underline{\underline{\boldsymbol{\delta}}}\right)\right] \quad \text{(A7)}$$

$$\underline{\underline{\boldsymbol{H}}}^{lr} = \frac{1}{Er}\left\{\underline{\underline{\boldsymbol{\nabla^2 Q}}} + \frac{L^*}{2}\left[\underline{\underline{\boldsymbol{\nabla}}}\left(\underline{\underline{\boldsymbol{\nabla}}}\cdot\underline{\underline{\boldsymbol{Q}}}\right) + \left[\underline{\underline{\boldsymbol{\nabla}}}\left(\underline{\underline{\boldsymbol{\nabla}}}\cdot\underline{\underline{\boldsymbol{Q}}}\right)\right]^T - \frac{2}{3}tr\left(\underline{\underline{\boldsymbol{\nabla}}}\left(\underline{\underline{\boldsymbol{\nabla}}}\cdot\underline{\underline{\boldsymbol{Q}}}\right)\right)\right]\right\} \quad \text{(A8)}$$

$$\underline{\underline{\boldsymbol{\mathcal{P}}}} = \frac{\Theta}{Er}\left(\epsilon_{mik}\underline{\underline{\boldsymbol{Q}}}_{mj,k} + \epsilon_{mjk}\underline{\underline{\boldsymbol{Q}}}_{mi,k}\right) \quad \text{(A9)}$$

Table A-1. Parameters required for Landau-de Gennes orientation evolution equation.

Parameter	Expression/Quantity	Unit	Description
$\underline{\underline{\widetilde{\boldsymbol{W}}}}$	$\frac{1}{2\gamma}\left(\left(\underline{\underline{\boldsymbol{\nabla}\widetilde{\boldsymbol{v}}}}\right)^T - \underline{\underline{\boldsymbol{\nabla}\widetilde{\boldsymbol{v}}}}\right)$	1	Dimensionless vorticity tensor
$\underline{\underline{\widetilde{\boldsymbol{A}}}}$	$\frac{1}{2\gamma}\left(\underline{\underline{\boldsymbol{\nabla}\widetilde{\boldsymbol{v}}}} + \left(\underline{\underline{\boldsymbol{\nabla}\widetilde{\boldsymbol{v}}}}\right)^T\right)$	1	Dimensionless rate of deformation tensor
$\boldsymbol{\beta}$	$\frac{p^2-1}{p^2+1}$	1	Shape Factor
$\boldsymbol{p}$	$\frac{l}{d}$	1	Aspect ratio

$\boldsymbol{De}$	$\frac{\gamma}{6D_r}$	1	Deborah number
$\boldsymbol{D_r}$	$\frac{\beta D_{r0}}{c^2 L^6 R^2}$	$\frac{1}{s}$	Pre-averaged rotational diffusivity
$\boldsymbol{D_{r0}}$	$\frac{3k_B T[\ln(p) - .8]}{\pi \eta_s L^3}$	$\frac{1}{s}$	Rotational diffusivity in dilute solution
$\boldsymbol{R}$	$\frac{ck_B T H^2}{L_1}$	1	Ratio of short to long-range order elasticity
$\boldsymbol{U}$	$3.5 - 4$	1	Dimensionless nematic potential
$\boldsymbol{Er}$	$\frac{ck_B T \gamma H^2}{6L_1 D_r}$	1	Ericksen number
$\boldsymbol{L_1}$	$\frac{K_{22}}{2S^2}$	N	Landau elastic coefficient
$\boldsymbol{L_2}$	$\frac{K_{11} - K_{22}}{S^2}$	N	Landau elastic coefficient
$\boldsymbol{L^*}$	$\frac{L_2}{L_1}$	1	Ratio of landau elastic coefficients
$\boldsymbol{K_{ii}}$		N	Frank elasticity constant
$\boldsymbol{\Theta}$	$\frac{L^2}{\mathcal{L}^2}$	1	Ratio of anisotropic to isotropic distortional energy
$\boldsymbol{L}$		m	Long-range isotropic length scale
$\boldsymbol{\mathcal{L}}$		m	Long-range anisotropic length scale

Additional parameters are expressed where c is the number of molecules per unit volume, k_B is the Boltzmann constant, T is the temperature, γ is the characteristic shear rate, H is the characteristic length scale for flow, and η_s is the solvent viscosity.

Finally, the total stress tensor can be written as Equation (A10) where ν_i are the dimensionless Landau viscosity coefficients.

$$\begin{aligned}\underline{\underline{\tilde{\tau}}}_{\nu} = \nu_1 \underline{\underline{\tilde{A}}} + \nu_2 \left[\underline{\underline{Q}} \cdot \underline{\underline{\tilde{A}}} + \underline{\underline{\tilde{A}}} \cdot \underline{\underline{Q}} - \frac{2}{3}\left(\underline{\underline{Q}} : \underline{\underline{\tilde{A}}}\right)\underline{\underline{\delta}}\right] \\ + \nu_4 \left\{\left(\underline{\underline{\tilde{A}}} : \underline{\underline{Q}}\right)\underline{\underline{Q}} + \underline{\underline{\tilde{A}}} \cdot \underline{\underline{Q}} \cdot \underline{\underline{Q}} + \underline{\underline{Q}} \cdot \underline{\underline{\tilde{A}}} \cdot \underline{\underline{Q}} + \underline{\underline{Q}} \cdot \underline{\underline{Q}} \cdot \underline{\underline{\tilde{A}}}\right. \\ \left. + \left[\left(\underline{\underline{Q}} : \underline{\underline{Q}}\right)\underline{\underline{\tilde{A}}}\right]\underline{\underline{\delta}}\right\}\end{aligned} \tag{A10}$$

Following Noorozi's approach to evaluate ν_i, we will extend their model to predict viscosity for CNC suspensions as a function of both concentration and shear rate.[1]

A3 Tensor Operations Required for Computational Analysis of Landau-de Gennes Theory

A3.1 Motivation

The following expressions are provided to facilitate the translation of Equations (A4) and (A10) to finite element analysis software. As computational analysis software requires explicit expressions for each corresponding stress tensor component, simplified expressions for each mathematical operation required to solve the equations in Appendix A are provided in detail. Specifically, the translation between tensor notation and summation notation are provided and are followed by an equivalent graphical representation for each component.

A3.2 Tensor Operations

A3.2.1 Tensor Dot Product $(A_{ij} \cdot B_{kl})$

$$A_{ij} \bullet B_{kl} = \sum_i \sum_j A_{ij}\delta_i\delta_j \bullet \sum_k \sum_l B_{kl}\delta_k\delta_l$$

$$= \sum_i \sum_j \sum_k \sum_l A_{ij}B_{kl}\delta_i(\delta_j \bullet \delta_k)\delta_l$$

$$= \sum_i \sum_j \sum_l A_{ij}B_{jl}\delta_i\delta_l$$

$$\begin{bmatrix} A_{11}B_{11} + A_{12}B_{21} + A_{13}B_{31} & A_{11}B_{12} + A_{12}B_{22} + A_{13}B_{32} & A_{11}B_{13} + A_{12}B_{23} + A_{13}B_{33} \\ A_{21}B_{11} + A_{22}B_{21} + A_{23}B_{31} & A_{21}B_{12} + A_{22}B_{22} + A_{23}B_{32} & A_{21}B_{13} + A_{22}B_{23} + A_{23}B_{33} \\ A_{31}B_{11} + A_{32}B_{21} + A_{33}B_{31} & A_{31}B_{12} + A_{32}B_{22} + A_{33}B_{32} & A_{31}B_{13} + A_{32}B_{23} + A_{33}B_{33} \end{bmatrix}$$

A3.2.2 Tensor Dot Product $(A_{ij} \cdot B_{kl} \cdot C_{mn})$

$$A_{ij} \bullet B_{kl} \bullet C_{mn} = \sum_i \sum_j A_{ij}\delta_i\delta_j \bullet \sum_k \sum_l B_{kl}\delta_k\delta_l \bullet \sum_m \sum_n C_{mn}\delta_m\delta_n$$

$$= \sum_i \sum_j \sum_k \sum_l \sum_m \sum_n A_{ij}B_{kl}C_{mn}(\delta_i\delta_j \bullet \delta_k\delta_l \bullet \delta_m\delta_n)$$

$$= \sum_i \sum_j \sum_l \sum_n A_{ij}B_{jl}C_{ln}\delta_i\delta_n$$

$$\begin{bmatrix} \begin{pmatrix}(A_{11}B_{11}+A_{12}B_{21}+A_{13}B_{31})C_{11}+\\(A_{11}B_{12}+A_{12}B_{22}+A_{13}B_{32})C_{21}+\\(A_{11}B_{13}+A_{12}B_{23}+A_{13}B_{33})C_{31}\end{pmatrix} & \begin{pmatrix}(A_{11}B_{11}+A_{12}B_{21}+A_{13}B_{31})C_{12}+\\(A_{11}B_{12}+A_{12}B_{22}+A_{13}B_{32})C_{22}+\\(A_{11}B_{13}+A_{12}B_{23}+A_{13}B_{33})C_{32}\end{pmatrix} & \begin{pmatrix}(A_{11}B_{11}+A_{12}B_{21}+A_{13}B_{31})C_{13}+\\(A_{11}B_{12}+A_{12}B_{22}+A_{13}B_{32})C_{23}+\\(A_{11}B_{13}+A_{12}B_{23}+A_{13}B_{33})C_{33}\end{pmatrix} \\ \begin{pmatrix}(A_{21}B_{11}+A_{22}B_{21}+A_{23}B_{31})C_{11}+\\(A_{21}B_{12}+A_{22}B_{22}+A_{23}B_{32})C_{21}+\\(A_{21}B_{13}+A_{22}B_{23}+A_{23}B_{33})C_{31}\end{pmatrix} & \begin{pmatrix}(A_{21}B_{11}+A_{22}B_{21}+A_{23}B_{31})C_{12}+\\(A_{21}B_{12}+A_{22}B_{22}+A_{23}B_{32})C_{22}+\\(A_{21}B_{13}+A_{22}B_{23}+A_{23}B_{33})C_{32}\end{pmatrix} & \begin{pmatrix}(A_{21}B_{11}+A_{22}B_{21}+A_{23}B_{31})C_{13}+\\(A_{21}B_{12}+A_{22}B_{22}+A_{23}B_{32})C_{23}+\\(A_{21}B_{13}+A_{22}B_{23}+A_{23}B_{33})C_{33}\end{pmatrix} \\ \begin{pmatrix}(A_{31}B_{11}+A_{32}B_{21}+A_{33}B_{31})C_{11}+\\(A_{31}B_{12}+A_{32}B_{32}+A_{33}B_{32})C_{21}+\\(A_{31}B_{13}+A_{32}B_{23}+A_{33}B_{33})C_{31}\end{pmatrix} & \begin{pmatrix}(A_{31}B_{11}+A_{32}B_{21}+A_{33}B_{31})C_{12}+\\(A_{31}B_{12}+A_{32}B_{32}+A_{33}B_{32})C_{22}+\\(A_{31}B_{13}+A_{32}B_{23}+A_{33}B_{33})C_{32}\end{pmatrix} & \begin{pmatrix}(A_{31}B_{11}+A_{32}B_{21}+A_{33}B_{31})C_{13}+\\(A_{31}B_{12}+A_{32}B_{32}+A_{33}B_{32})C_{23}+\\(A_{31}B_{13}+A_{32}B_{23}+A_{33}B_{33})C_{33}\end{pmatrix} \end{bmatrix}$$

A3.2.3 Tensor Double Dot Product $(A_{ij} : B_{kl})$

$$A_{ij} : B_{kl} = \sum_i \sum_j A_{ij}\delta_i\delta_j : \sum_k \sum_l B_{kl}\delta_k\delta_l$$

$$= \sum_i \sum_j \sum_k \sum_l A_{ij}B_{kl}(\delta_i\delta_j : \delta_k\delta_l)$$

$$= \sum_i \sum_j A_{ij}B_{ji}$$

$$\underline{\underline{A}} : \underline{\underline{B}} = A_{11}B_{11} + A_{12}B_{21} + A_{13}B_{31} + A_{21}B_{12} + A_{22}B_{22} + A_{23}B_{32} + A_{31}B_{13} + A_{32}B_{23} + A_{33}B_{33}$$

A3.2.4 Tensor Double Dot Product $\left((A_{ij} : B_{kl})C_{mn}\right)$

$$(A_{ij} : B_{kl})C_{mn} = (\sum_i \sum_j A_{ij}\delta_i\delta_j : \sum_k \sum_l B_{kl}\delta_k\delta_l) \sum_m \sum_n C_{mn}\delta_m\delta_n$$

$$= \sum_i \sum_j \sum_k \sum_l \sum_m \sum_n A_{ij}B_{kl}C_{mn}(\delta_i\delta_j : \delta_k\delta_l)\delta_m\delta_n$$

$$= \sum_i \sum_j \sum_m \sum_n A_{ij}B_{ji}C_{mn}\delta_m\delta_n$$

$$(A_{11}B_{11} + A_{12}B_{21} + A_{13}B_{31} + A_{21}B_{12} + A_{22}B_{22} + A_{23}B_{32} + A_{31}B_{13} + A_{32}B_{23} + A_{33}B_{33}) \begin{bmatrix} C_{11} & C_{12} & C_{13} \\ C_{21} & C_{22} & C_{23} \\ C_{31} & C_{32} & C_{33} \end{bmatrix}$$

A3.2.5 Tensor Double Dot Product $\left((A_{ij} \cdot B_{kl}) : C_{mn}\right)$

$$(A_{ij} \bullet B_{kl}) : C_{mn} = (\sum_i \sum_j A_{ij}\delta_i\delta_j \bullet \sum_k \sum_l B_{kl}\delta_k\delta_l) : \sum_m \sum_n C_{mn}\delta_m\delta_n$$

$$= \sum_i \sum_j \sum_k \sum_l \sum_m \sum_n A_{ij}B_{kl}C_{mn}(\delta_i\delta_j \bullet \delta_k\delta_l) : \delta_m\delta_n$$

$$= \sum_i \sum_j \sum_l \sum_m \sum_n A_{ij}B_{jl}C_{mn}(\delta_i\delta_l : \delta_m\delta_n)$$

$$= \sum_i \sum_j \sum_l A_{ij}B_{jl}C_{li}$$

$$C_{11}(A_{11}B_{11} + A_{12}B_{21} + A_{13}B_{31}) +$$
$$C_{21}(A_{11}B_{12} + A_{12}B_{22} + A_{13}B_{32}) +$$
$$C_{31}(A_{11}B_{13} + A_{12}B_{23} + A_{13}B_{33}) +$$

$$C_{12}(A_{21}B_{11} + A_{22}B_{21} + A_{23}B_{31}) +$$
$$C_{22}(A_{21}B_{12} + A_{22}B_{22} + A_{23}B_{32}) +$$
$$C_{32}(A_{21}B_{13} + A_{22}B_{23} + A_{23}B_{33}) +$$

$$C_{13}(A_{31}B_{11} + A_{32}B_{21} + A_{33}B_{31}) +$$
$$C_{23}(A_{31}B_{12} + A_{32}B_{22} + A_{33}B_{32}) +$$
$$C_{33}(A_{31}B_{13} + A_{32}B_{23} + A_{33}B_{33})$$

A3.3 Tensor Differential Operations

A3.3.1 Tensor Gradient (∇A_{ij})

$$\nabla A_{ij} = \sum_i \frac{\partial}{\partial x_i} \delta_i \left(\sum_j \sum_k A_{ij} \delta_j \delta_k \right)$$

$$= \sum_i \sum_j \sum_k \frac{\partial}{\partial x_i} A_{jk} \delta_i \delta_j \delta_k$$

$$\left[\frac{\partial}{\partial x_1} \begin{pmatrix} A_{11} & A_{12} & A_{13} \\ A_{21} & A_{22} & A_{23} \\ A_{31} & A_{32} & A_{33} \end{pmatrix} \quad \frac{\partial}{\partial x_2} \begin{pmatrix} A_{11} & A_{12} & A_{13} \\ A_{21} & A_{22} & A_{23} \\ A_{31} & A_{32} & A_{33} \end{pmatrix} \quad \frac{\partial}{\partial x_3} \begin{pmatrix} A_{11} & A_{12} & A_{13} \\ A_{21} & A_{22} & A_{23} \\ A_{31} & A_{32} & A_{33} \end{pmatrix} \right]$$

A3.3.2 Tensor Laplacian $(\nabla^2 A_{ij})$

$$\begin{aligned}
\nabla^2 A_{ij} &= \nabla \bullet \nabla A_{ij} \\
&= \sum_i \frac{\partial}{\partial x_i}\delta_i \bullet \sum_j \frac{\partial}{\partial x_j}\delta_j \left(\sum_k \sum_l A_{kl}\delta_k\delta_l\right) \\
&= \sum_i \sum_j \sum_k \sum_l \frac{\partial}{\partial x_i}\frac{\partial}{\partial x_j} A_{kl}(\delta_i \bullet \delta_j)\delta_k\delta_l \\
&= \sum_i \sum_j \sum_l \frac{\partial}{\partial x_i}\frac{\partial}{\partial x_i} A_{kl}\delta_k\delta_l \\
&= \sum_i \sum_j \sum_l \frac{\partial^2}{\partial x_i^2} A_{kl}\delta_k\delta_l
\end{aligned}$$

$$\left(\frac{\partial^2}{\partial x_1^2} + \frac{\partial^2}{\partial x_2^2} + \frac{\partial^2}{\partial x_3^2}\right)\begin{bmatrix} A_{11} & A_{12} & A_{13} \\ A_{21} & A_{22} & A_{23} \\ A_{31} & A_{32} & A_{33} \end{bmatrix} = \begin{bmatrix} \nabla^2 A_{11} & \nabla^2 A_{12} & \nabla^2 A_{13} \\ \nabla^2 A_{21} & \nabla^2 A_{22} & \nabla^2 A_{23} \\ \nabla^2 A_{31} & \nabla^2 A_{32} & \nabla^2 A_{33} \end{bmatrix}$$

$$\nabla^2 = \frac{\partial^2}{\partial x_1^2} + \frac{\partial^2}{\partial x_2^2} + \frac{\partial^2}{\partial x_3^2}$$

A3.3.3 Tensor Divergence $(\nabla \cdot A_{ij})$

$$\nabla \bullet A_{ij} = \sum_i \frac{\partial}{\partial x_i} \delta_i \bullet \sum_j \sum_k A_{jk} \delta_j \delta_k)$$

$$= \sum_i \sum_j \sum_k \frac{\partial}{\partial x_i} A_{jk} (\delta_i \bullet \delta_j \delta_k)$$

$$= \sum_i \sum_k \frac{\partial}{\partial x_i} A_{ik} \delta_i \delta_k$$

$$\begin{bmatrix} \frac{\partial}{\partial x_1} A_{11} + \frac{\partial}{\partial x_2} A_{21} + \frac{\partial}{\partial x_3} A_{31} \\ \frac{\partial}{\partial x_1} A_{12} + \frac{\partial}{\partial x_2} A_{22} + \frac{\partial}{\partial x_3} A_{32} \\ \frac{\partial}{\partial x_1} A_{13} + \frac{\partial}{\partial x_2} A_{23} + \frac{\partial}{\partial x_3} A_{33} \end{bmatrix}$$

A3.3.4 Tensor Gradient of Divergence $\left(\nabla(\nabla \cdot A_{ij})\right)$

$$\nabla(\nabla \bullet A_{ij}) = \sum_i \frac{\partial}{\partial x_i}\delta_i\left(\sum_j \frac{\partial}{\partial x_j}\delta_j \bullet \sum_k \sum_l A_{kl}\delta_k\delta_l\right)$$

$$= \sum_i \sum_j \sum_k \sum_l \frac{\partial}{\partial x_i}\frac{\partial}{\partial x_j} A_{kl}\delta_i(\delta_j \bullet \delta_k\delta_l)$$

$$= \sum_i \sum_j \sum_l \frac{\partial}{\partial x_i}\frac{\partial}{\partial x_j} A_{jl}\delta_i\delta_l$$

$$\begin{bmatrix} \frac{\partial}{\partial x_1}\frac{\partial}{\partial x_1}A_{11} + \frac{\partial}{\partial x_1}\frac{\partial}{\partial x_2}A_{21} + \frac{\partial}{\partial x_1}\frac{\partial}{\partial x_3}A_{31} & \frac{\partial}{\partial x_1}\frac{\partial}{\partial x_1}A_{12} + \frac{\partial}{\partial x_1}\frac{\partial}{\partial x_2}A_{22} + \frac{\partial}{\partial x_1}\frac{\partial}{\partial x_3}A_{32} & \frac{\partial}{\partial x_1}\frac{\partial}{\partial x_1}A_{13} + \frac{\partial}{\partial x_1}\frac{\partial}{\partial x_2}A_{23} + \frac{\partial}{\partial x_1}\frac{\partial}{\partial x_3}A_{33} \\ \frac{\partial}{\partial x_2}\frac{\partial}{\partial x_1}A_{11} + \frac{\partial}{\partial x_2}\frac{\partial}{\partial x_2}A_{21} + \frac{\partial}{\partial x_2}\frac{\partial}{\partial x_3}A_{31} & \frac{\partial}{\partial x_2}\frac{\partial}{\partial x_1}A_{12} + \frac{\partial}{\partial x_2}\frac{\partial}{\partial x_2}A_{22} + \frac{\partial}{\partial x_2}\frac{\partial}{\partial x_3}A_{32} & \frac{\partial}{\partial x_2}\frac{\partial}{\partial x_1}A_{13} + \frac{\partial}{\partial x_2}\frac{\partial}{\partial x_2}A_{23} + \frac{\partial}{\partial x_2}\frac{\partial}{\partial x_3}A_{33} \\ \frac{\partial}{\partial x_3}\frac{\partial}{\partial x_1}A_{11} + \frac{\partial}{\partial x_3}\frac{\partial}{\partial x_2}A_{21} + \frac{\partial}{\partial x_3}\frac{\partial}{\partial x_3}A_{31} & \frac{\partial}{\partial x_3}\frac{\partial}{\partial x_1}A_{12} + \frac{\partial}{\partial x_3}\frac{\partial}{\partial x_2}A_{22} + \frac{\partial}{\partial x_3}\frac{\partial}{\partial x_3}A_{32} & \frac{\partial}{\partial x_3}\frac{\partial}{\partial x_1}A_{13} + \frac{\partial}{\partial x_3}\frac{\partial}{\partial x_2}A_{23} + \frac{\partial}{\partial x_3}\frac{\partial}{\partial x_3}A_{33} \end{bmatrix}$$

References

1. Noroozi, N.; Grecov, D.; Shafiei-Sabet, S., Estimation of viscosity coefficients and rheological functions of nanocrystalline cellulose aqueous suspensions. *Liquid Crystals* **2013,** *41* (1), 56-66.
2. Dana Grecov, A. D. R., Theoretical And Computational Rheology for discotic nematic liquid crystals. *Mol. Cryst. Liq. Cryst.* **2003,** *391*, 57-94.
3. Dustin G. Venhaus, K. S. C. M. J. G., Dynamics of Liquid Crystals Under Applied Shear. *Liquid Crystals* **2013,** *40* (6), 846-853.
4. Acevedo, A.; Cotts, P. M.; Shine, A. D., Molecular Weight Dependence of the Rotational Diffusivity of Rodlike Polymers in Concentrated Nematic Solutions. *Macromolecules* **2005,** *38* (15), 6648-6655.